Daniele Esposito

UNIVERSITÀ DEGLI STUDI DI NAPOLI
FEDERICO II

itee Ph.D
INFORMATION TECHNOLOGY
ELECTRICAL ENGINEERING

THE "FEDERICA" HAND:
A SIMPLE, VERY EFFICIENT PROSTHESIS

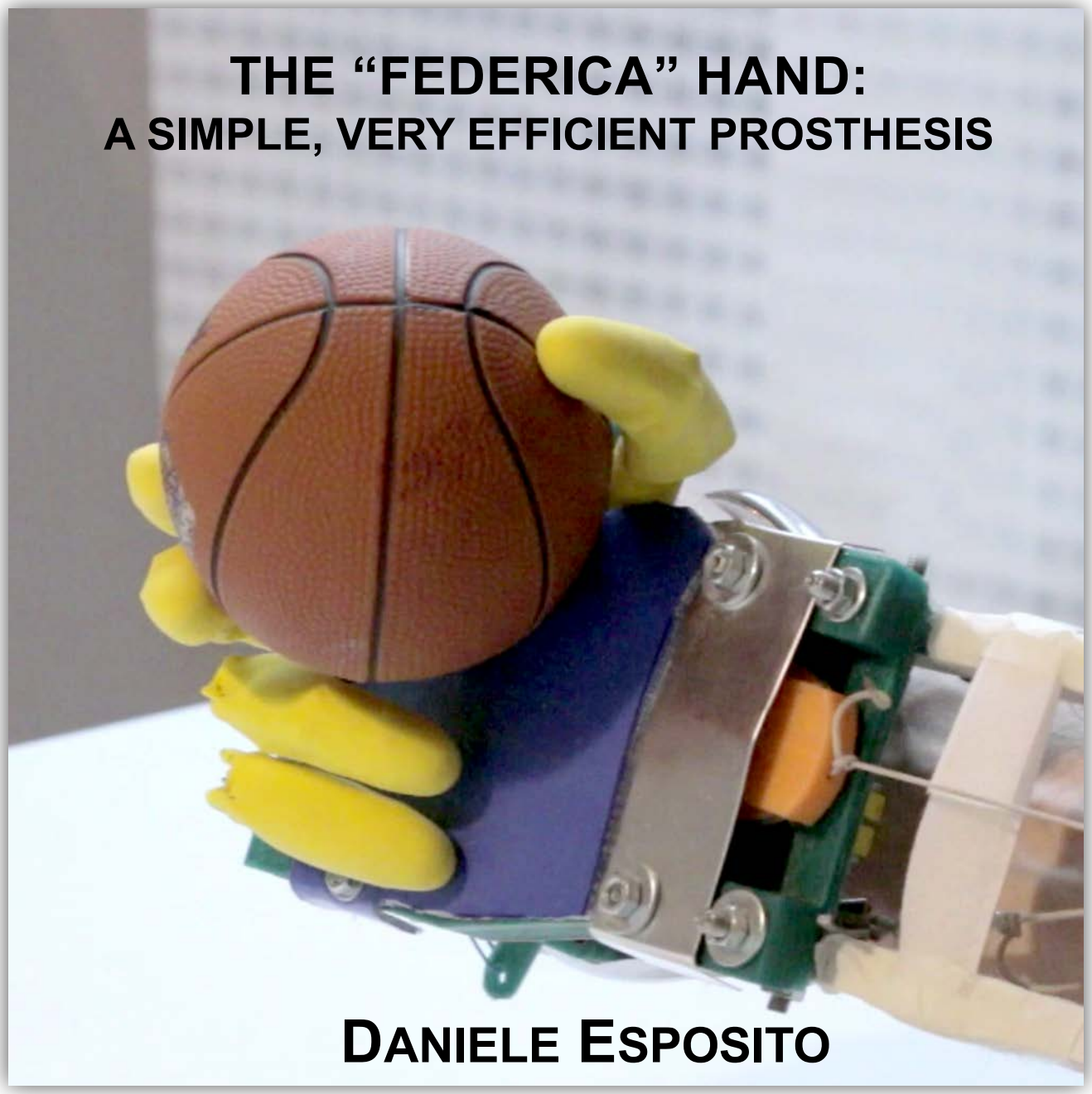

DANIELE ESPOSITO

PH.D. IN INFORMATION TECHNOLOGY AND ELECTRICAL ENGINEERING

THE "FEDERICA" HAND: A SIMPLE, VERY EFFICIENT PROSTHESIS

2020 - XXXIII

UNIVERSITÀ DEGLI STUDI DI NAPOLI FEDERICO II

UNIVERSITÀ DEGLI STUDI DI NAPOLI FEDERICO II

PH.D. THESIS

IN

THE "FEDERICA" HAND:

A SIMPLE, VERY EFFICIENT PROSTHESIS

DANIELE ESPOSITO

TUTOR: **PROF. PAOLO BIFULCO**
CO-TUTOR: **PROF. MARIO CESARELLI**
CO-TUTOR: **PROF. VINCENZO NIOLA**
ABROAD CO-TUTOR: **PROF. GAETANO GARGIULO**
COORDINATOR: **PROF. DANIELE RICCIO**

XXXIII CICLO

SCUOLA POLITECNICA E DELLE SCIENZE DI BASE
DIPARTIMENTO DI INGEGNERIA ELETTRICA E TECNOLOGIE DELL'INFORMAZIONE

I hereby declare that, the contents and organisation of this dissertation constitute my own original work and does not compromise in any way the rights of third parties, including those relating to the security of personal data.

…….....

Daniele Esposito

Naples, 5th February, 2021

Summary

Hand prostheses partially restore hand appearance and functionalities. Not everyone can afford expensive prostheses and many low-cost prostheses have been proposed. In particular, 3D printers have provided great opportunities by simplifying the manufacturing process and reducing costs. Generally, active prostheses use multiple motors for fingers movement and are controlled by electromyographic (EMG) signals. The “Federica” hand is a single motor prosthesis, equipped with an adaptive grasp and controlled by a force-myographic signal.

The “Federica” hand is 3D printed and has an anthropomorphic morphology with five fingers, each consisting of three phalanges. The movement generated by a single servomotor is transmitted to the fingers by inextensible tendons that form a closed chain; practically, no springs are used for passive hand opening. A differential mechanical system simultaneously distributes the motor force in predefined portions on each finger, regardless of their actual positions. Proportional control of hand closure is achieved by measuring the contraction of residual limb muscles by means of a force sensor, replacing the EMG. The electrical current of the servomotor is monitored to provide the user with a sensory feedback of the grip force, through a small vibration motor. A simple Arduino board was adopted as processing unit.

The differential mechanism guarantees an efficient transfer of mechanical energy from the motor to the fingers and a secure grasp of any object, regardless of its shape and deformability. The force sensor, being extremely thin, can be easily embedded into the prosthesis socket and positioned on both muscles and tendons; it offers some advantages over the EMG as it does not require any electrical contact or signal processing to extract information about the muscle contraction intensity. The grip speed is high enough to allow the user to grab objects on the fly: from the muscle trigger until to the complete hand closure, “Federica” takes about half a second. The cost of the device is about 100 US$. Preliminary tests carried out on a patient with transcarpal amputation, showed high performances in controlling the prosthesis, after a very rapid training session.

The "Federica" hand turned out to be a lightweight, low-cost and extremely efficient prosthesis. The project is intended to be open-source: all the information needed to produce the prosthesis (e.g. CAD files, circuit schematics, software) can be downloaded from a public repository. Thus, allowing everyone to use the “Federica” hand and customize or improve it.

To my beloved family...

PUBLICATIONS

I. Bifulco, P.; **Esposito, D.;** Gargiulo, G.D.; Savino, S.; Niola, V.; Iuppariello, L.; Cesarelli, M. A stretchable, conductive rubber sensor to detect muscle contraction for prosthetic hand control. In Proceedings of the 2017 E-Health and Bioengineering Conference (EHB); 2017; pp. 173–176.

II. Bifulco, P.; Iuppariello, L.; Romano, M.; Fratini, A.; **Esposito, D.;** Clemente, F.; Cesarelli, M. Assessment of cervical disk prosthesis by means of video-fluoroscopy image processing. In Proceedings of the 2017 E-Health and Bioengineering Conference (EHB); 2017; pp. 169–172.

III. **Esposito, D.**; Andreozzi, E.; Fratini, A.; Gargiulo, G.D.; Savino, S.; Niola, V.; Bifulco, P. A Piezoresistive Sensor to Measure Muscle Contraction and Mechanomyography. *Sensors* **2018**, *18*, doi:10.3390/s18082553.

IV. Andreozzi, E.; Gargiulo, G.D.; Fratini, A.; **Esposito, D.;** Bifulco, P. A Contactless Sensor for Pacemaker Pulse Detection: Design Hints and Performance Assessment. *Sensors* **2018**, *18*, 2715, doi:10.3390/s18082715.

V. Parajuli, N.; Sreenivasan, N.; Bifulco, P.; Cesarelli, M.; Savino, S.; Niola, V.; **Esposito, D.**; Hamilton, T.J.; Naik, G.R.; Gunawardana, U.; et al. Real-Time EMG Based Pattern Recognition Control for Hand Prostheses: A Review on Existing Methods, Challenges and Future Implementation. *Sensors* **2019**, *19*, 4596, doi:10.3390/s19204596.

VI. Parajuli, N.; Ulloa, D.F.; Sreenivasan, N.; Naik, G.; Bifulco, P.; **Esposito, D.**; Savino, S.; Cesarelli, M.; Hamilton, T.; Gunawardana, U.; et al. Electrodeless FSR Linear Envelope Signal for Muscle Contraction Measurement. In Proceedings of the 2019 International Conference on Electrical Engineering Research Practice (ICEERP); 2019; pp. 1–5.

VII. Polley, C.; Andreozzi, E.; Bifulco, P.; **Esposito, D.**; Naik, G.; Gunawardana, U.; Gargiulo, G. Low Cost Analogue Front End for Electronic Stethoscopes Application with Silicone Enclosure. In Proceedings of the 2019 International Conference on Electrical Engineering Research Practice (ICEERP); 2019; pp. 1–6.

VIII. **Esposito, D**.; Cosenza, C.; Gargiulo, G.D.; Andreozzi, E.; Niola, V.; Fratini, A.; D'Addio, G.; Bifulco, P. Experimental Study to Improve "Federica" Prosthetic Hand and Its Control System. In Proceedings of the XV Mediterranean Conference on Medical and Biological Engineering and Computing – MEDICON 2019; Henriques, J., Neves, N., de Carvalho, P., Eds.; Springer International Publishing: Cham, 2020; pp. 586–593.

IX. **Esposito, D.**; Savino, S.; Cosenza, C.; Gargiulo, G.D.; Fratini, A.; Cesarelli, G.; Bifulco, P. Study on the Activation Speed and the Energy Consumption of "Federica" Prosthetic Hand. In Proceedings of the XV Mediterranean Conference on Medical and Biological Engineering and Computing – MEDICON 2019; Henriques, J., Neves, N., de Carvalho, P., Eds.; Springer International Publishing: Cham, 2020; pp. 594–603.

X. Andreozzi, E.; Pirozzi, M.A.; Sarno, A.; **Esposito, D.**; Cesarelli, M.; Bifulco, P. A Comparison of Denoising Algorithms for Effective Edge Detection in X-Ray Fluoroscopy. In Proceedings of the XV Mediterranean Conference on Medical and Biological Engineering and Computing – MEDICON 2019; Henriques, J., Neves, N., de Carvalho, P., Eds.; Springer International Publishing: Cham, 2020; pp. 405–413.

XI. **Esposito, D.**; Andreozzi, E.; Gargiulo, G.D.; Fratini, A.; D'Addio, G.; Naik, G.R.; Bifulco, P. A Piezoresistive Array Armband With Reduced Number of Sensors for Hand Gesture Recognition. *Front. Neurorobotics* **2020**, *13*, doi:10.3389/fnbot.2019.00114.

XII. **Esposito, D.**; Gargiulo, G.D.; Parajuli, N.; Cesarelli, G.; Andreozzi, E.; Bifulco, P. Measurement of muscle contraction timing for prosthesis control: a comparison between electromyography and force-myography. In Proceedings of the 2020 IEEE International Symposium on Medical Measurements and Applications (MeMeA); 2020; pp. 1–6.

XIII. Andreozzi, E.; Fratini, A.; **Esposito, D.**; Naik, G.; Polley, C.; Gargiulo, G.D.; Bifulco, P. Forcecardiography: A Novel Technique to Measure Heart Mechanical Vibrations onto the Chest Wall. *Sensors* **2020**, *20*, 3885, doi:10.3390/s20143885.

XIV. **Esposito, D.**; Gargiulo, G.D.; Polley, C.; D'Addio, G.; Bifulco, P. Improvements of a Simple Piezoresistive Array Armband for Gesture Recognition. In Proceedings of the 2020 International Conference on e-Health and Bioengineering (EHB); October 2020; pp. 1–5.

XV. Cosenza, C.; Nicolella, A.; **Esposito, D.;** Niola, V.; Savino, S. Mechanical System Control by RGB-D Device. *Machines* **2021**, *9*, 3, doi:10.3390/machines9010003.

XVI. **Esposito, D.**; Savino, S.; Andreozzi, E.; Cosenza, C.; Niola, V.; Bifulco, P. The "Federica" Hand, submitted to *"Research in Biomedical Engineering (Springer)"* - under revision

XVII. **Esposito, D.;** Savino, S.; Cosenza, C.; Andreozzi, E.; Gargiulo, G.D.; Polley, C.; Cesarelli, G.; D'Addio, G.; Bifulco, P. Evaluation of Grip Force and Energy Efficiency of the "Federica" Hand. *Machines* **2021**, 9, 25, doi:10.3390/machines9020025.

XVIII. Centracchio, J.; Sarno, A.; **Esposito, D.;** Andreozzi, E.; Pavone, L.; Di Gennaro, G.; Bartolo, M.; Esposito, V.; Morace, R.; Casciato, S.; et al. Efficient Automated Localization of ECoG Electrodes in CT Images via Shape Analysis. *Int J CARS* **2021**, doi:10.1007/s11548-021-02325-0.

XIX. Andreozzi, E.; Fratini, A.; **Esposito, D.;** Cesarelli, M.; Bifulco, P. Toward A Priori Noise Characterization for Real-Time Edge-Aware Denoising in Fluoroscopic Devices. Submitted to *"BioMedical Engineering OnLine"* – under revision.

CONTENTS

Thesis outline

Chapter 1 introduces the problem of the upper limb deficiency and the principal typologies of active prosthetic hands; particular emphasis is firstly given to EMG strategies for prosthetic control [V], and then to force-myography (FMG) technique as alternative to EMG, in muscle contraction monitoring and prosthetic control [III]. This chapter ends introducing the "Federica" prosthetic hand project [XVI].

Chapter 2 presents a single-point muscle force sensor and its performances with respect to the EMG, in muscle contraction detection and prosthetic control applications [III]. A circumference muscle force sensor is also presented and evaluated in comparison with the EMG [I].

Chapter 3 describes the current state-of-the-art of the "Federica" hand: the underactuated mechanical system, the FMG control system and the vibrotactile sensory feedback of the grip force [XVI].

Chapter 4 shows the performance tests carried out on the "Federica" hand, for evaluating: the FMG control; the activation speed; the power grip force and the energy efficiency of the prosthetic mechanical system. Preliminary experimental tests, on both heathy and amputee subjects, are also reported [VIII,IX,XII,XVII].

Chapter 5 proposes a new design of the "Federica" hand and the thesis conclusions [XVI].

Finally, Chapter 6 presents future trends and applications: an array armband of single-point muscle force sensors, for gesture recognition and prosthetic control purposes [XI,XIV].

Chapter 1

Introduction

1.1 Upper limb deficiency and prosthetic hands

The upper limb can be described as a system whose main effector organ is the hand, thanks to which man is able to perform an extremely wide variety of functions and skills that are used in the various activities of daily living, working and sports. Conditions that may require a prosthetic hand substantially include amputations and congenital malformations. The design of prosthetic hand is therefore a very complex process, which had in recent years a number of developments and improvements [1,2]. Despite this, there are still many aspects that can be improved and refined so that the user can have a simple prosthesis to be controlled, comfortable to wear and aesthetically pleasing.

In general, active prosthetic devices can be body powered or electric powered [3]. The body-powered devices are activated by means of a Bowden cable anchored to the controlateral shoulder harness: the user by pulling the cable with shoulder movements, performs the opening in the voluntary opening devices [4], or the closure of the prosthesis in the voluntary closing devices [5]. The advantages of body-powered devices are that they are low-cost and are less expensive to repair. However, these devices are not cosmetically appealing and are difficult to operate by some users due to the physical force required. The electric-powered prosthetic devices are usually supplied by batteries and are desired by most of the users because their versatility and their cosmetic appearance [3].

1.2 Electromyography (EMG) for prosthetic control

Active prosthetic devices provide many more functional capabilities to amputees with respect to those of simply aesthetic, body-powered or passive devices. User intention for prosthesis control is generally obtained by monitoring physiological signals, which are acquired through different sensors. Although various signals can be used in prosthetic control (such as switches, pressure, electroencephalography, etc.) and electromyography (EMG) is by far the most used signal.

Surface electromyography (sEMG) is generally used for monitoring muscle contraction [6], and it can provide a non-invasive way to detect the muscles electrical activity from the residual limb; sEMG signal is a bipolar, symmetric distribution of positive and negative amplitudes, and can range between ± 5 mV, showing most frequency power between 20 and 150 Hz. It is also called "interference pattern" for its random shape. In fact, raw EMG spikes cannot be precisely reproduced in exact shape, due to the constant changes of the recruited motor units and their activation frequencies. However, by applying a smoothing algorithm (e.g. moving average) the non-reproducible contents of the signal are eliminated or at least minimized.

Several external factors can influence the EMG recording, by altering its shape and features: tissue characteristics (thickness, muscle physiological changes and temperature); physiological cross talk (EMG signals from neighbouring muscles under the local electrode site); changes in the geometry between muscle belly and electrode site; external noise (e.g. power line 50/60Hz interferences); noise from electrodes and biopotential amplifiers [7]; etc.

EMG can reveal detailed information about the timing and the magnitude of muscle activation. Indeed, the average amplitude of the EMG signal is a good indicator of the level of muscle activity, due to the increase of the active motor units numbers, the frequency of their activation or the firing rate [6]. Therefore, in order to measure activation level and timing, the EMG linear envelope (EMG-LE) is usually computed [8]. Generally, the raw EMG signal, detected by means of electrodes, is rectified and then low-pass filtered. Alternatively, the envelope can be obtained using a moving window on the raw EMG, in which the root-mean-square (RMS) is computed. The EMG envelopes give a measure of the local power of the signal and produce a much simpler waveform that is easily analyzable. Although the EMG-LE is a band-limited signal with frequency content very close to the DC mean (limited to the interval 0-5 Hz), it actually represents the average variations of the energy of the EMG signal and is normally used to control prostheses [6,9,10].

Since prosthesis control requires a continuous monitoring of patient's muscle activity, in practical application the EMG should be acquired by using dry electrodes, embedded in the socket of the prosthesis. The conductive gel generally used to improve electrode performance and stability cannot be used for long recordings, since the gel tends to dry and change its characteristics over time: this greatly degrades the quality of the recorded EMG signal [11]. Stainless steel or even textile [12] electrodes can be used instead , but these cause problems for the biopotential amplifier [7]. Furthermore, stable mechanical placement of electrodes onto skin, skin properties and motion artifacts [13] are other issues to be considered. Because of these problems, the commercial state-of-the-art myoelectric interface uses two EMG channels [6,7,8].

Figure 1 presents the principle strategies used to exploit the EMG signal for prosthetic control [17,18].

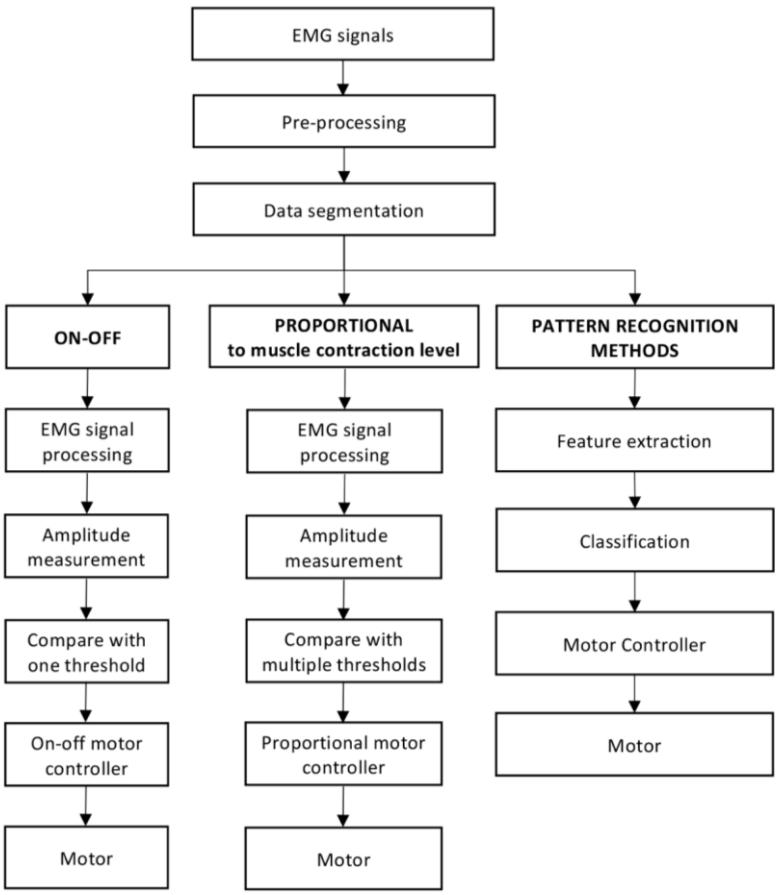

Figure 1. Principal methodologies to exploit the EMG signals for prosthetic control.

In the conventional on–off control, once a pre-established EMG threshold is reached, the prosthetic hand is operated with a constant speed (independent from the muscle contraction level) until to the complete hand closure. In proportional control, in function

of an increasing muscle contraction level (i.e., EMG amplitude), a gradual closure of the prosthetic hand is achieved [17,18].

EMG Pattern Recognition (EMG-PR) techniques have been developed to increase the dexterity of myoelectric prosthetic devices, and to overcome the limitations of conventional proportional control. EMG-PR operates by extracting multiple features from EMG signals rather than entirely relying on EMG amplitude [19] (as EMG amplitude is slow, cumbersome and difficult for users to control their residual muscles movement). A well-developed artificial upper limb design comprises of trajectories of a limb and their associated movement patterns. To delineate this, a control algorithm requires parameters such as kinematics and models of joints [20], motion and activities range [21]. Through EMG-based pattern recognition, researchers are working on the hypothesis that EMG patterns contain much information on intended movements. Once the EMG patterns are identified for intended movements by using a specific classifier, the prosthesis controller will receive the command to implement the movement. Thus, EMG-PR approach may allow users to control their myoelectric prosthesis more effortlessly with a broad range of control.

The use of artificial hands instead of biological hands with the same degree of dexterity [22] and complexity is a challenging task. However, pattern recognition (PR) technology has played an important role in controlling myoelectric prosthetic devices for over 20 years [23,24]. Pattern recognition technology provides more natural control, which is easier to learn by user and machine. It also provides independent control of multiple DOFs using simultaneous, sequential or semi-sequential control, as well as bringing the prosthesis closer to natural arm functions [25]. By applying proper PR-based methods and signal processing techniques in combination with machine learning algorithms, an amputee's limb movement can be accurately decoded and used to control a prosthetic device [21,26]. EMG-based PR methods involve various approaches such as pre-processing, segmentation of data, feature extraction, feature classification and post-processing [27] (see Figure 2).

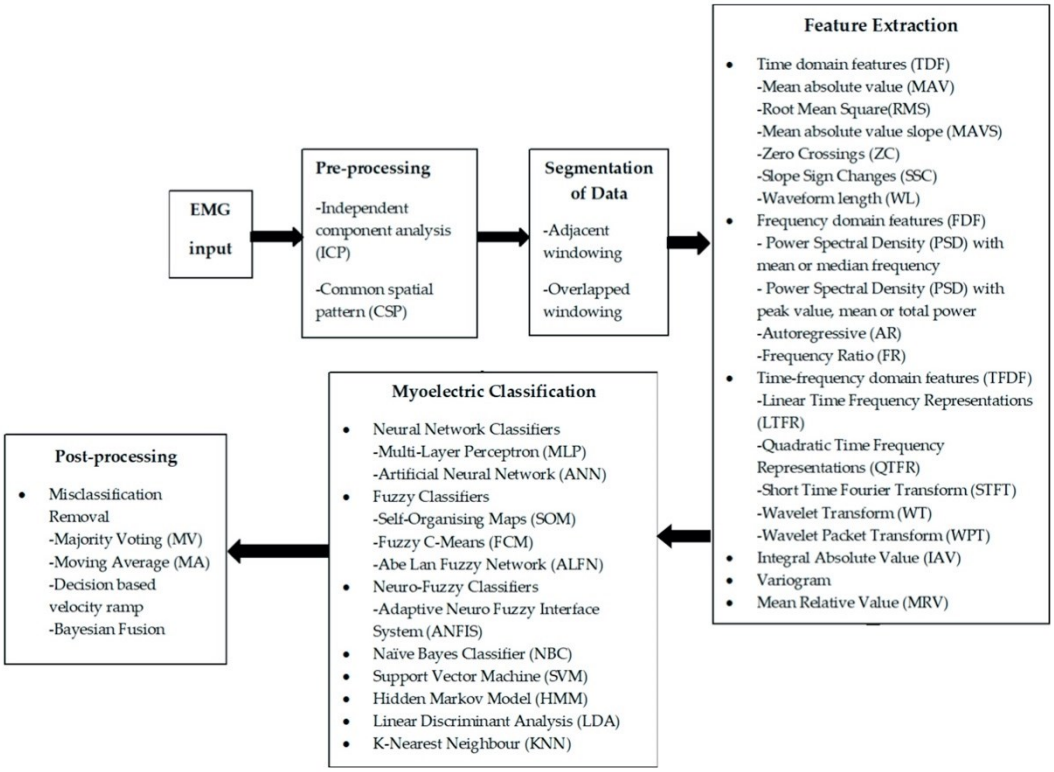

Figure 2. General pattern recognition scheme (extracted from [28])

All these approaches related to myoelectric pattern recognition in one way or another can be helpful, but these methods still need further real-time evaluations for their validity [29]. Much research has been done on the myoelectric prosthesis; nevertheless, some of the areas in the field need to be improved: (i) control of multiple degrees of freedoms (DOFs) naturally and intuitively, (ii) two-way communication with the brain (peripheral nervous system (PNS)) and iii) fast learning. Moreover, several advanced pattern recognition techniques have been proposed without any real-world user applications [30,31]. A large portion of pattern recognition techniques described in the literature is still being applied in clinical settings. Moreover, the performance of these algorithms is affected greatly by several factors, including the positioning of electrodes, the fatigue of the muscle, arm position, surface EMG cross-talk and muscle contraction.

1.3 Mechanomyography (MMG) and Force-Myography (FMG)

Different mechanical features can be used to monitor muscle activation. Muscle contraction is generally associated with muscle shortening, increase of cross-section areas, increase of stiffness and tension, mechanical vibrations, and other mechanical parameters. Mechanomyography (MMG) can be regarded as the mechanical counterpart of the EMG [32,33], and is based on the recording of muscular vibrations produced by an active muscle. It can be used as a monitor of muscle stiffness and can be related to muscle force exertion [34]. The amplitude of the MMG signal may be related to the number of active motor units (i.e., motor unit recruitment) [33]. Different types of sensors can be used to measure the MMG signal: condenser microphones [33,35,36], piezoelectric contact sensors, accelerometers [33,37–40], and, more recently, laser distance sensors [33], placed in contact with the patient's skin. Tensiomyography is another technique used to estimate a muscle's mechanical properties, and it does so by measuring the radial enlargement of the muscle belly and detects muscle contractile properties [41–43].

Mechanical muscle contraction can be measured in many ways [44], including: Strain gauges [45]: muscle contractions which cause direct stretching of the sensor; Change of electrical impedance of the muscles [46]: changes to global muscle resistivity when it goes from a resting state to an activity state, due to blood afflux in the muscles; Muscle circumference sensor [47,48]: where muscular contraction is proportional to the changing of cross-sectional areas of the muscles, around which the sensor is positioned; A resonance-based active-muscle stiffness sensor [49]: where piezoelectric probes are used to measure stiffness changes in muscles; Ultrasound scanners [34,50]: where ultrasound probes are employed to evaluate the morphological changes in muscle thickness or displacement; A small permanent magnet fixed on the skin, in conjunction with a Hall effect device, used to measure changes in muscle dimension [51]; Pneumatic sensors [31]: muscular activity detected by measuring changes in air pressure in an air-bladder contacting the muscle; Change in optical properties [52]: LEDs and photodiodes can be combined to detect muscle contraction by measuring the backscattered light from the muscle tissue; Textile pressure sensors enclosed in garments [53].

In particular, some previous studies [54,55] reported the use of force-sensitive resistors (FSR) to acquire information about muscle activity, however, they could only provide qualitative results or simple information about on-off muscle activation. They used bare FSR sensors laid onto the patient's skin, and no quantitative comparisons with

other, more well-assessed signals proportional to the intensity of muscle contractions (as the EMG) were made.

It is worth emphasizing that EMG reflects the electrical, not mechanical events of muscle contraction. In fact, EMG represents the propagation of motor unit action potentials along muscle fibers, which is only the initiator of the muscle mechanical activity, followed by chemical and mechanical events [56] which take place before the muscle actually exerts force.

Indeed, there are many consecutive steps in the excitation– contraction pathway. The onset of muscular force is triggered by the depolarization of the fibres (EMG), but must involve the release of calcium from the sarcoplasmic reticulum, its binding to troponin, the cross-bridge between actin and myosin filaments and the sliding of these two proteins. Other events in the muscle relaxation process, such as the off-rate of actin myosin cross-bridges and the time occurring for uptake of calcium by the sarcoplasmic reticulum, will determine the time delay between the end of the EMG signal and the end of force production. This phenomenon is known as electro-mechanical delay (EMD), that is the time lag between the EMG onset and the beginning of force generation [56]. Similarly, the latency between the end of the EMG signal and the beginning of force fading, occurs during muscle relaxation [57], that is known as the relaxation electromechanical delay (r-EMD) [58]. Again, chemical and mechanical events occur [56]. Moreover, while muscle contraction is an active process, relaxation is passive, and other biomechanical events (e.g., action of antagonist muscle and/or other external counteracting forces) have to be considered also. Simultaneous recordings of EMG, MMG, and force (or torque) can accurately evaluate such electromechanical delays [59–61].

In the vast majority of applications involving measurement of muscular contraction levels (such as prosthesis control), EMG-concise information, such as the EMG-LE is still used. However, the aforementioned problems (see section 1.2) related to EMG collection (i.e., electrodes, interferences, motion artifacts, etc.) have stimulated interest in other types of sensors, such as those sensitive to the muscle mechanical activity, but nothing has proved so effective to offer a reliable replacement for the EMG-LE. Factors such as ease of use, stable positioning on patient, size, robustness, durability, wearability, cost, energy transmitted to the patient, electrical connections with the patient, etc. have hindered its extensive usage.

In exchange, a new muscle force sensor that overcomes many of these limitations was presented in [62]. It is based on a slim force-sensitive resistor mounted on a purposefully designed mechanical coupling system, driven by a specific conditioning circuit. The custom force sensor is extremely simple and easy to use, and is able to record the muscle cross-sectional changes, thus providing a signal (referred to as force-

myogram, FMG), extremely similar to the EMG-LE. The force sensor should be positioned above the muscle belly (and not on tendons), where EMG is generally taken. This easily enable to exploit or to adapt other EMG based techniques. In both cases (EMG and FMG), the muscles should be superficial and not deep, to allow advantageous signal-to-noise ratio.

Such high similarity suggested the potential use of FMG as an alternative to EMG for prosthesis control. FMG offers some advantages over EMG: no need for electrodes and stable electrical contact; much lower susceptibility to electromagnetic interferences; no need for signal processing to obtain a reliable control signal (the FMG signal can be used as is); simpler conditioning circuit; extreme compactness and thinness of the sensor, which improves wearing comfort; lower cost. Furthermore, the simplicity of FMG signal made possible the use of low cost and open-source Arduino boards as prosthesis controllers.

The new muscle force sensor went through a preliminary test as a replacement of an EMG sensor to control an active prosthetic hand named “Federica”(see Figure 3).

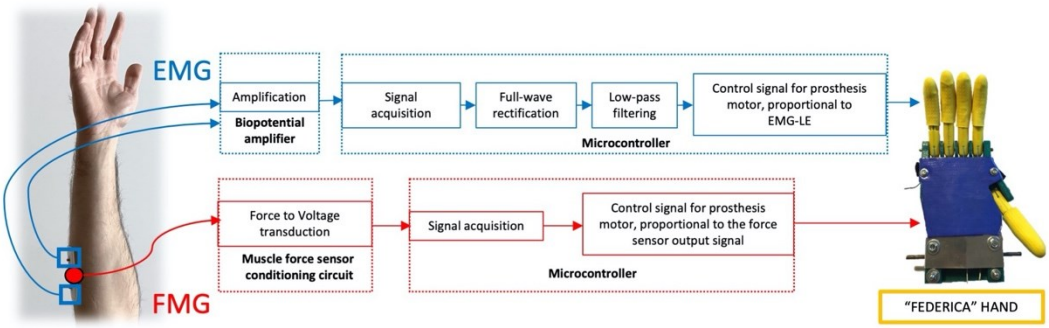

Figure 3. Flow chart comparing EMG and FMG for prosthetic control applications.

1.4 The “Federica” hand project

The hand loss is a traumatic event, which involves the loss of motor and sensory functions, with inevitable disabilities. Hand prostheses are intended to restore both the appearance and some functionalities of the hand, in people with amputations or congenital malformations. Especially in poor and developing countries, there may be several causes of amputation, associated with trauma due to wars, explosives, industrial or environmental accidents, the consequences of which are often aggravated by the lack of public health care. All over the world, many people cannot afford high-tech, commercial hand prostheses, so various low-cost solutions have been proposed. Local availability of materials, ease of realization, effectiveness, robustness, durability, and free access to the hardware and software should be taken into account in the design process. The "Federica" prosthetic hand was specifically designed to meet these needs. “Federica” restores the grasping functions that are the most useful in everyday life. Its design is focused on achieving an energy efficient operation, as well as providing a fast and responsive control system with sensory feedback capability, that allows the user to rapidly get confident with the prosthesis control. An ad hoc designed mechanical system, together with a novel technique to monitor muscle contraction (FMG control), provide very fast grasping functions, also simplifying the learning curve for the user. During the design process, the low cost of realization has been pursued by conceiving almost all components to be 3D printable (only one off-the-shelf servomotor must be purchased); also, the modularity has been promoted in the design to simplify the assembly, maintenance and repair operations.

“Federica” is powered by a single servomotor and performs the grasping function by means of a custom underactuated differential mechanical system. Many underactuated mechanical systems (less actuators than degrees of freedom (DOF)) have been proposed to simplify the control of hand prosthesis, without renouncing to mimicking the dexterity of some natural hand movements. Underactuated mechanisms aim to reduce the number of active DOF and to reproduce common hand action, without increasing mechanical and control complexity [63]. Moreover, underactuated mechanisms do not control a single element (e.g. a phalanx), but rather a set of elements (e.g. a finger or some fingers).

Examples of underactuated systems include floating pulley trees and differential gearings. These systems turned out to be very useful in grasping tasks, where the fingers should be able to conform with irregular shaped objects [64]. Different studies presented prosthetic devices with multiple DOF, controlled with a limited number of actuators and a differential mechanism. The resulting underactuated mechanism allows to transfer the motor force from few actuators to many phalanxes, taking advantage of self-adaptive grip

capacity and a lower manufacturing cost [65]. Adaptive grasp is the ability of the fingers and thumb to adapt to the shape of an object, in order to increase the contact points between the hand and the object [63]. A reduced number of actuators also implies simplification of the prosthetic control system and can be advantageous for the patient. The user would prefer to send few, fast and direct commands to the prosthesis in performing normal daily activities, without the need to commit to much in the control [63].

A specific underactuated mechanism [65] was presented to control five fingers (15 DOF) by means of one actuator, with the aim to grab complex shaped objects and to allow appropriate force distribution. Each finger has three compliant joints, with rotation and spring functions, that are not suitable for grabbing heavy objects, because they can easily be abducted or adducted [65]. Another prosthesis, named TUAT/Karlsruhe humanoid hand, adopted a mechanism for the cooperative movement of finger and palm joints [66]. In order to realize the function to operate each finger individually, without losing the conventional grasping function, the main servomotor cooperate with six small servomotors arranged between metatarsals. By using springs or rubber bands, each finger can return to its rest position [67]. A three fingered prosthesis, called SPRING hand [63], showed to be capable of self-adaptive grasp by means of an underactuated mechanism. The eight DOF of the hand are driven by one motor, and each finger includes cables and springs, in order to guarantee the shape adaptation to the grasped object [63]. A project entitled KIT Prosthetic Hand [68], presented an underactuated system in which the four fingers are simultaneously driven via a force-distributing transmission based on the TUAT/Karlsruhe mechanism [66,67], while the thumb is actuated by a second motor. Custom made springs in every joint ensure the passive reopening of the fingers [68]. A mechatronic hand with five fingers controlled by a single actuator, showed to be able to perform four types of grasps, and to switch between them by means of a bistable ratchet coupled to thumb adduction/abduction [64].

All the aforementioned devices [21–25] made use of underactuated mechanical systems combined with springs and/or elastic elements, which unavoidably absorb a considerable amount of energy supplied by motors when hand closes . In general, elastic elements are used for the passive opening of the hand (i.e. extension of the fingers), while, during the closing of the hand (i.e. flexion of the fingers), springs have to be loaded and this requires energy expenditure.

However, multiple DOF devices with multiple actuators, were also presented by other studies. An example is the fully actuated ROBIOSS hand [69], consisting of four fingers each with 4 DOF, driven by 16 actuators; another example is the doubly actuated

Utah-MIT hand [70], which includes four fingers each with 4 DOF and 3 DOF wrist, driven by 38 separate actuators. Obviously, the complexity of both the mechanics and the control are considerably increased with respect to the underactuated devices.

A further issue addressed in the "Federica" hand project was the development of a system to provide a non-invasive sensory feedback of the grip force. The amputation involves the loss of sensory receptors and the interruption of the physiological channels, through which stimuli are normally perceived and transmitted to the central nervous system (CNS) [71,72]. Restoration of the sensory function, is an important challenge faced by prosthesis designers. There are two possible ways to elicit sensory feedback [71,73,74]: invasively, by using neural electrodes implanted in the peripheral nervous system, in afferents originally serving the fingers and palm, in order to directly interface with the CNS; or non-invasively, by providing feedback to residual sensory systems (e.g. electrotactile and vibrotactile stimulations on the residual limb, etc.). In both cases, the user should be trained to associate stimuli with physical events occurring at the prosthesis (exteroception) or to states of the prosthesis (proprioception) [71,73]. A prosthesis with sensory feedback realizes a closed-loop control, providing the user with both exteroceptive and proprioceptive information. However, commercial hand prostheses used in clinical practice are generally not equipped with such closed-loop control and, consequently, the user needs to rely on visual feedback and incidental stimulation (hearing, socket pressure, etc.) [71]. An exception is the VINCENTevolution2 prosthetic hand, which is equipped with haptic feedback [72,75]. Other devices like Sensor-Hand, i-Limb and BeBionic use sensors to measure and automatically regulate the grip force without having the user in the loop; in particular, i-Limb and BeBionic exploit motor current sensors with the aim to achieve an adaptive grasp [71]. Nevertheless, experimental projects mainly proposed electrotactile and vibrotactile stimulations, in order to code information relative to the grasp and provide the user with a non-invasive sensory feedback [71]. Electrotactile stimulation evokes sensations by passing a local electric current to stimulate afferent nerve in the skin with surface electrodes. The modulated parameters include frequency, amplitude and pulse width [74]. Electrocutaneous feedback can cause pain in the user, and can also create interferences in prostheses controlled by EMG signal [73]. Vibrotactile stimulation is achieved by providing the user with a mechanical vibration on the skin to convey a tactile sensation [74]. The two main features of the stimulus are vibration amplitude and frequency [71]. The use of vibrotactile feedback was reported to improve user performance, by achieving better grip force control and less errors in performing daily activities [71].

A different approach to provide sensory feedback is based on mechanotactile stimulation, consisting in a force/pressure applied in a different area (the residual limb)

from the original stimulus [74]. An example is an elastic armband connected to two DC motors [76], which rotate in opposite directions to tighten or loosen the band, in order to help the user adjust the gripping force. Current mechanotactile devices are more cumbersome and heavier than vibrotactile or electrotactile devices, also resulting in higher energy consumption [74].

However, sensory feedback could encourage the sense of body ownership for prosthetic users and help them to correctly apply force in the grip; therefore, restoring a kind of tactile sensation is helpful in improving the user experience as well as the handling performances [74].

The current doctoral dissertation presents the "Federica" hand, a very low-cost prosthetic device powered by a single servomotor and able to easily and quickly grab object of any shape. The whole project and all its components are openly presented in detail, to clearly show all the adopted solutions and to allow their reproduction. For this purpose, a recent study (submitted to Research in Biomedical Engineering – Springer and under review) provided with the supplementary materials, the CAD files for 3D printing and the Arduino script for the control system. Further information about the "Federica" hand project are available on a webpage [77].

Chapter 2

FMG and MMG as alternatives to EMG in muscle contraction monitoring

2.1 Single-point Muscle Force Sensor

2.1.1 Sensor Design

Muscle contraction is associated with volumetric and stiffness changes, which exert radial forces (or pressures). A force-sensitive resistor (FSR) placed on a patient's skin in correspondence with a muscle belly was used to sense contraction. Generally, FSRs consist of a conductive polymer, which changes its resistance when a force is applied to its surface. They can be made small and very thin (e.g., less than 0.5 mm), offer good shock resistance, can operate in moderately hostile environments, and are low-cost. However, there should only be concentrated and uniformly distributed force within the FSR active (or sensing) area for reliable use of the FSR. The assembling of the Interlink FSR [78] includes perimetral spacers that separate the two membranes holding the metallic contacts and the conductive polymer (see Figure 4).

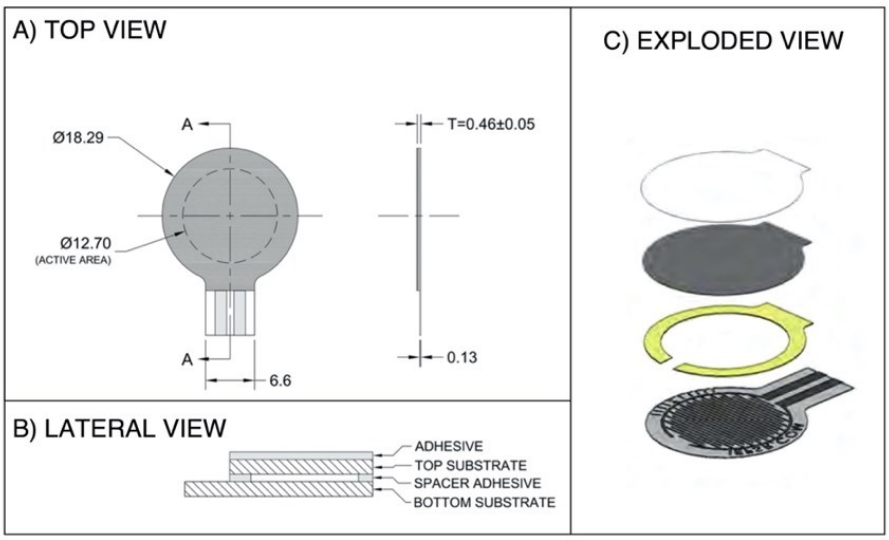

Figure 4. Force-sensitive resistor (FSR) 402 short: A) Top view; B) Lateral view; C) Exploded view.

A direct application of the FSR on skin to sense muscle contraction proved to be quite unsatisfactory. The mere sensor, without any mechanical coupler, provided uncertain and unreliable results. Contact with the patient's skin was unstable and uncertain—the perimetral spacers of the FSR sensor transmits part of the applied force directly to the back of the sensor without involving the sensing area, and prevents the membrane with electrical contacts from properly flexing onto the resistive polymer layer. A specific mechanical coupler was designed in response to these drawbacks (see Figure 5). A rigid spherical cap, made of acrylic resin, provides advantageous force transmission to FSR. The spherical cap base was glued onto the FSR's sensitive area (leaving out the perimetral spacers) and its convex part was made to face the patient's skin. When the sensor is applied onto the patient, the dome creates a little subsidence that gently but firmly attaches to the skin. Furthermore, a flat, rigid sheet of plastic was attached to the back of the sensor to prevent improper bending. The elastic modulus of both the spherical cap and the back support were much higher than that of skin and muscle. The mechanical coupler provides a much more convenient and reliable muscle force transmission to FSR.

The assembly of the FSR and the mechanical coupler can be held in place onto a patient's skin by a belt or other fastening methods (e.g., scotch tape). The increase of muscular transverse section during contraction, as well as the resultant skin stretching, impresses uniform pressure on the FSR active area via the rigid spherical cup. Furthermore, the small mechanical vibrations generated during muscle contraction (i.e., the mechanomyography MMG signal) are suitably transmitted to the FSR sensor.

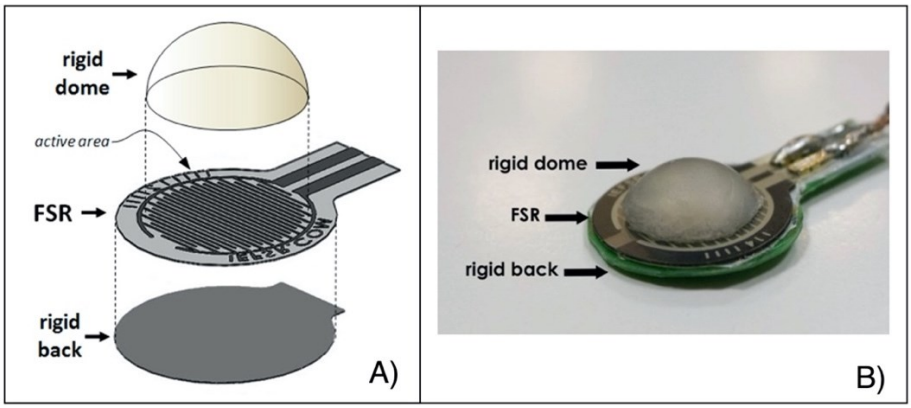

Figure 5. A) Exploded view of the mechanical components of the force-sensitive resistor (FSR)-based muscle sensor. B) A picture illustrating the FSR sensor and the rigid dome mounted above.

2.1.2. Sensor Conditioning

The use of conductive polymer composites as force sensors in robotic and biomedical applications [79,80] has been limited due to their low accuracy and repeatability in measuring absolute force (or pressure) compared to load cells. Some recent studies have modelled in detail the rheological behaviour of the insulating polymer matrix in which conductive particles are dispersed [81,82], and highlighted the role of the voltage across the sensor. When an FSR is subjected to constant loading for an extended period of time, mechanical creep behaviour can be observed in the physical dimensions of the specimen due to the rheological characteristics of the polymer. The creep affects the inter-particle separation, as well as the electrical resistance of FSR (see quantum tunneling operation mode [83])—this produces a drift of the sensor output. However, the sourcing voltage across the FSR sensor plays an important role in the output drift.

The sensor datasheet [78] primarily reports a simple voltage divider circuit (a series of FSR and fixed resistors as depicted in Figure 6) for FSR conditioning. The voltage divider configuration [54] is mostly used for its simplicity, and is often supplied by the voltage available from microcontroller boards (e.g., 5 V).

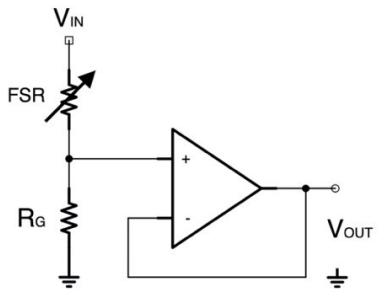

Figure 6. FSR sensor conditioning by means of a voltage divider circuit (as suggested by Interlink datasheet [84]).

However, the voltage divider configuration does not ensure a constant voltage across the sensor (it may swing from a few millivolts up to 5 V)—such configurations increase and complicate sensor drift, yields sensitivity degradation, and provides much poorer measurement accuracy and repeatability. Thus, using voltage divider conditioning circuits have been discouraged [85], and a constant voltage should be used instead. The FSR conditioning circuit was designed using an op-amp trans-impedance amplifier (see Figure 7). This circuit maintains a constant voltage across the FSR, performs a current-to-voltage conversion, and makes the FSR sensitivity constant over a wide input force range. It was observed that if the FSR voltage is about a hundred mV (140 mV for the Interlink FSR 402 sensor [82]) there is a non-linear relationship between the FSR current and voltage. Furthermore, it was observed that by increasing the voltage, the drift would tend to reduce [85]. However, joule self-heating of the sensor suggested reduction of the supply voltage, and the non-linear phenomena of sensitivity degradation [79] could also be observed when an FSR, supplied with a voltage greater than 2 V [85],was subjected to cyclic loading. Therefore, a good compromise to minimize drift and preserve sensitivity is to supply the FSR sensor with a constant voltage of 2 V.

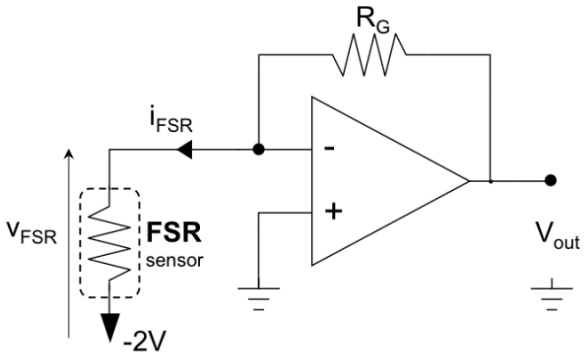

Figure 7. Conditioning circuit for the FSR sensor, based on op-amp-trans-impedance amplifier.

With reference to muscle contraction sensing, the large time constant of the mechanical creep and the sensor drift (about 500 s [85]) should be compared to muscles' activation intervals, which are usually much shorter. However, it is important for the sensor to have stable sensitivity over time [79,85] so that repeated or cyclic muscle contractions can be monitored. In conclusion, FSR sensor drift and sensitivity degradation, although not eliminated, can be effectively limited by means of appropriate FSR conditioning circuits.

2.1.3. Static and Dynamic test

Static calibration of the FSR sensor was performed to measure the relationship between force and voltage output (using the conditioning circuit of Figure 7). Different weights were applied onto the FSR sensor, and the resulting voltages were recorded. The weights were sequentially and perpendicularly applied to the active area of the sensor (on the top of the spherical cup), while the sensor was placed on a precision electronic scale that measured the actual force impressed.

The results of the static calibration of the FSR are presented in Figure 8. The gain resistor R_G (see Figure 7) was set to 700 Ω and the voltage V_{FSR} across the FSR to 2 V. The experimental measurements are represented as circles while the linear regression is represented as a continuous line. The angular coefficient of the regression line was 0.855, whereas the coefficient of determination R^2 of the linear regression was 0.99, proving a good fitting.

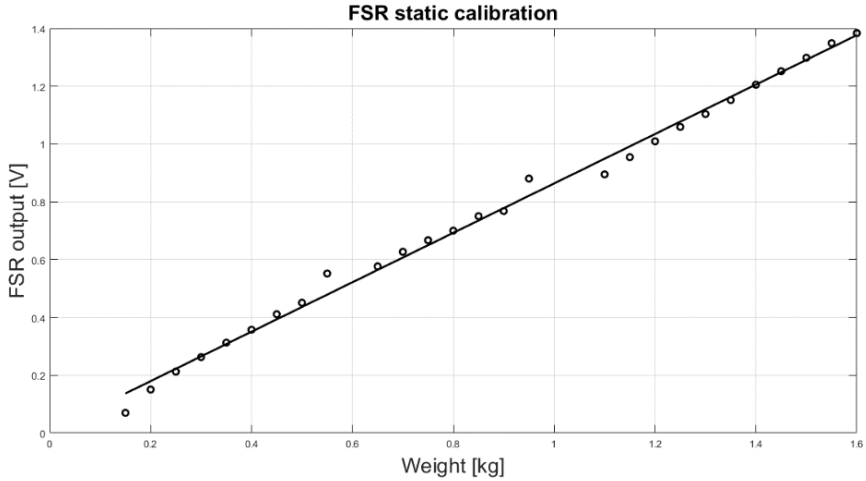

Figure 8. FSR static calibration: scatter plot of the experimental data (o) and regression line.

In addition, FSR sensor outputs were recorded for 200 s after the application of static loads in order to measure the actual drift achieved by the conditioning circuit. Drift was expressed as a percentage of variation from the expected value, according to the following equation:

$$Drift(t) = \frac{V_{FSR}(t) - V_{FSR}(0)}{V_{FSR}(0)} \times 100 \qquad (1)$$

where $Drift(t)$ is the normalized voltage drift in percentages; $V_{FSR}(t)$ is the voltage output of the FSR sensor at time t, and $V_{FSR}(0)$ is the sensor voltage immediately after the application of stress (i.e., the expected value).

The frequency response of the sensor was experimentally evaluated in order to test its ability to record rapidly varying signals, such as the MMG. A specific measurement set-up (see Figure 9) was designed and realized to practically measure the FSR sensor amplitude and phase response at different mechanical frequencies. A little electrodynamic shaker, supplied by a signal generator (Hewlett Packard HP 33120A) was mounted on top of the sensor, placed on a table. A precision accelerometer (PCB Piezotronics ICP 352B, sensor signal conditioner model 480C02) was fixed by screws onto the shaker (at the center of the upper part) to measure the acceleration of its mass. The weight of the shaker and accelerometer assembly was 315 grams. The actual force applied onto the sensor was obtained by multiplying the mass by the acceleration.

The shaker was driven by a sinusoidal voltage of increasing frequency (within the range of 1–2000 Hz, using 50 Hz steps) while the accelerometer signal and the voltage output of the sensor were sampled by means of an acquisition board (National Instruments NI USB-4431). Both signals were acquired at 100 kHz sampling frequency with 24-bit precision. The modulus of the FSR frequency response was determined by computing the ratio between the sensor output and the actual applied force, computed from the accelerometer data. The phase of the FSR frequency response was determined by measuring the time lag between the positive-slope zero-crossings of the applied sinusoidal force and of the FSR voltage output.

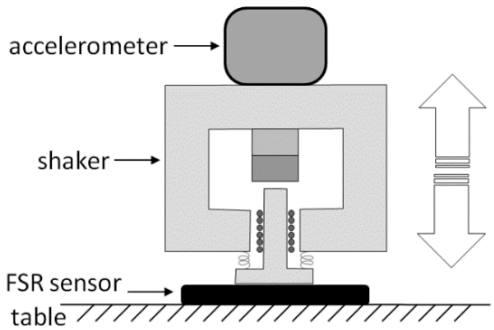

Figure 9. Experimental set-up to measure the frequency response of the FSR-based sensor.

Figure 10 shows the FSR-based sensor output drift at different loads. Constant weights of 400, 800, 1200, and 1600 grams were applied onto the sensor for 200 s. The sensor drifts were plotted as a percentage of the expected value. The drift amount did not correlate with loads, but was always confined below 8%. These measurements are compatible with the mechanical model of the sensor [85].

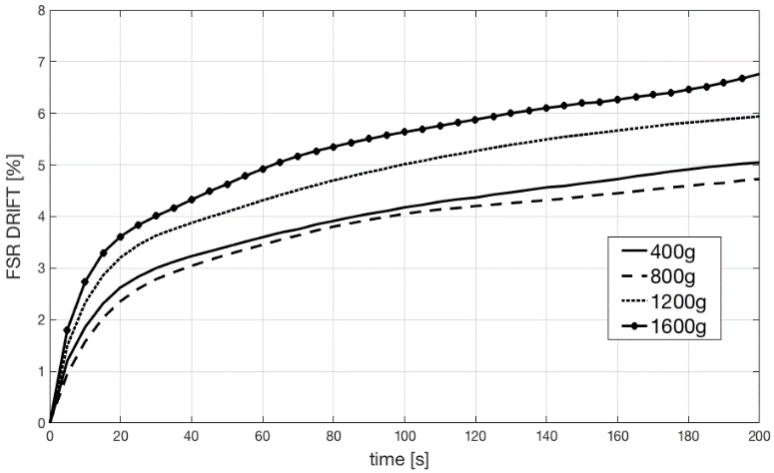

Figure 10. FSR drifts at different constant loads (400, 800, 1200, and 1600 grams).

Figure 11 shows the frequency response of the FSR-based sensor: the amplitude response is depicted in the upper panel, and the phase response in the lower panel. The amplitude response was flat, and the phase linear, up to 300 Hz. A mechanical resonance peak can be observed at about 700 Hz. The bandwidth of the sensor is more than enough to correctly represent the MMG signal, since the human MMG spectrum goes from 2 Hz up to 120 Hz [32,33].

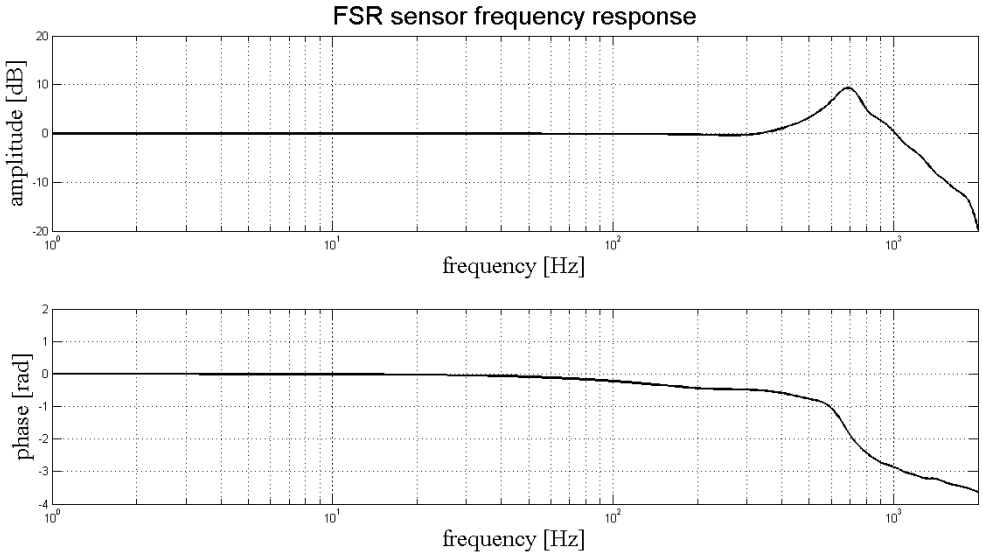

Figure 11. FSR dynamic response: amplitude (upper panel) and phase (lower panel) frequency response.

Discussion and Conclusions

A single-point muscle force sensor, able to detect both the force-myographic signal (FMG) and the mechanomyographic signal (MMG), was presented and tested in this study. The specific mechanical coupling and conditioning circuit allowed a quantitative and more reliable evaluation of the muscle contraction level with respect to previous studies involving mere FSR sensors [54,55]. The new muscle force sensor allows detection of muscle contraction and provides signals that can be compared to EMG–LE (taking into account the electromechanical delay). The new sensor is simple and ready for immediate use, is proportional to muscle contraction level, non-invasive, non-obstructive, easy to wear, robust, unaffected by electromagnetic interferences, and low-cost. Furthermore, it does not make use of electrodes, does not require any electrical contact with patients' skin, and does not need any signal processing to detect muscle contraction levels (only for MMG computing a simple high-pass filter is required). The FSR-based sensor is much simpler with respect to others (e.g., [31,45–52]) in measuring mechanical muscle variations during contraction.

However, the enclosed FSR shows drift errors caused by the mechanical creep of the polymeric matrix; these drawbacks can be reduced by using an appropriate conditioning circuit for the FSR. No experiment was carried out to evaluate FSR sensor performance during muscle fatigue.

In conclusion, the new FSR-based sensor can effectively monitor muscle contraction intensity and can be used as a valid substitute for EMG-LE to proportionally control prostheses or, more generally, for Human-Machine Interface (HMI) applications. The MMG signal provided by the sensor can be used to control prostheses too [35,37,39,86].

2.1.4 FMG – MMG – EMG detection from the same muscle

Introduction

Simultaneous measurements of EMG and the FSR-based sensor output were carried out on the forearm muscle of five healthy volunteer subjects (males aged 25–50) in order to achieve a quantitative comparison between the EMG linear envelope (EMG-LE) and the FSR-based sensor output.

Experimental Setup

Tests were performed on the flexor carpi ulnaris, a muscle involved in prosthetic hand control [44,87]. EMG electrodes and the FSR-based sensor were placed closed to each other on the belly of the muscle, as shown in Figure 12. The EMG signal was acquired by means of a biopotential amplifier (Biomedica Mangoni BM623) enabling a hardware 10–500 Hz band-pass filter. The two signals were simultaneously acquired at 10 kHz sampling frequency with 24-bit precision (using the National Instruments NI USB-4431). The EMG linear envelope (EMG-LE) signal was obtained by applying full-wave rectification followed by a low-pass filter (Butterworth 3-rd order, 5 Hz cut-off frequency). The mechanomyografic signal (MMG) was extracted from the FSR-based sensor's raw signal, that is the force-myographic signal (FMG), by applying a high-pass filter (Butterworth 3-rd order, 2 Hz cut-off frequency). Simultaneous signals were recorded when the subjects performed some voluntary muscle contractions of different intensity and duration.

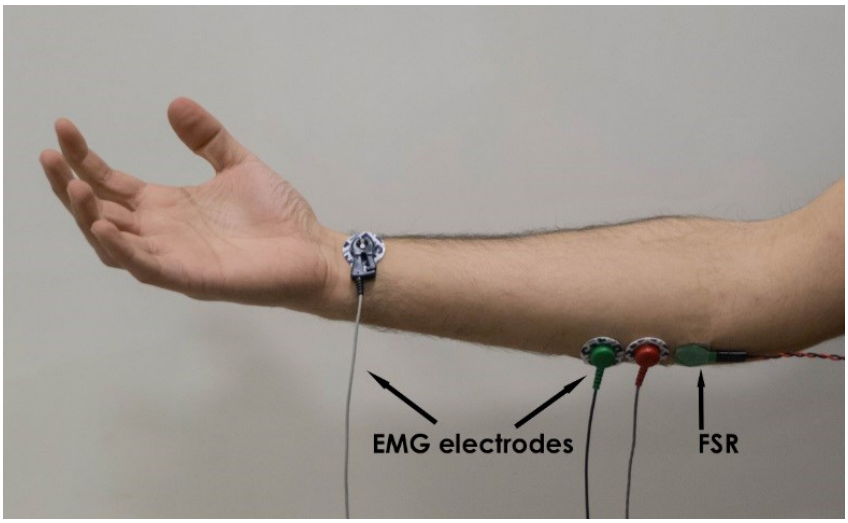

Figure 12. Electromyography (EMG) electrodes and FSR-based sensor placed on patient's muscle.

Results

The following are some of the results obtained when healthy subjects performed freehand grasping movements of different intensity and duration. As an example, Figure 13 shows simultaneous recordings of the EMG and the FSR-based sensor output (force-myographic signal (FMG)), as well as the computed EMG linear envelope (EMG-LE) and the MMG signal (computed from the FSR raw signal). The EMG linear envelope was plotted as a percentage of the maximum voluntary contraction (MVC), while the FSR signals were expressed in kilograms. Three separate muscle contractions of different intensity are clearly evident (each contraction starts at about 5, 31, and 58 s, see Figure 13). The third contraction corresponds to the maximum voluntary contraction (MVC).

There is clearly a good match between the EMG linear envelope and the FSR force signal. The Pearson's correlation coefficient "r" was computed between these two signals to quantitatively measure their similarity: it scored 0.9286 (p-value < 0.0001 (two-tailed test)). However, a delay of the force signal with respect to the EMG is particularly noticeable at the end of each contraction. This is probably due to the electromechanical delay, which is longer during muscle relaxation [58,61]. Thirty contractions of the subjects' flexor carpi ulnaris were analyzed, and the Pearson's correlation coefficients computed between the FSR output and the correspondent EMG-LE were always greater than 0.9.

As expected [32,33], the amplitude of the MMG signal corresponding to the central part of muscle contraction (excluding the start and the end) increases with the muscular strength. The standard deviations of the MMG signal computed in the central part of the contractions (i.e., from 7 to 14 s for the first contraction; from 33 to 40 s for the second contraction; and from 61 to 68 s for the third contraction, see Figure 13) resulted in 2.7, 5.2, and 7.0 grams, respectively. The main part of the MMG spectrum results were concentrated at between 2 and 20 Hz, in accordance to literature [32,33].

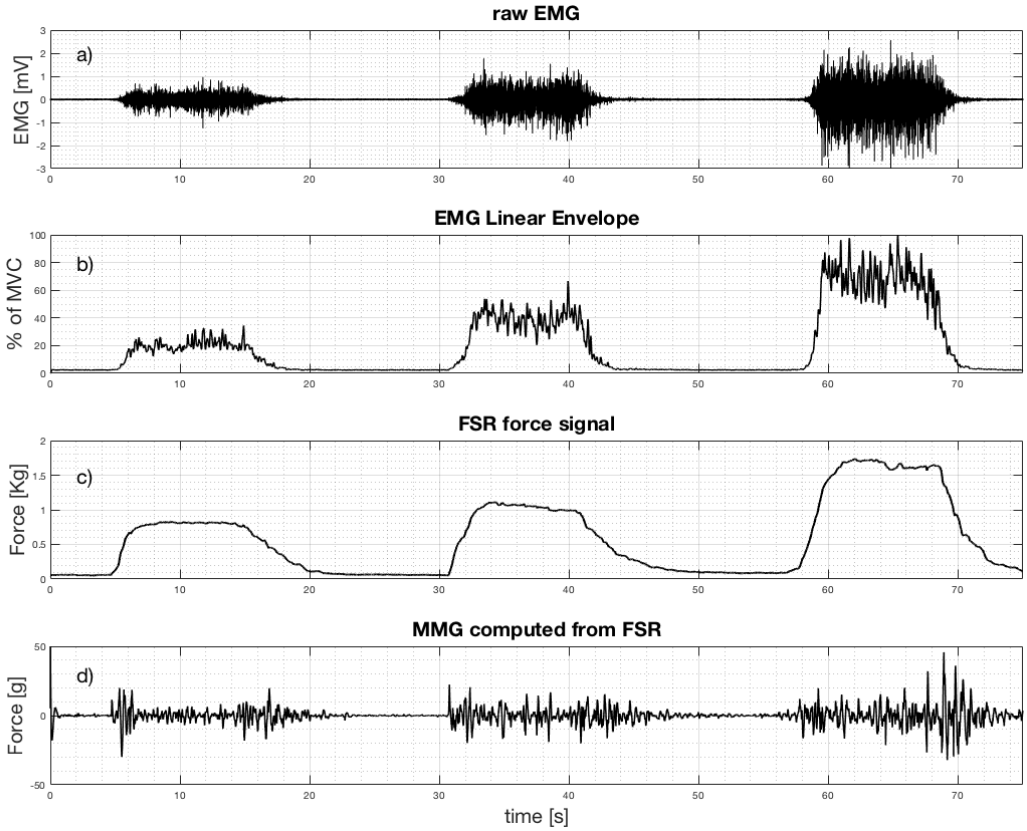

Figure 13. Simultaneous recordings from flexor carpi ulnaris when performing three grasp actions at increasing strength: (a) Raw EMG signal; (b) EMG linear envelope; (c) FSR raw signal (force-myographic signal (FMG)); (d) mechanomyogram (MMG) extracted from FSR.

2.1.5 FMG and EMG Comparison in Muscle Contraction Timing for Prosthetic Control

Introduction

The activation times required to trigger active prostheses, by using the EMG linear envelope and the force-myographic signal (provided by the FSR-based sensor) were in detail compared. Although the raw EMG signal always precedes the mechanical contraction, and therefore the signal detectable by the FSR, EMG signal must be processed in real-time with inevitable computational delays. On the contrary, the FSR signal can be used without any processing. To experimentally measure such delays, EMG and FSR signals were simultaneously acquired from the same muscle, opportunely processed and then compared. These time delays are particularly important when prostheses include fast acting mechanism that allow rapid interactions and, in general, for human machine interfaces.

Experimental setup

Practically, EMG and FSR signals were collected simultaneously from the forearm muscle “flexor carpi ulnaris”, while performing wrist flexion movements (see also [88]). FSR-based sensor was placed between the EMG electrodes on the belly of the muscle (see Figure 14). The FSR was fixed on patient’ skin by means of an elastic adhesive tape such the kinesio-tape. This allows to mount the sensor locally on the desired position of the skin, without the need of a band that wraps around the forearm. The EMG signal was acquired by means of a biopotential amplifier (Biomedica Mangoni BM623) enabling a hardware 20–500 Hz band-pass filter and a gain of 1000 V/V. The two signals were simultaneously acquired at 10 kHz sampling frequency with 16-bit precision by means of an acquisition board (National Instruments PCI-6251). The voluntary subjects were asked to vigorously perform wrist flexions as fast as they can, holding the position for a second or two and then returning in a relaxed state.

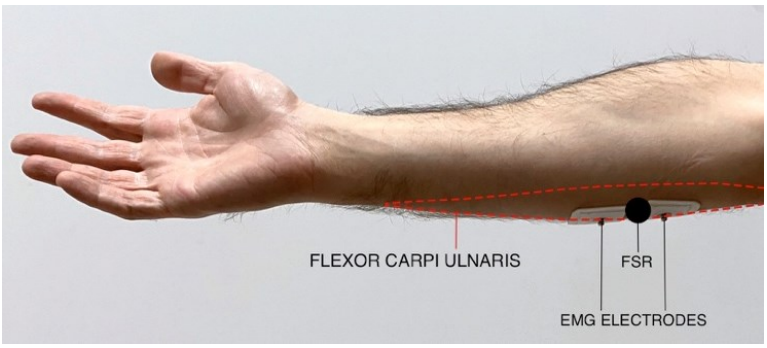

Figure 14. FSR-based sensor and EMG electrodes positioned on flexor carpi ulnaris.

Data processing

Different, classical techniques were applied on the raw EMGs to compute the EMG linear envelopes. In particular the following techniques were considered: a Moving Average (MA) low-pass filter with a time window set to a duration of 88ms acting on the rectified EMG; a Moving Root Mean Square (RMS) filter with a time window of 88ms; a 4th order Butterworth low-pass digital filter acting on the rectified EMG. All the filters were designed to exhibit the upper cut-off frequency (-3dB) to 5Hz (see Figure 15). This band was chosen as a good compromise between an acceptable variability of the EMG linear envelope and a fast tracking of muscle activation. Indeed, the proportional control of a prosthesis must not only consider the activation state of the muscle, but also its level.

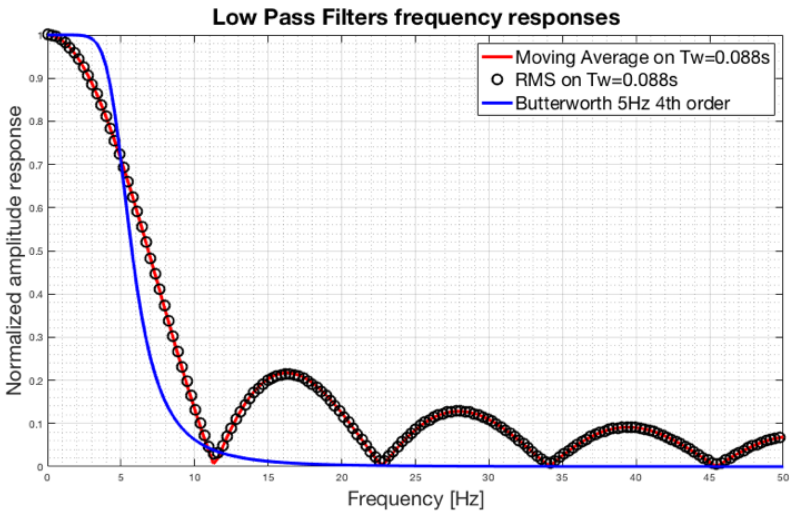

Figure 15. Frequency responses of the used low-pass filters for computing the EMG linear envelopes.

For conditioning the FSR-based sensor, it was used the op-amp trans-impedance amplifier [62], presented in section 2.1.2. By means of a static calibration, it was computed the relationship between the force exerted on the sensor (expressed in Kg) and the voltage output (V_{OUT}) of the conditioning circuit.

Beginning and end of a muscle contraction

A well-established double threshold method [89] was used to compute the beginning (onset) and the end of a muscle contraction. Assuming that the EMG signal amplitude is generally associated with a Gaussian probability distribution (normal curve), the algorithm involves to compute the mean (μ) and standard deviation (σ) of the baseline EMG activity in absence of muscle contraction (considering a time period of 250ms prior to burst). The first threshold was set to $\mu + 2.58\sigma$ ($\mu \pm 2.58\sigma$ represents the 99%

confidence interval of the EMG baseline activity). The second threshold considers a minimum time of continuous muscle activation, in which the EMG signal is above the first threshold. It was considered a time interval of 50ms [90]. This second threshold minimizes false onset detections due to fluctuations around the first threshold [89]. The detection of the end of muscle contraction is calculated similarly to the onset (using the same thresholds values). The same criteria to compute the beginning and the end of the contraction was applied to the FSR force signal (FMG).

Results

By applying the different low-pass filtering methodologies on the raw EMG signal (as described in the "Data processing" section), in Figure 16 the obtained EMG linear envelope waveforms (mV) are superimposed presented, together with the FSR force signal (Kg), in the appropriate measurement units.

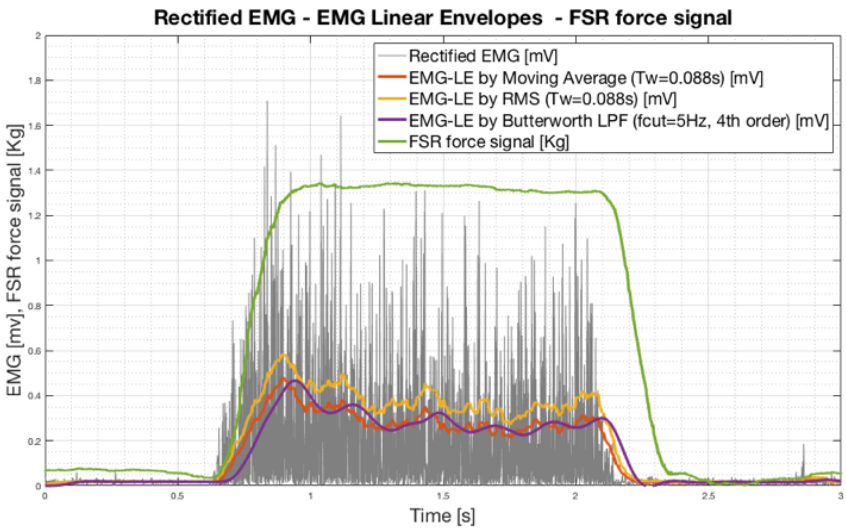

Figure 16. Superimposed plots (coded with different colors) of the rectified EMG, EMG linear envelopes and FSR force signal (FMG), related to a single wrist flexion movement.

To better visualize the time interval relating to the muscle activation (i.e. the onset), an enlargement of the beginning of the contraction is reported in Figure 17. This figure shows that the electrical muscle activation signal (rectified EMG) is rightly ahead of the mechanical muscle activation detected with the FSR-based sensor, considering the electromechanical delay. Nevertheless, it is clearly evident that the EMG linear envelopes are all delayed with respect to the FSR force signal. This is due to the lags associated with the different low-pass filtering methods. It is further emphasized that the signal from the FSR-based sensor does not need to be filtered in any way.

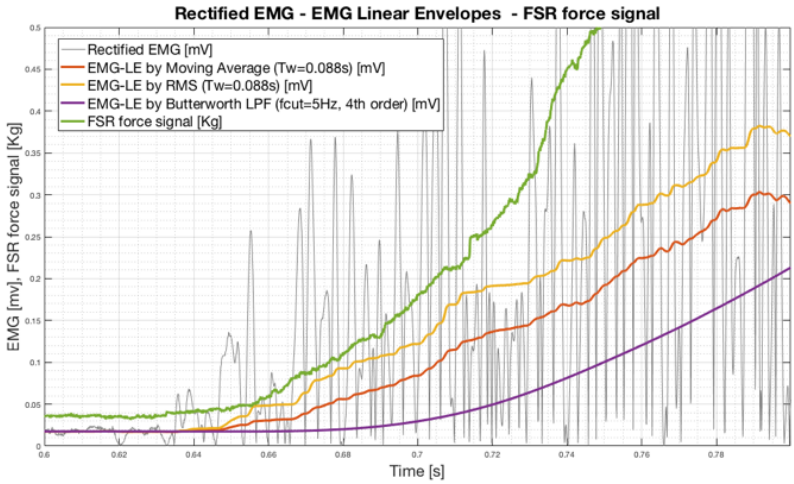

Figure 17. Enlargement of the beginning of the muscle contraction depicted in Figure 16. All signals plots (rectified EMG, EMG-LEs and FSR force signal (FMG)) are superimposed and coded with different colours.

As an example of muscle contraction onset detection by means of the double threshold technique, applied to the same muscle contraction depicted in Figure 16, the following Figure 18 shows for each different computed EMG linear envelopes and for the FSR force signal, the related thresholds and onsets.

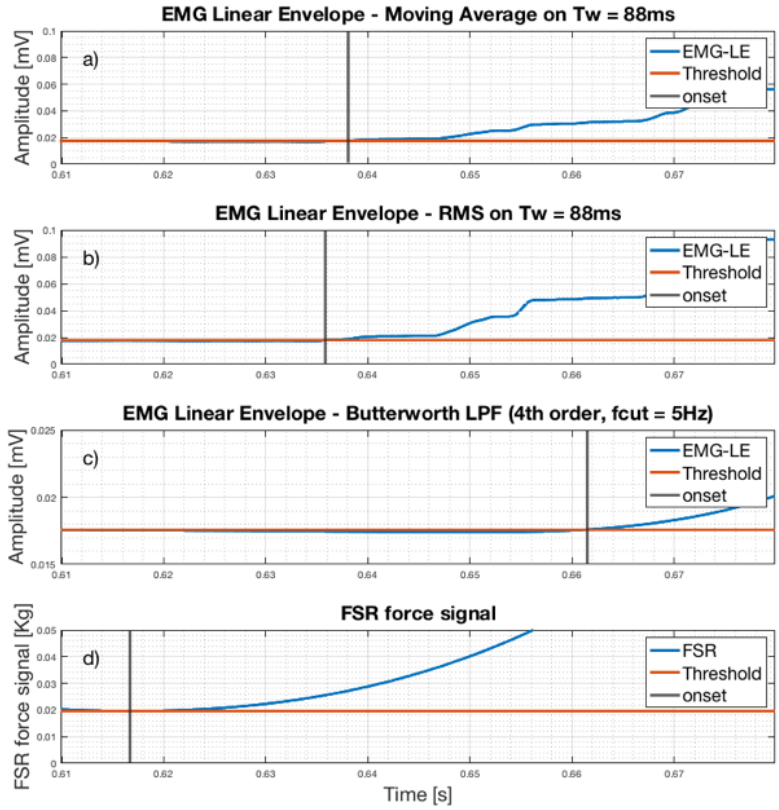

Figure 18. Detected onsets by means of double threshold method (see Materials and Methods section) for the different tested signals: a) EMG-LE computed by applying a Moving Average filter on windows of 88ms; b) EMG-LE computed by applying a moving Root Mean Square filter on windows of 88ms; c) EMG-LE computed by applying a Butterworth LPF (4^{th} order, fcut=5Hz); d) FSR force signal (FMG).

Moreover, onsets measurements were carried out on ten different muscle contractions, in order to obtain a reliable estimate of the different trigger signals (for prosthesis control) achievable with the considered methodologies. Table 1 shows the statistics of the EMG linear envelopes onsets with respect to the corresponding FSR signals onsets.

Table 1. EMG-LE onsets delays with respect to the FSR onsets

EMG-LE computation method	**Delays from FSR onsets (m ± s)**
Rectified EMG + Moving Average (computed on 88ms time windows)	30.6 ± 12.9 [ms]
RMS values computed on 88ms EMG time windows	22.1 ± 4.2 [ms]
Rectified EMG + LPF Butterworth 4th order, 5Hz cut-off frequency	59.4 ± 20.6 [ms]

The FSR onsets resulted always ahead, even if of a few tens of milliseconds, from the obtainable EMG-LE onsets. Furthermore, compared to the FSR onsets, the most performing EMG low-pass filter resulted the moving RMS, while the worst was the Butterworth filter.

Analogously, an enlargement of the end of the contraction (presented in Figure 16) is reported in Figure 19.

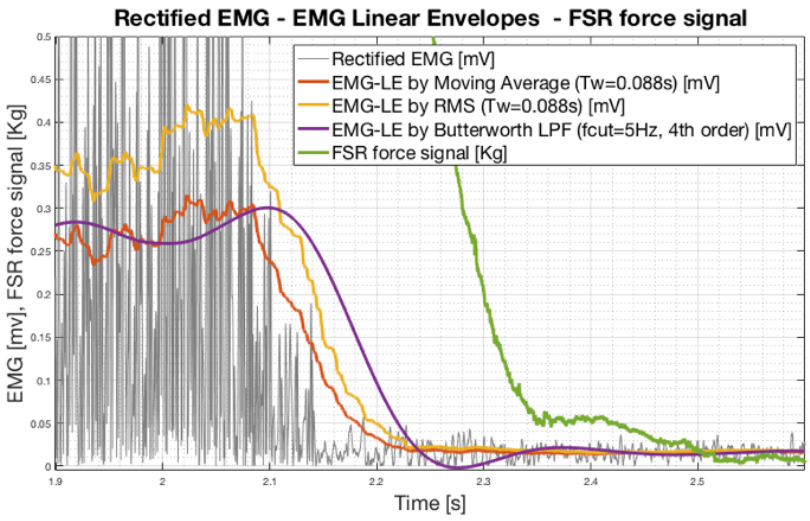

Figure 19. Enlargement of the end of the muscle contraction depicted in Figure 16. All signals plots (rectified EMG, EMG-LEs and FSR force signal) are superimposed and coded with different colours.

As already done in Figure 18, the instants computed as the muscle contraction ends, by means of the four methods, are represented in detail in Figure 20.

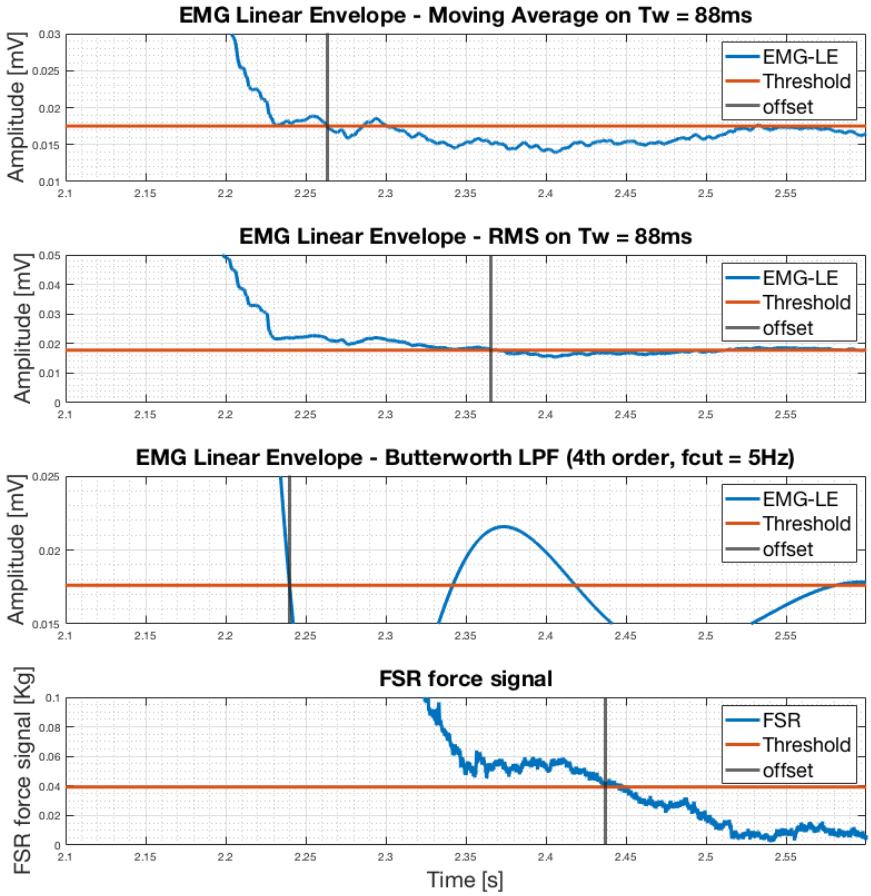

Figure 20. Detected contraction ends by means of double threshold method (see Materials and Methods section) for the different tested signals: a) EMG-LE computed by applying a Moving Average filter on windows of 88ms; b) EMG-LE computed by applying a moving Root Mean Square filter on windows of 88ms; c) EMG-LE computed by applying a Butterworth LPF (4th order, fcut=5Hz); d) FSR force signal (FMG).

Table 2 shows the statistics of the end-contraction times, computed as delays with respect to the EMG-LE, obtained by using the Butterworth low-pass filter.

Table 2. End-contractions delays with respect to the EMG-LE (Butterworth)

EMG-LE computation method	**Delays from EMG-LE (Butterworth 4th order, 5Hz cut-off freq) (μ±σ)**
Rectified EMG + Moving Average (computed on 88ms time windows)	56.1 ± 23.2 [ms]
RMS values computed on 88ms EMG time windows	114 ± 16.4 [ms]
FSR force signal (FMG)	135 ± 87.0 [ms]

To show the effect of a low-pass filter with a cut-off frequency much higher than 5 Hz to extract the EMG-LE, Figure 21 shows the EMG linear envelope signal obtained

with a Butterworth low-pass filter at 50 Hz. Obviously, with this filter the delay of the envelope obtained with respect to the raw EMG signal is significantly reduced, but the envelope signal results extremely variable and not suitable for proportionally controlling a prosthesis.

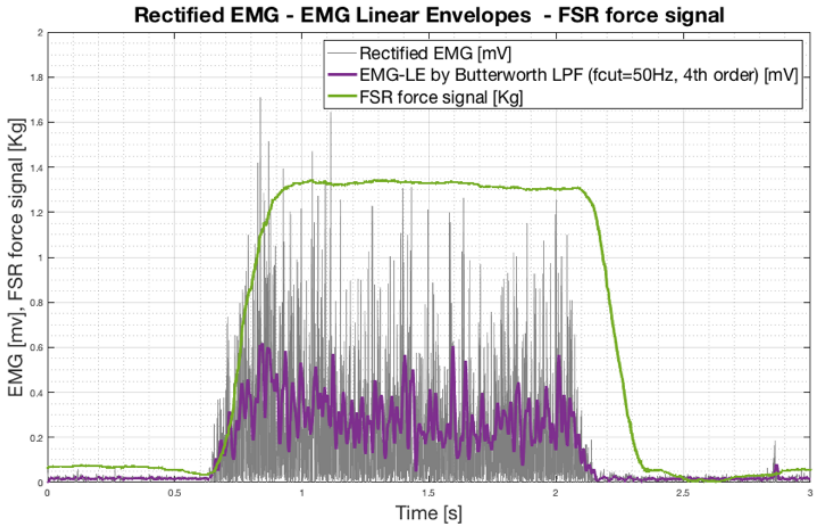

Figure 21. Superimposed plots (coded with different colors) of the rectified EMG, EMG linear envelope (Butterworth LPF, 4th order, fcut=50Hz) and FSR force signal, related to a single wrist flexion movement.

Figure 22 shows an enlargement of Figure 21 to better appreciate the signals at the beginning of the contraction. The wide variations exhibited by the envelope signal can generate various passages through the amplitude threshold and determine an uncertainty about the contraction beginning.

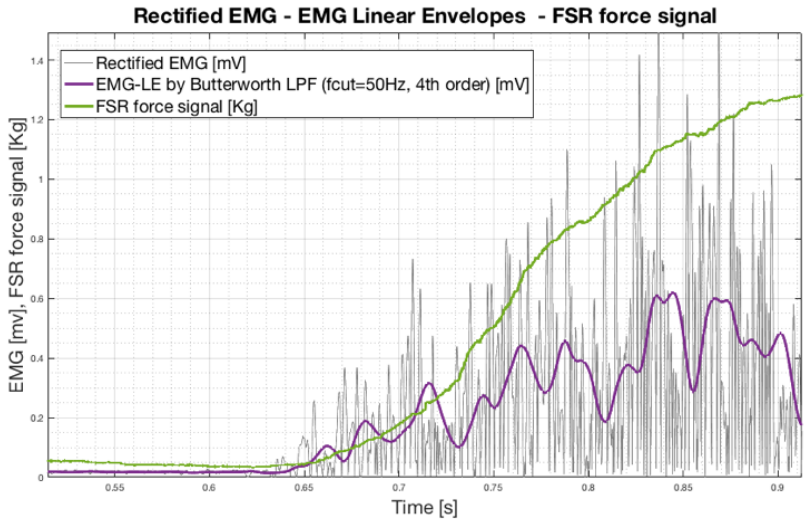

Figure 22. Enlargement of the beginning of the muscle contraction depicted in Figure 21. All signals plots (rectified EMG, EMG-LE and FSR force signal) are superimposed and coded with different colours.

Discussions and conclusions

This study proposed a comparison between electromyographic (EMG) and force-myographic (FMG) signals for providing appropriate timing control for prostheses, by monitoring residual muscle activity. The FSR force signal (FMG) is disadvantaged compared to the EMG, due to the physiological electromechanical delay (EMD) between the electrical activation of the muscle and its mechanical contraction. However, to practically use the EMG signal, it must be processed (i.e. compute its linear envelope); this processing involves a low-pass filtering operation that causes an unavoidable delay. This delay was greater than the EMD (as measured with the FSR-based sensor) with reference to the beginning of the muscle contraction. On the contrary, for the determination of the end of the muscle contraction, the FSR-based sensor always provides a delayed signal with respect to that provided by the EMG; this result is in line with what reported in the literature [91]. However, it would be interesting, in future studies, to compare the performances of force sensors as alternatives for EMG on various subjects, in order to obtain more information regarding the repeatability and the accuracy of the measurements. Likely, the muscular volumetric variation detected by means of force sensors is correlated with the specific anatomical characteristics of the subject (e.g. the ratio of lean muscle mass vs fat mass).

The results of this study provide important information about the use of force sensors as substitutes for electromyography in the proportional control of artificial limb prostheses. In particular, these are very important when very rapid mechanical actuators are embedded in prosthesis, which require similarly fast patient control.

2.2 Circumference Muscle Force Sensor

2.2.1 Sensor Design

A conductive rubber cord was also experimented to sense forearm muscle contractions. The cord is made of carbon impregnated rubber; its section is circular with a diameter of about 2mm; its resistivity is about 150 Ω/cm. The rubber results enough compliant and can be stretched more than 50% longer than its resting length. Therefore, it can be easily adapted to the specific patient forearm size. The conductive rubber cord was enclosed in a stretchable, fabric cuff so to be easily worn by the patient himself. There is no electrical contact between the sensor and the patient's body. This is an advantage over the use of electrodes to record the EMG. A constant current was injected into the rubber cord and the voltage drop at its terminals was measured (see Figure 23).

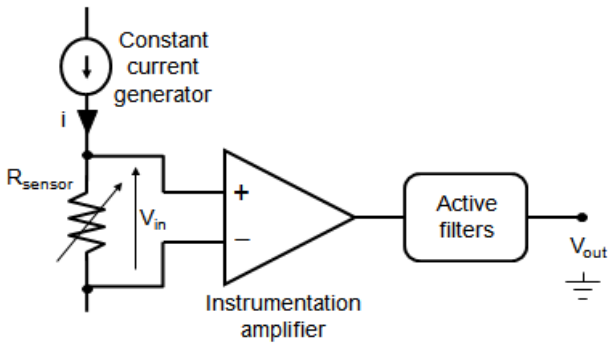

Figure 23. General scheme of the conditioning circuit for the stretchable cord sensor

2.2.2 Experimental Test

In order to test the relation between an EMG signal recorded at patient's forearm and the signal produced by the sensor wrap around the forearm, the two signals were simultaneously recorded while the patient clenched his fist.

Figure 24 shows the relative placements of the EMG electrodes and the stretchable cord sensor on patient's forearm. The EMG signal is mainly produced by the flexor carpi ulnaris muscle.

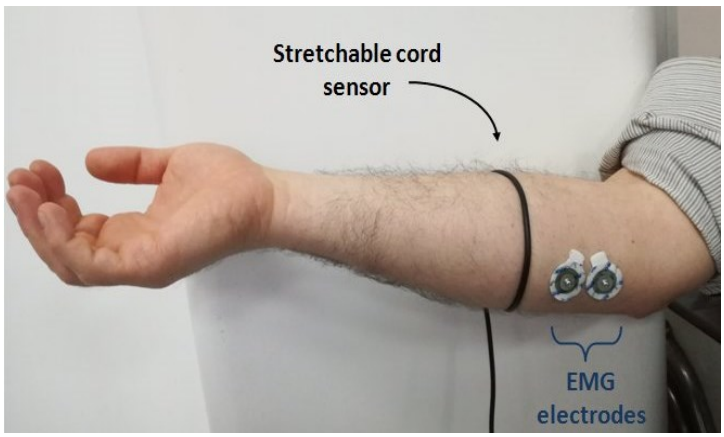

Figure 24. EMG electrodes and rubber cable sensor placed on the right forearm of a healthy volunteer.

Some of the results obtained during the various experimental tests are shown hereafter to prove the substantial equivalence of the proposed sensor with respect to the conventional EMG in controlling prosthetic hand.

Figure 25 shows the simultaneous recordings of the EMG and the output signal provided by the stretchable cord sensor, while the subject exercised five separated muscle contractions of different intensity and duration.

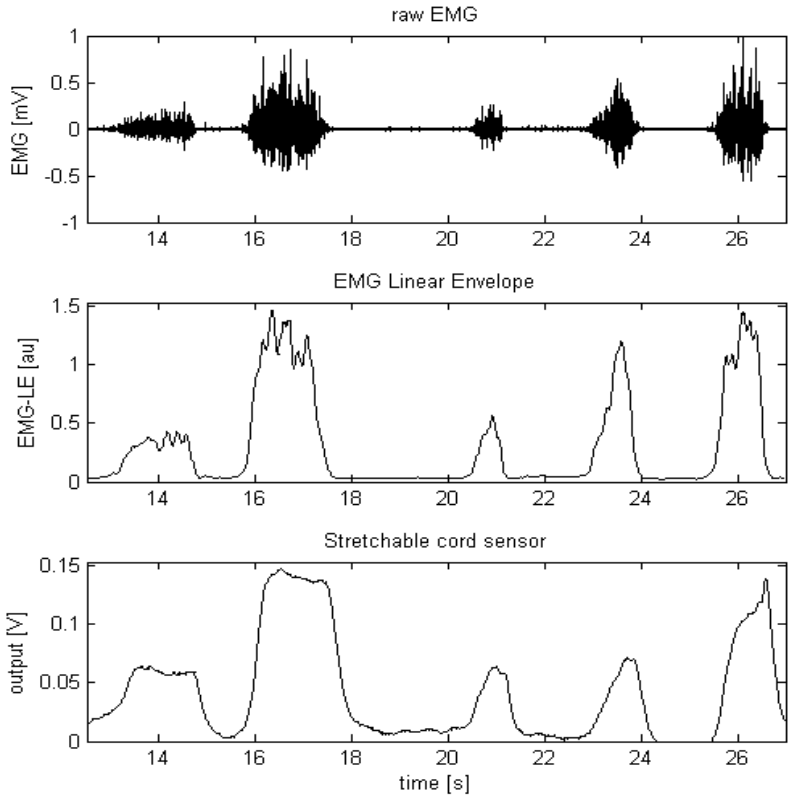

Figure 25. Simultaneous graph that displays: a raw EMG tract, with five separate muscle contractions of different intensity (upper panel); the correspondent EMG linear envelope (middle panel); the output voltage of the stretchable cord sensor (lower panel).

As can be seen from Figure 25, the EMG linear envelope (EMG-LE) and the sensor output voltage are similar but not identical. This can be explained by considering that the rubber sensor is mounted around the entire forearm circumference (see Figure 24). Hence, during the clench of the fist, the stretchable cord sensor responds to the activity of various muscles and not just to the flexor carpi ulnaris muscle, sensed by EMG. To quantitatively measure the similarity between the EMG linear envelope and the output of the stretchable cord sensor, the Pearson's correlation coefficient "r" was computed. It resulted to be 0.78 (p-value < 0.0001 (two-tailed test)).

Discussions and conclusions

This study proposes a circumference muscle force sensor, which provides a signal ready to use; it does not require any preparation of patient's skin and can be comfortably worn as an elastic cuff. The sensor is very cheap, insensitive to electromagnetic interference, withstands large mechanical stresses, wear and can be washed. Certainly, in prosthetic applications, the sensor in its present form is not suitable for controlling more than one motor. However, new topological arrangements of the stretchable cord are being considered in order to be only, or predominantly, sensitive to the contraction of a single, specific muscle. In this way, a single elastic fabric cuffs that embed multiple sensors can be made; this would allow simultaneous, independent recordings of different muscles activity.

Chapter 3

State-of-the-art of the “Federica” Hand

3.1 Mechanics and Control

3.1.1 Underactuated Mechanical System

The parts of the “Federica” hand are almost completely 3D printed in Polylactic Acid (PLA). The prosthesis has an anthropomorphic appearance and is composed of five fingers each of three phalanges. It is strongly underactuated as a single servo motor (180 degrees metal steering gear, 30 Kg/cm torque) [92] provides to synergistically move the fifteen phalanxes (15 degrees of freedom) by means of inelastic cables (artificial tendons). A custom differential mechanical system allows a balanced and constant distribution of the force between the fingers (see Figure 26).

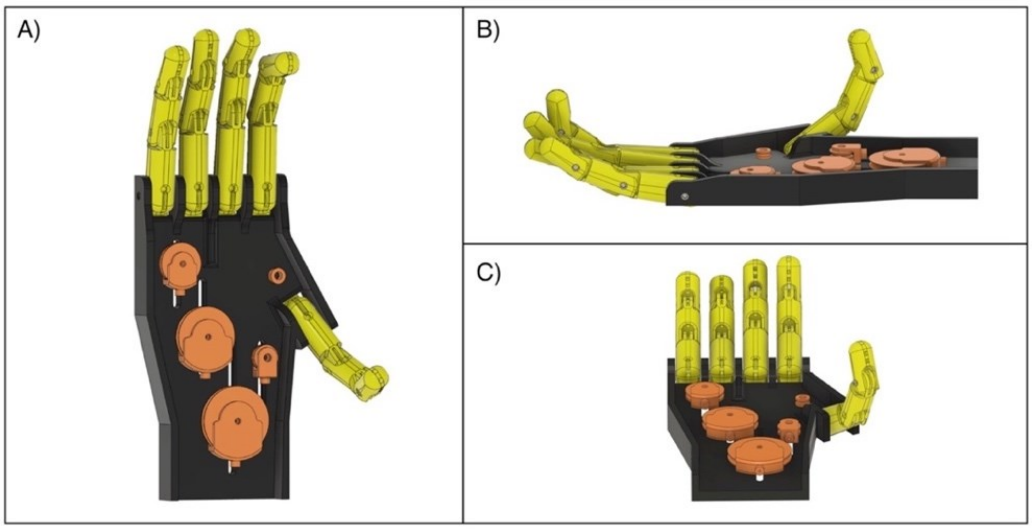

Figure 26. 3D renderings of the “Federica” prosthetic hand: a) Top view; b) Side view; c) Bottom view.

In the hand palm side (see Figure 27,A-B) it is possible to observe that the servomotor exerts a force $\vec{F}$ on the pulley A; here this force is divided into equal force components ($\vec{F}/2$) towards the pulleys B and C; pulley B further divides the force at its input into two equal force components ($\vec{F}/4$) directed towards the middle finger and pulley E respectively; pulley E in turn divides the force at its input and supplies the same force components ($\vec{F}/8$) to the ring and little fingers; finally, the pulley C distributes the force at its input into equal force components ($\vec{F}/4$) directed towards the index finger and thumb. This particular design allows to always have $\vec{F}/4$ on the thumb, index and middle fingers, and $\vec{F}/8$ on both the ring and little finger. A former functional–anatomical analysis of the human hand [93] revealed that a greater reliability in the grip is given by the thumb (for its opposability), index and middle fingers; while the ring and little fingers assist the prehension.

The mechanical system is equipped with two main tendons: one actuator (palm side) and one antagonist (back side) to perform respectively the closing (fingers flexion) and opening (fingers extension) of the hand. Both tendons are connected to the same pulley on the servomotor output shaft (see Figure 28,A), so that when one is pulled the other is released and vice-versa. In particular, in the back side (see Figure 27,C-D), the traction force used for the extension of the fingers, is distributed by using levers. A coil spring with low elastic constant (K ≈ 2.5 N/mm) is inserted on the main tendon of the back side (see Figure 27,C), in order to allow the complete flexion of the fingers, otherwise not possible by using inextensible cables (tendons).

It is interesting to emphasize that most of the hand prostheses on the market [1,2] use different coil springs positioned inside the fingers, to permit their passive extension. This entails a considerable energy absorption in having to overcome the elastic forces exerted by these coil springs during the hand closing tasks.

On the contrary, the "Federica" hand actively performs the hand opening and closing movements, in a closed chain system: the traction of the main tendon from the palm side allows the hand closure, while the traction of the main tendon from the back side permits the hand opening. The energy efficiency of the device allows the transfer of most of the motor energy to the prosthetic fingers, achieving a more powerful grip.

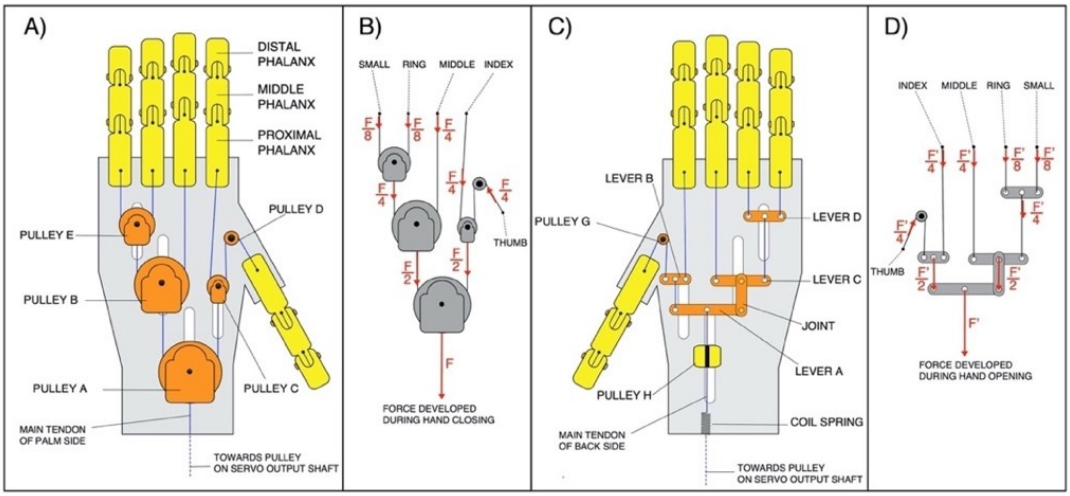

Figure 27. Illustration of the “Federica” hand design: a) Palm side mechanical system; b) Force distribution on palm side during hand closing; c) Back side mechanical system; d) Force distribution on back side during hand opening.

The current version of the “Federica” hand is showed in Figure 28. In order to preliminary test it on healthy subjects, the device was provided with a rigid handle mounted on the back of the prosthesis (see Figure 28,B-C), while two aluminium bars were used to remotely fix the servomotor. It is clearly observable that the main tendon from the palm side, after some windings around the pulley on the servomotor output shaft, is joined with the main tendon of the back side, thus making the closed chain of the mechanical system.

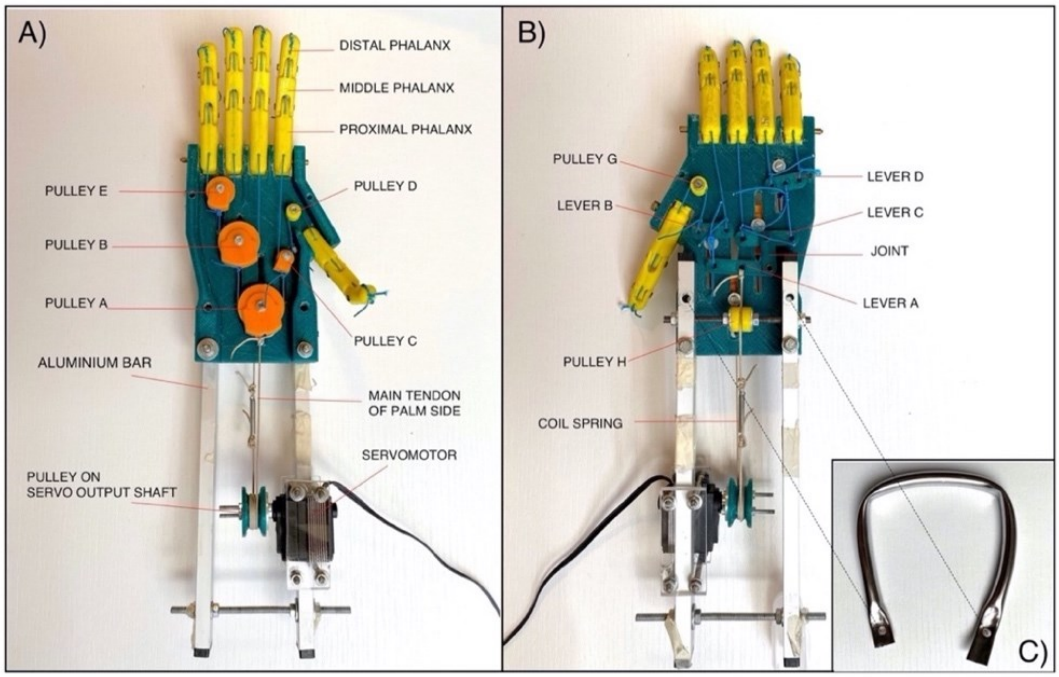

Figure 28. Current version of "Federica" hand: A) Palm view; B) Back view; C) Handle. Two aluminium bars were mounted in back side to remotely fix the servomotor.

As a further example of the closed chain of the mechanical system, Figure 29 shows the actuation mechanism of a single prosthetic finger. The clockwise rotation of the servomotor, by traction on the inelastic cable towards the hand back (Figure 29,A) performs the finger extension; on the other hand, the counter-clockwise rotation of the servomotor, by traction on the inelastic cable towards the hand palm (Figure 29,B), performs the finger flexion. The figure also highlights that these inelastic cables pass inside each phalanx (through special holes) and are knotted at the fingertip.

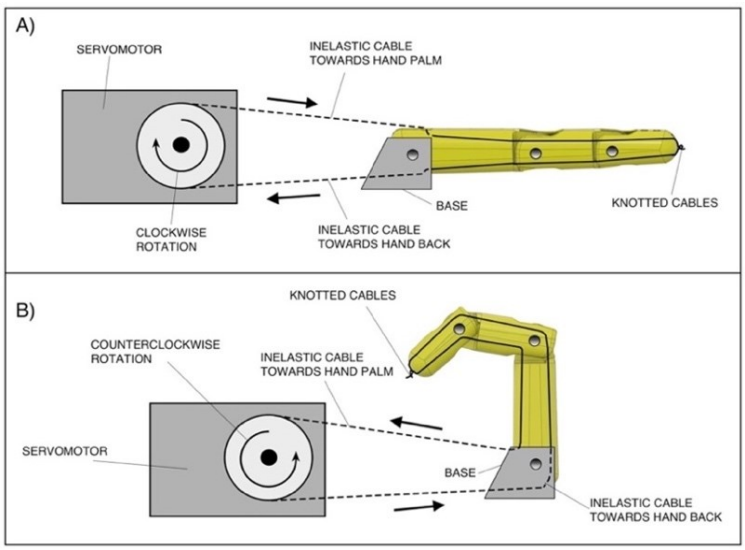

Figure 29. Finger actuation mechanism: a) finger extension by traction on the inelastic cable toward the hand back; b) finger flexion by traction on the inelastic cable toward the hand palm.

3.1.2 FMG Control and Vibrotactile Sensory Feedback

Figure 30 shows the closed loop on the prosthesis user, made by combining the force-myographic (FMG) control and the vibrotactile sensory feedback. In particular, both the "efferent pathway" (from the contraction of the target muscle to the execution of the grasp action) and the "afferent pathway" (from the sensing of the servomotor current absorption to the vibrotactile stimulation for the sensory feedback of the grip force) are presented.

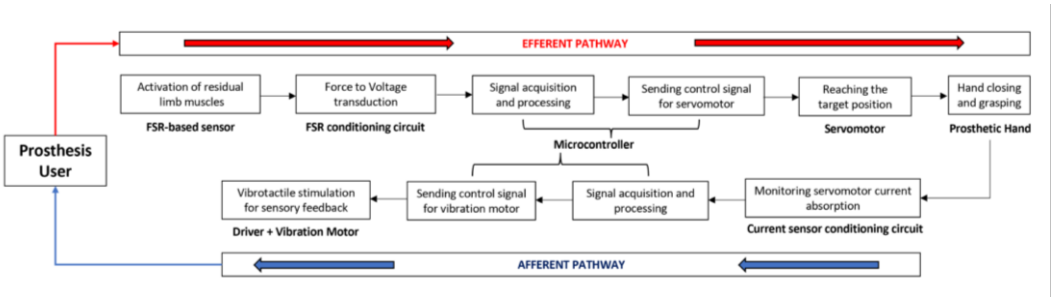

Figure 30. Flowchart describing the efferent pathway (force-myographic control system) and the afferent pathway (vibrotactile sensory feedback system).

The force-myographic (FMG) control signal for prosthesis activation, is provided by the FSR-based sensor (presented in section 2.1.1), positioned in correspondence with the forearm muscles assigned to the control. The positioning of the sensor depends on both the shape of the forearm stump and the location of the residual muscles. The FSR-based sensor is extremely thin: even with the mechanical coupler (the rigid dome in Figure 31,A), its thickness is limited and it favours its positioning both inside the socket or on other control muscles.

The FSR-based sensor is conditioned by means of a current mirror circuit [94], realized by means of a pair of pnp BJT (2N2907), gluing the two-transistor cases, in order to maintain them at approximately the same temperature. The circuit replicates the FSR current in the gain resistor R_G (see Figure 31,B) [94] providing an output voltage that is directly proportional to the force exerted on the sensor. Moreover, although the voltage across the FSR is not fixed (unlike the conditioning circuit presented in Figure 7), it was proved in [94] that by considering loads between 100g and 1500g (simulating real conditions), its percentage variation was only about 2%.

A static calibration of the FSR-based sensor was carried out to evaluate the relationship between the muscle force exerted on the sensor and the voltage output from the conditioning circuit (Figure 31,B). Different calibrated weights were progressively

applied on the active area of the sensor and the corresponding output voltages were recorded, then the static calibration relationship was obtained by means of linear regression [11,17].

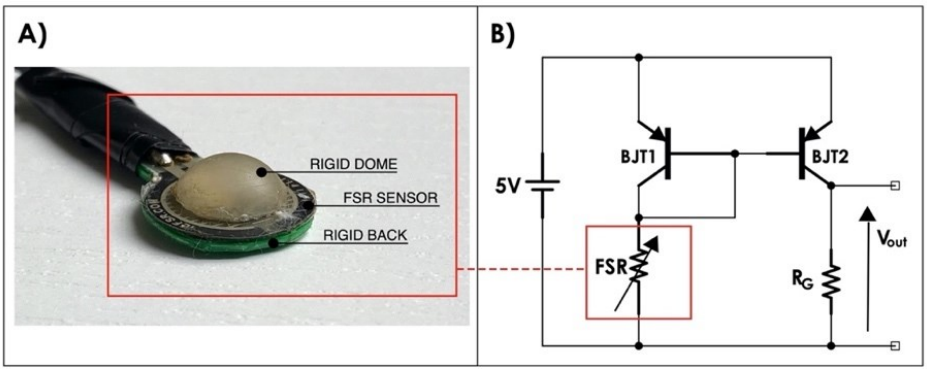

Figure 31. A picture of an FSR-based sensor equipped with a custom mechanical coupler; B) FSR conditioning circuit, based on current mirror (R_G = 910Ω).

Results of the static FSR calibration are showed in Figure 32. Experimental measurements are represented as circles, while linear regression is represented as red continuous line. Considering the weights applied to the sensor as x (N) and the output voltage from the conditioning circuit as y (V), the equation of the linear regression resulted:

$$y = 0.288\,x + 0.3727 \qquad (2)$$

with a coefficient of determination R^2 equal to 0.984.

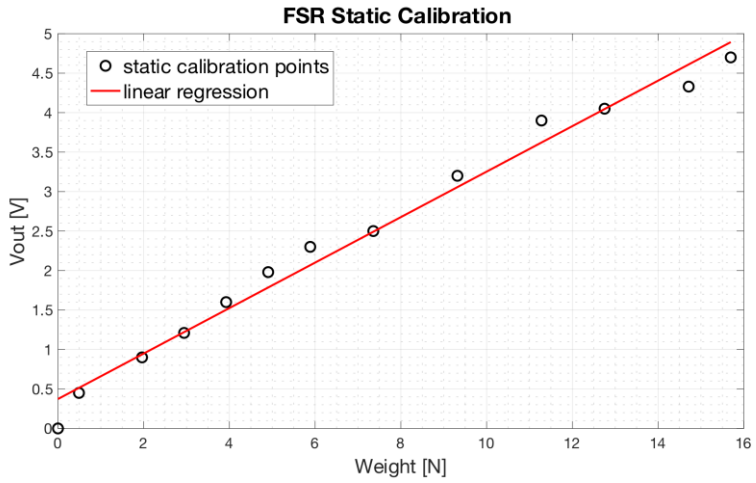

Figure 32. FSR-based sensor static calibration: scatter plot of the experimental data (o) and regression line.

The control system was implemented on an open-source Arduino platform (Arduino Nano). The whole system is powered by a 7.4V battery pack. Every time the prosthesis is

worn, a simple calibration procedure is recommended: while staying at rest (two seconds), the mean minimum force value applied on the FSR-based sensor is acquired and stored; then, while exerting the maximum voluntary contraction (two seconds), the mean maximum force is acquired and stored. The user can be guided in this calibration phase by means of the vibration motor (or by a buzzer), which signals when the patient has to contract the muscle. Figure 33 depicts the entire calibration phase as a flowchart. After calibration, the prosthesis is ready to work.

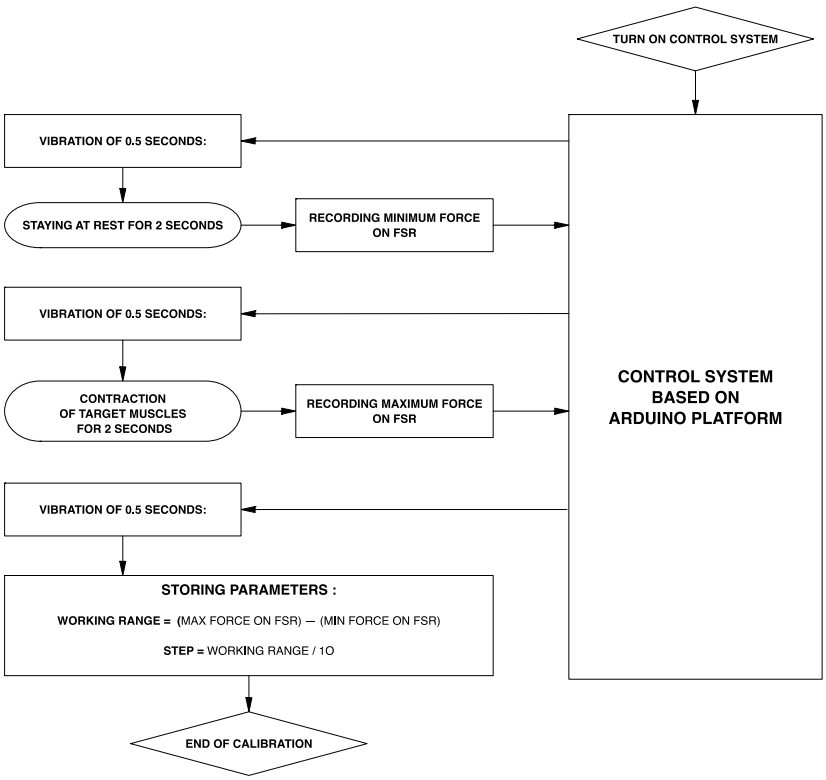

Figure 33. Flowchart describing the calibration phase of the control system.

The proportional control is achieved by associating different levels of muscle contraction (from the minimum to the maximum of the FSR output voltages) to the rotation angle of the servomotor (from 0 degrees: hand open, to 180 degrees: hand closed). Even few levels (e.g. ten) allow a progressive and smooth hand closure.

The “Federica” hand is equipped with an optional sensory system that provides information to the user about the exerted grip force. An estimate of the grip force is obtained by measuring the electric current absorbed by the servomotor, then this information is provided to the user through a vibration transducer. A previous study [47] already showed that the mechanical torque generated by servomotor, is highly correlated to its current absorption.

The motor current is continuously monitored through the ACS712 Hall effect sensor [95,97]. When the absorbed current exceeds a certain threshold for a given time (double threshold criterion [89]), a vibration is provided to the user by means of an eccentric motor placed in contact with the patient's skin (on-off sensing). In particular, an increase in current of 200 mA compared to the steady motor absorption, for a time greater than 200 ms, was empirically chosen to trigger the vibration motor. Likewise, the vibration ends when the current absorption goes under the same threshold for more than 200 ms. In a previous study [95] it was already showed that the servomotor, according to its structure and controller, absorbs current in a non-continuous way and, consequently, the absorbed current continuously shows impulsive variations. The ACS712 output signal is low-pass filtered at 5Hz by means of a hardware RC filter (R_1C_1 in Figure 34), in order to give the Arduino board a more stable signal.

The simple circuit to drive the vibration motor is showed in a section of Figure 34. A npn BJT (BJT3) is used to amplify the driver current supplied from the Arduino to the vibration motor; on the other hand, a 1KΩ resistor (R2) in series with the base of the transistor, is also used for limiting this current and avoiding motor damages. The diode (D1) acts as a surge protector for the microcontroller against voltage spikes that the motor could produce while rotating, and a 0.1uF ceramic capacitor (C3) absorbs these voltage peaks.

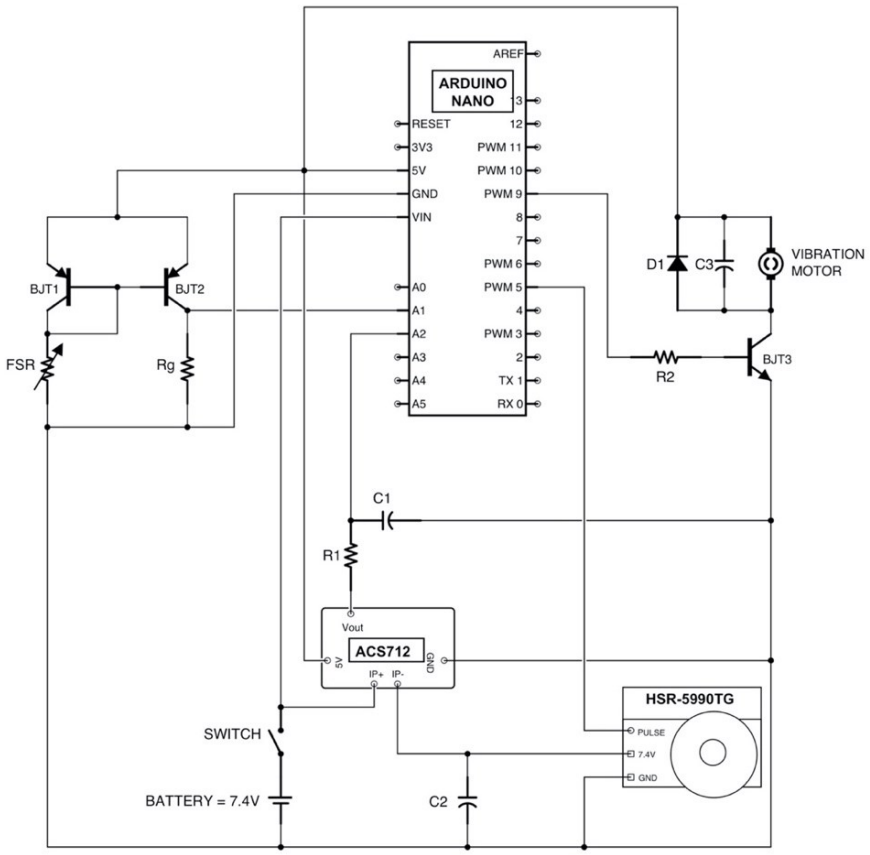

Figure 34. Circuit diagram based on Arduino platform (R_G = 910Ω; R_1 = 1.6KΩ; C_1= 20μF; C_2 = 0.47mF, D_1 (1N4001); R_2=1KΩ; C_3=0.1μF).

The flowchart of Figure 35 describes the software operations implemented on the Arduino board, for controlling the servomotor and the vibration motor.

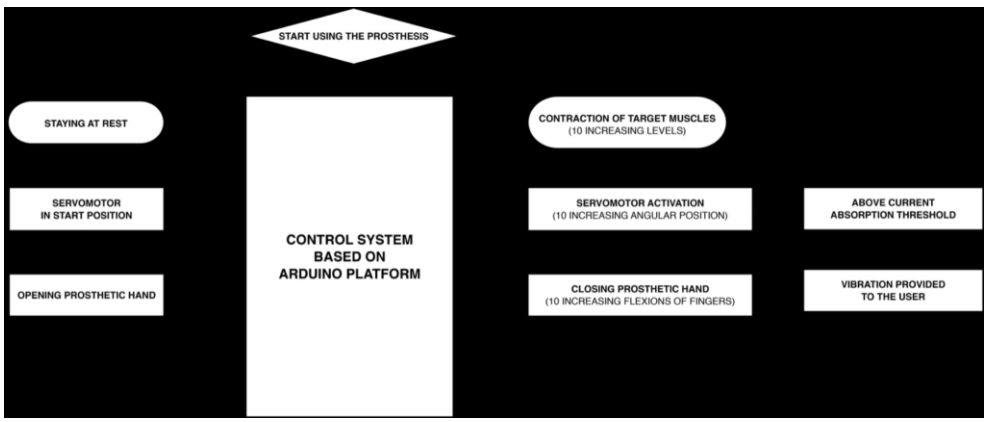

Figure 35. Flowchart describing the logic of the software implemented on the Arduino board.

Figure 36 shows simultaneous recordings of FSR sensor output (N), servomotor current absorption (mA) and vibration motor control signal (V). The FSR-based sensor (see Figure 36,A) was triggered by exerting a first impulsive and then constant force

(about 16N), in order to quickly activate the closure of the prosthetic hand and keep the grip on an object for some seconds. The current absorbed (see Figure 36,B) by the servomotor shows a first peak at the motor starting (to overcome static friction) and a second peak when the prosthetic fingers reach the object; then, the current value stabilizes at about 800 mA for the entire holding time. The panel C of Figure 36 shows the activations of the vibration motor, corresponding to three consecutive grasps.

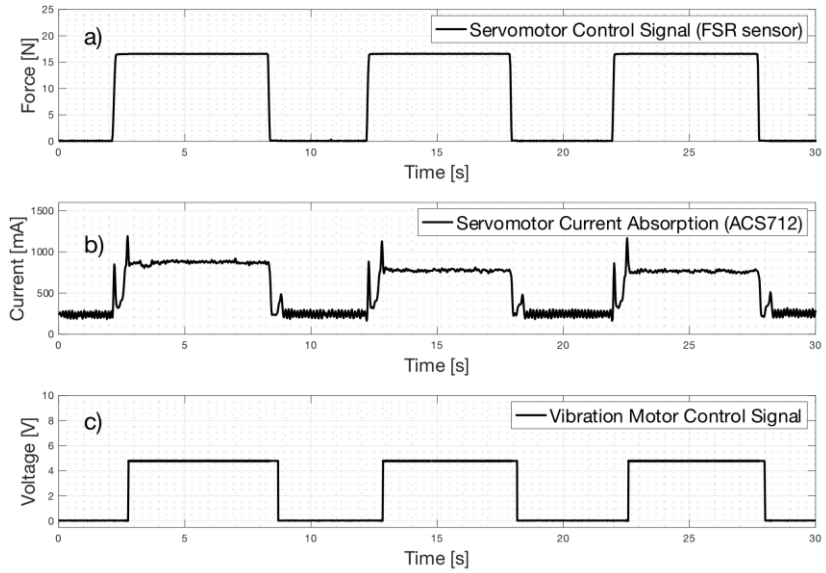

Figure 36. Simultaneous recordings of: a) Prosthesis control signal (output of the FRS-based sensor conditioning circuit); b) Current absorbed by the servomotor (output of the ACS712 conditioning circuit); c) Vibration motor control signal.

3.1.3 Design Specifications

The design specifications for the "Federica" hand are outlined in

Table 3. The size was specified to be suitable for an adult man and the mass of the device (the only prosthetic hand) was about 200 g. Different tasks of daily-life, carried out in a previous study [95], showed the capability of the device to grasp different shaped objects (raising loads up to 1 Kg) and an activation speed of about 0.5s, from the muscle sensor trigger to the complete closure of the hand. Moreover, using batteries of 7.4 V with a capacity of 3000 mAh, and considering various daily activities performed by the patient, it was estimated that the prosthesis would have an autonomy of at least an entire day [95].

Table 3. Design specifications for the "Federica" hand.

Item	**Specification**
Size	Suitable for an adult man

Mass	About 200g (the prosthesis only)
Modularity	Yes
Number of actuators	1
Degrees of freedom	15
Sensing of grip force	Vibrotactile
Max tested load	1 kg
Activation speed (from trigger to complete closure)	0.5s
Energy power	2 x 3.7V batteries (3000mAh)

The approximate costs (overestimated) for the realization of the prosthetic device (total of 100 US$) are shown in Table 4. The higher cost was due to the servomotor (Hitec HSR-5990TG), because it is equipped with metal gears and allows to generate a remarkable mechanical torque. Conversely, the costs related to the 3D printed components and the realization of the entire control system are much more affordable.

Table 4. List of components (related costs in US$) used for the realization of the "Federica" hand.

Component	**Cost (US$)**
3D printed components (PLA)	20
other mechanical components (cables, aluminium tube, screws…)	10
Servomotor (HITEC HSR-5990TG) or equivalent	40
Arduino Nano (processing unit board)	10
Battery Pack (2x3.7V rechargeable battery)	10
Piezoresistive force sensor (FSR 402 short)	5
Electronic components (BJTs, resistors, capacitors, switch)	5
Vibration Motor	(5)
Current Sensor (ACS712-5A)	(5)
----------	----------
TOTAL	100 (110)

Chapter 4

“Federica” performances

4.1 Activation Speed and Motor Energy Consumption

Introduction

This study is focused on two performance analyzes of the “Federica” hand. Firstly, it is evaluated its activation speed, from the muscle sensor (FSR-based sensor) trigger to the complete closure of the hand; then it is investigated the energy consumption, while performing some daily-life activities.

Previous studies [1,2] carried out comparisons of the most well-known hand prostheses (iLimb, Bebionic, Michelangelo, etc.) available on market, reporting specific performances. Hence, it was possible to compare these prosthetic devices in terms of activation speed with the performances of the “Federica” hand. However, no accurate data were found about energy absorption of the above-mentioned commercial prostheses (hindering comparative studies). Concise data declared by the manufacturers of prosthetic devices [98,99] were not usable for a correct comparison, because they were either too generic (for example, the current absorptions not related to certain actions performed with the prosthesis, but as average consumptions), or in relative units of measurement (for example, the speed of rotation in closing and opening of the prosthesis reported as linear speed (m/s), depending on the reference radius, and not at angular velocity (rad/s)).

Experimental setup

Full-HD video acquisitions at 100 fps of a complete rotation of the servomotor arm (Figure 37,a-b) were filmed with a Sony alpha 7III digital camera. Subsequently, the

rotation of the prosthesis pulley (Figure 37,c-d) fixed to the same servomotor, was filmed with the settings mentioned above, from the open hand position to the completely closed. This was useful to compare the different kinematic behaviours of the servomotor, when it works freely or linked to the mechanical components of the prosthesis.

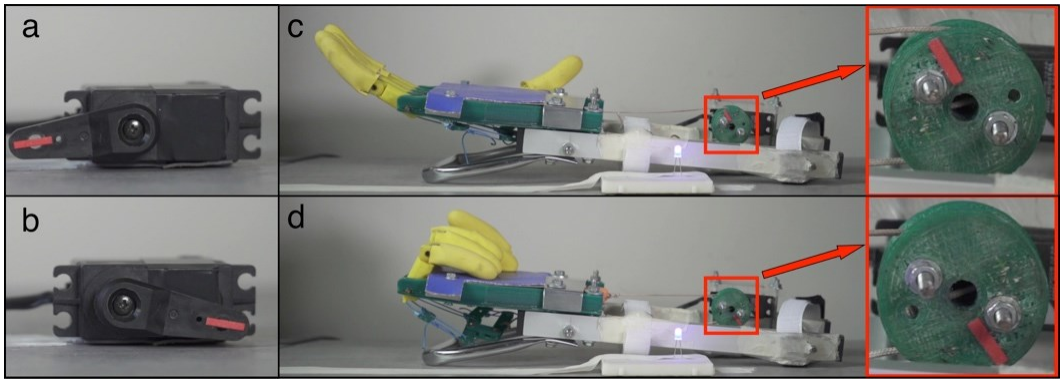

Figure 37**.** Setup for video acquisitions: a) servomotor in start position; b) servomotor in final position; c) prosthesis pulley in start position; d) prosthesis pulley in final position.

The control signals were sent to the servomotor by means of an Arduino board and a LED was used as a light indicator of the servomotor rotation. In detail, the LED turns on when the control signal is sent to the servomotor, and stays on until the servomotor rotates and reaches the final position (i.e. hand completely closed); after that, the LED turns off (see Figure 38). In this way, it was possible to precisely measure the start and end times of the servomotor rotation.

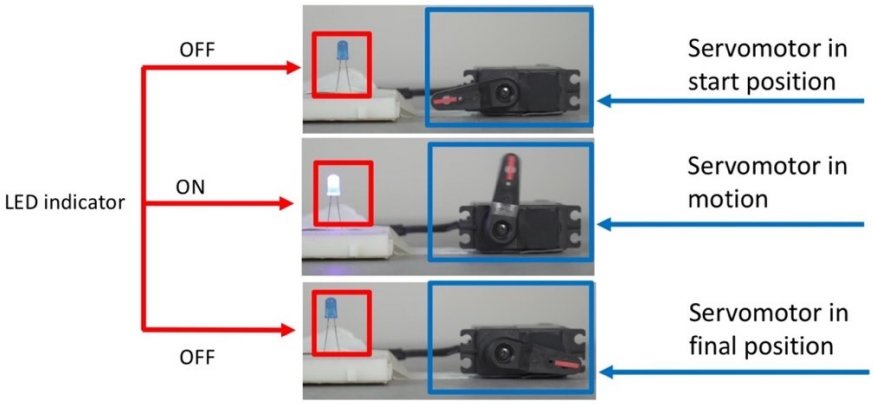

Figure 38**.** Light indication of the servomotor rotation: the LED turns on when the control signal is sent to the servomotor, and stays on until the servomotor rotates and reaches the final position.

A tool developed in MATLAB allowed the tracking of a red marker applied both on the servomotor arm and on the prosthesis pulley, frame by frame (see the flowchart depicted in Figure 39). In this way, it was possible to compute the angular displacements (rad) over time (s) in both the aforementioned cases.

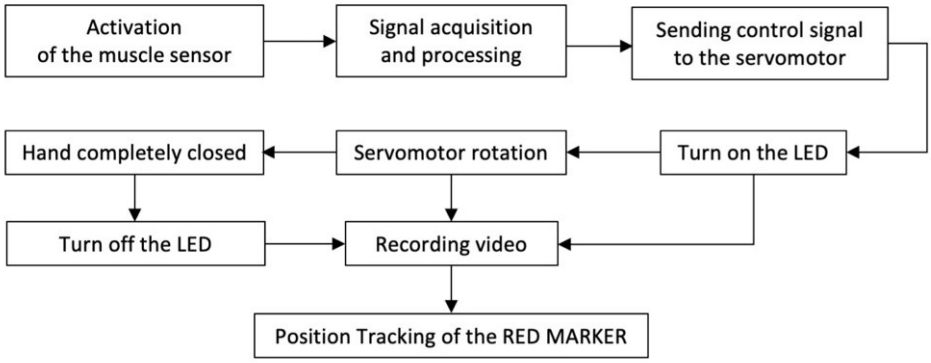

Figure 39. Flowchart describing the methodology used to obtain the tracking of the red marker applied both on the servomotor arm and on the prosthesis pulley.

The angular displacements over time were low-pass filtered by means of a Butterworth 2-rd order filter, with 10 Hz cut-off frequency. The angular velocities (rad/s) were obtained as temporal derivatives of the angular displacements, while, the angular accelerations (rad/s^2) as temporal derivatives of the angular velocities.

It was used an Hall-effect current sensor (ACS712) [97] in order to measure the absorbed current by the servomotor, under different conditions of use of the prosthesis (at rest, grasping objects, raising water bottles, etc.). In fact, the greater the load to which the prosthetic hand is subjected, i.e. the servomotor, and the greater the absorbed current by the latter. This sensor detects currents in the ± 5A range and has a sensitivity of 185 mV/A.

The servomotor, when holding a position or moving, absorbs current in a non-continuous way (according to its structure and to the servo controller). Thus, the absorbed current continuously shows sudden variations depending on the instantaneous need of energy required by the servo mechanism to hold or to change its angle. Therefore, it was necessary to filter the Hall sensor output signal with a low-pass filter (hardware RC circuit with a 5 Hz cut-off frequency) for the purpose of measuring an averaged value of the absorbed current (see Figure 40). The signal was then acquired at 10 kHz sampling frequency with 14-bit precision by means of an acquisition board (National Instruments NI USB-6009). Moreover, it was successively low-pass filtered by means of a Butterworth 3-rd order filter, with 3 Hz cut-off frequency.

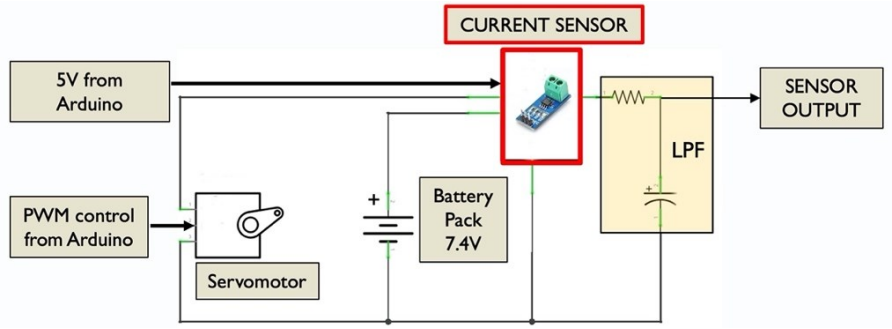

Figure 40. Circuit diagram showing the hardware configuration used for measuring the current absorption of the servomotor.

The energy consumptions related to the various conditions of use of the prosthetic device, were obtained by integrating the different current absorptions multiplied by the supply voltage for a specific time interval:

$$E = \int_{t}^{t+T} Vcc\, I(t)\, dt \quad (3)$$

(with E [J] representing the energy consumption, Vcc [V] the constant supply voltage, I(t) [A] the instantaneous current flowing in the servomotor, t [s] the time instant related to the end of the transient phase and the reaching of a stable condition, T [s] integration time: 5s).

Results

Figure 41 shows the results of the servomotor kinematic analysis, when not connected to the prosthesis (Figure 37,a-b). The total angular displacement over time of the rotor (Figure 41,a) resulted to be about 3.5 radians, and was well represented by a sigmoid regression (S-shape) such as:

$$y = \frac{a}{b + e^{-b(x+c)}} \quad (4)$$

(a = 0.0389, b = 0.01038, c = 126.4 with 95% confidence bound; x = time (ms), y = angle (rad)) with a coefficient of determination R^2 equal to 0.993.

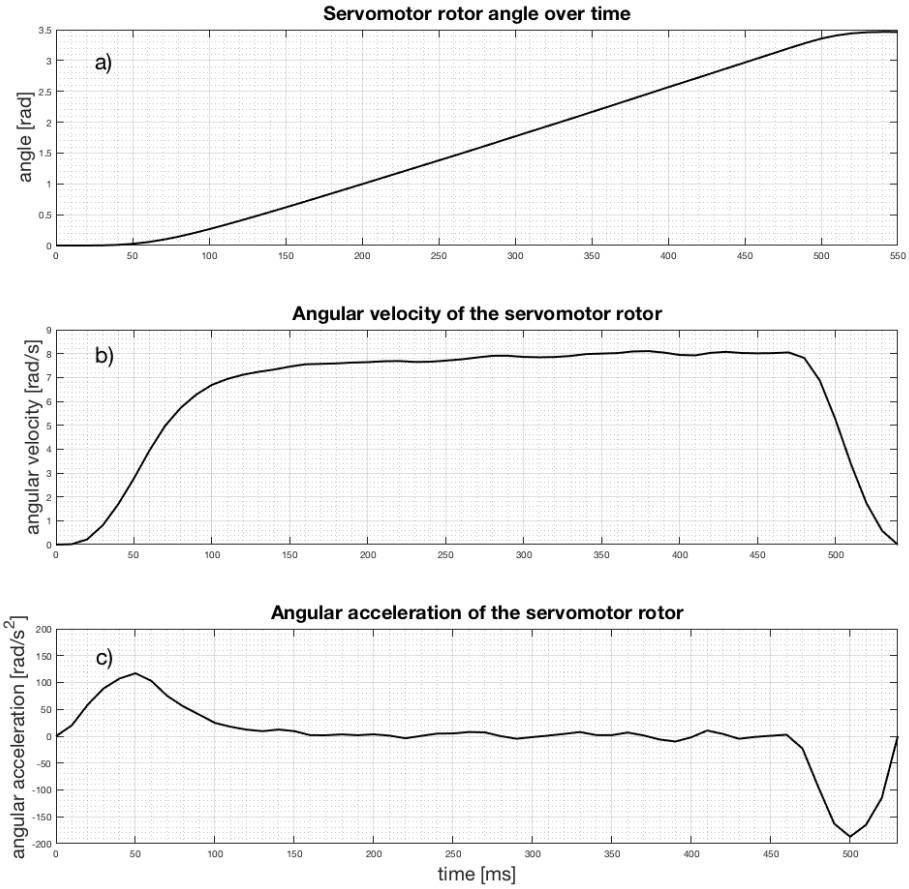

Figure 41. Kinematic analysis of the servomotor: a) angular displacement over time of the servomotor rotor; b) angular velocity of the servomotor rotor; c) angular acceleration of the servomotor rotor.

The angular velocity (Figure 41,b) was initially zero, had a rapid rise and remained almost constant at about 8 rad/s, finally, at the end of the rotation, it returned to zero.

The angular acceleration (Figure 41,c) was initially zero, had a rapid rise when the velocity incremented, remained almost null when the velocity was constant, finally, at the end of the rotation, it had a negative peak when the velocity decremented and then returned to zero.

Figure 42 shows the results of the kinematic analysis of the prosthesis pulley connected to the servomotor (Figure 37,c-d). The total angular displacement over time of the pulley (Figure 42,a) resulted to be about 3 radians, and was well represented by a sigmoid regression (S-shape) such as:

$$y = \frac{a}{b + e^{-b(x+c)}} \qquad (5)$$

(a = 0.03576, b = 0.01133, c = 94.92 with 95% confidence bound; x = time (ms), y = angle (rad)) with a coefficient of determination R^2 equal to 0.994.

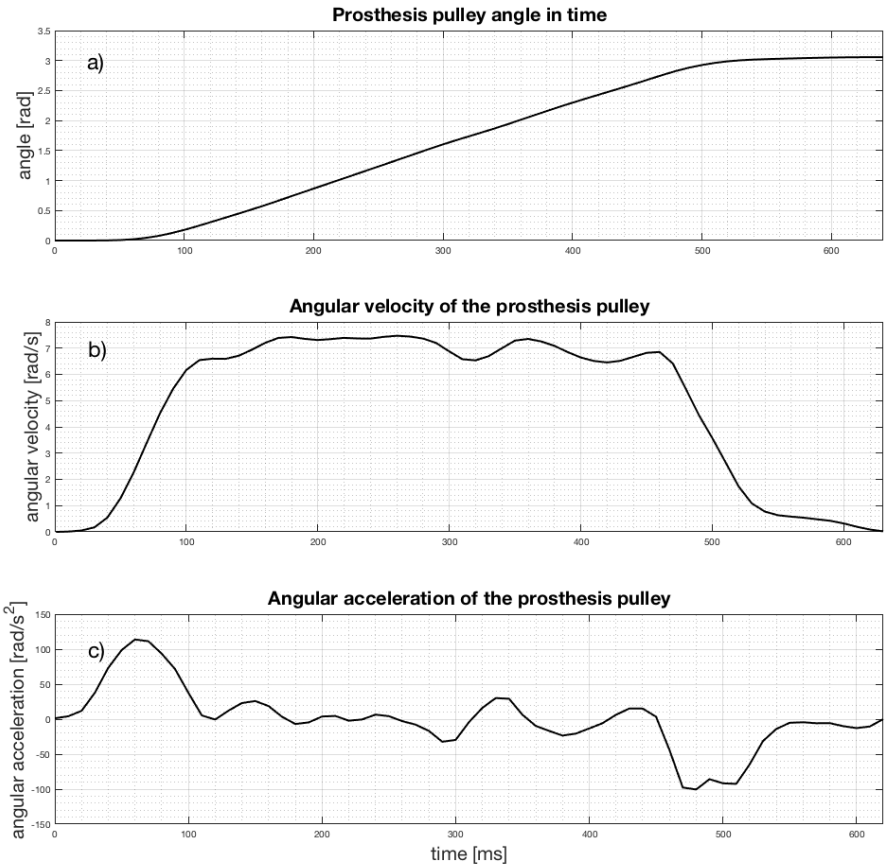

Figure 42**.** Kinematic analysis of the prosthesis pulley connected to the servomotor: a) angle position over time of the prosthesis pulley; b) angular velocity of the prosthesis pulley; c) angular acceleration of the prosthesis pulley.

The trend of the angular velocity of the prosthesis pulley (Figure 42,b) was quite similar to that of the servomotor at the previous point (Figure 41,b), with the differences of being slightly lower (about 7rad/s) and with greater variations in the central part of the rotation.

Concerning the angular acceleration (Figure 42,c), it resulted to be similar to that of the servomotor (Figure 41,c), especially with regard to the initial and final phases of the rotation, while in the central phase there are much more evident accelerations and decelerations in correspondence to the related variations of velocity.

Figure 43 shows the current absorption trends associated with the various actions, displayed in Figure 44, performed with the prosthesis.

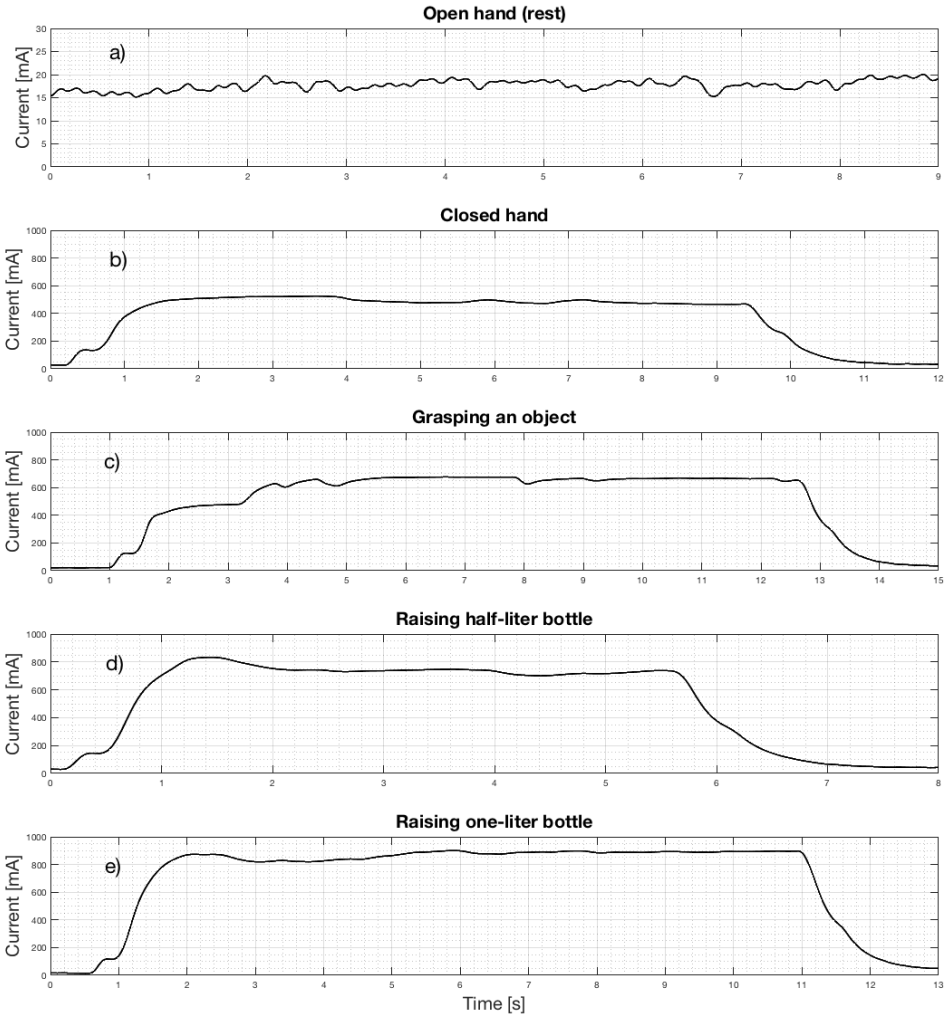

Figure 43. Trends of the current absorbed by the servomotor in the different actions performed with the prosthesis: a) open hand (rest condition); b) closed hand; c) grasping an object; d) raising half-liter bottle; e) raising one-liter bottle.

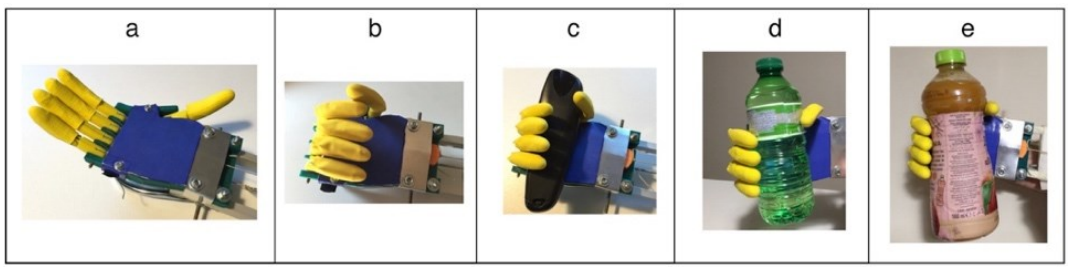

Figure 44. Images captured during the various tests performed: a) open hand (rest condition); b) closed hand; c) grasping an object; d) raising half-liter bottle; e) raising one-liter bottle.

For the time interval T (5s), corresponding to stable conditions, the average values of current absorptions and the associated energy consumptions were computed for each performed action. The results of these values are shown in Table 5.

The minimum energy absorption occurred in rest condition (less than 20mA), while in the other tested actions, the maximum absorption achieved (about 860mA) was obtained by raising a load of 1 Kg.

Using batteries of 7.4 V with a capacity of 3000 mAh, the autonomy at rest would be about a week, while constantly raising a load of 1kg of about 3.5h. Consequently, considering various daily activities performed by the patient, an autonomy for at least an entire day is predicted.

Table 5. Average values of current absorptions and energy consumptions (in 5s) for each performed action

Prosthesis activity	**Average current absorption [mA]**	**Energy consumption in 5s [J]**
Open hand (rest)	17.6	0.650
Closed hand	498	18.4
Grasping an object	665	24.6
Raising half-liter bottle	730	27.0
Raising one-liter bottle	859	31.8

Discussion and conclusions

This study showed the different kinematic behaviours of the servomotor, actuator of the "Federica" hand, when working freely or linked to the mechanical system of the prosthesis. The mechanical efficiency of the prosthesis in the transmission of movement is proved in terms of imperceptible latencies and not noticeable variations in the velocity and acceleration profiles of the motor. The high grasping speed offered by this prosthetic device (less than half a second, from the muscle sensor trigger, for a complete closure of the hand) is remarkable, even comparing these performances with the most recent and innovative prostheses on the market (0.35s for Michelangelo, 0.80s for iLimb Quantum, 1s for BiBionic V3) [1].

Regarding the energy absorption of the prosthesis motor in the various conditions of use considered, the estimated autonomy will guarantee an efficient use for at least an entire day.

4.2 Power Grip Force and Energy Efficiency of the Prosthesis Mechanical System

Introduction

Grip force is an important parameter to evaluate performances and functionalities of both human and prosthetic hands. It is a kinetic measurement that aims to provide information about the maximum force exerted by the hand, its payload capabilities and resistance to pulling or pushing forces during grasp actions [100]. For prosthetic hand, grip force is mainly function of the mechanical system that transfers the energy from the actuators to the grasped object. Generally, prostheses exhibit different grip forces depending on the size and the shape of the object, besides the force required to hold an object is highly related to the friction between the fingers and the object [101].

In recent years, different grip force measurement systems have been presented and they are principally classified into mechanical, strain gauge and force sensors devices. Split cylindrical handlebars equipped with sensors mounted between the two halves, are often used to measure the internal force transmission of a power grasp [100]. A study presented a grip-measuring device for neuro-rehabilitation, made of a split cylinder handlebar containing a single axis load cell, with the aim to improve the patient's ability to modulate the grasp force [100]. The "Yale Multigrasp Hand" prosthesis showed a power grasp of 23 N, measured by means of a load cell placed through the actuation tendon and another between fingers [102] Grip performances of the "KIT Prosthetic Hand" were evaluated by using split cylinders with diameters of 31mm and 49mm, containing a six degrees of freedom (DOFs) force/torque sensor (Mini 40, ATI Industrial Automation®), that revealed a power grasp of about 24N [68]. Grasp force tests of the "Soft Hand Prosthesis", were performed by means of a force/torque sensor (Nano 25, ATI Industrial Automation®) positioned inside a split cylindrical handlebar [76]. A multi-axis dynamometer was also presented with the purpose to evaluate the grip force of human hands in a range between 5 and 250N. The device consists of three aluminium beams covered by caps to form a cylindrical shape. Two of the beams are instrumented with strain gauges configured as full Wheatstone bridges, while the third is a static reference beam [103].

However, in addition to cylindrical handlebars mainly used for power grasp measurements, sensorized spheres were also proposed for evaluation of tripodal grip forces (grip with thumb, index and middle finger), while flat devices were usually used to measure the pressure generated by each single finger [104]. Other studies have instead

focused on mapping the local forces in specific points of both the natural and prosthetic hand (e.g. phalanges) via tiny force sensors. An example of punctual forces measurement was proposed for "The Kit Prosthetic Hand": optoforce sensors (OMD-10-SE-10N, Optoforce Ltd.) were attached to the distal phalanges of the prosthetic fingers [68]. Tekscan® company proposes the "Grip™ System", consisting of a matrix of force sensors positioned over specific location of the fingers or the hand palm, with the aim to evaluate static and dynamic forces of human hand while grasping objects [105]. Tiny Force Sensor Resistors (FSRs) [78] attached to specific points on the hand palm and phalanxes, were also used to evaluate force distribution patterns of natural and prosthetic hands [100,106,107]. In particular, a study used customized FSRs applied on 20 predefined positions of the hand, showing total grasp forces of 16.7 N for a human hand, 21.3 N for an adaptative grip prosthesis and 47.4 N and 28.5 N for the commercial non-adaptative prosthetic hands "Sensor-hand" and "System-electro-hand" by Ottobock® respectively [108].

Adaptive prosthetic hands are generally realized by means of underactuated mechanisms (less actuators than DOFs), this is achieved by reducing the number of active DOFs motors without sacrificing the ability to conform to irregular shaped objects [63,65,109]. Adaptive prostheses, by mimicking the grasp skill of the natural hand, are able to hold objects using lower forces compared to non-adaptive grippers [108]. If the gripper is able to wrap around objects and maintain a wide contact area, grip force can be kept below 10N to perform many actions of daily life. Conversely, non-adaptive grippers exert grip forces on small contact areas and need forces 3 to 6.5 times greater than those of adaptive devices [104]. Design of adaptive prostheses should resemble the adaptive grip of the natural hand, that is capable to conform to the shape of an object, thanks to its 22 degrees of freedom and to the compliance of the skin and tissue. The contact forces in human hand cover a large area and the grip is very efficient, since little energy is required for stable holding of an object [108]. Another study proposed an estimation of the grip force by measuring the current absorption of the prosthesis actuator. The current absorbed by the motor is proportional to the torque generated and, in turn, to the tendon traction force and to the gripping force, however, friction must be taken into account [76].

The current study is focused on the evaluation of the grip force provided by the "Federica" hand [47,94,95,109]. For this purpose, a split cylindrical handlebar equipped with a load cell was 3D printed, and custom piezoresistive force sensors [62,88] were applied on selected phalanxes. In addition, the energy efficiency of the prosthesis was also estimated.

Grip force measurement system

Methods for evaluating the performances of prosthetic hands, are in detail explained by the National Institute of Standards and Technology (NIST) [110]. According to the NIST guidelines, in order to measure the internal force transmission during the power grasp, it is suggested to use split cylinder handlebars, containing one or more load cells. If a handlebar capable of measuring the force along one direction only is used, it is recommended to take measurements along orthogonal directions to provide a more accurate estimate of the actual forces. The final grip force measure ($F_{total\ grip}$) is obtained by computing the L2 norm of the two orthogonal components recorded.

In this study, in order to evaluate the grip force exerted by the "Federica" hand, a single axis load cell was fixed inside a custom 3D printed handlebar, consisting of two half-cylinders. In particular, the two ends of the load cell were screwed to the two half-cylinders by placing half-centimeter spacers (see Figure 45), so that the grip force applied to the handlebar should be completely transferred to the load cell.

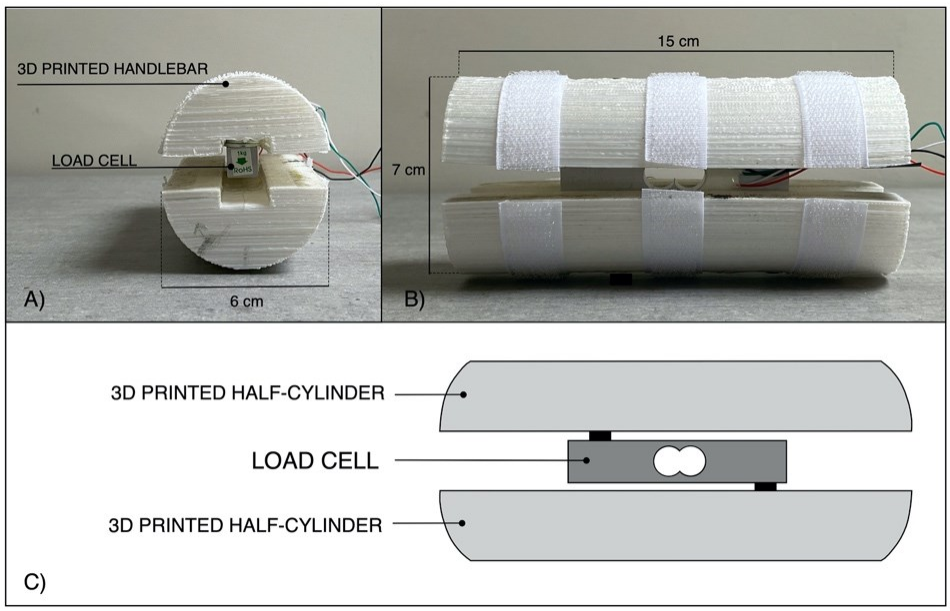

Figure 45. 3D printed handlebar for the load cell: a) transversal view; b) lateral view; c) rendering of the exploded components in lateral view.

The single axis load cell consists of an aluminum bar with four strain gauges glued on it, those are connected to form a full Wheatstone bridge circuit (minimizing the effect of temperature). All the gauges exhibit at rest a value of 1kΩ and two of them are wired in compression, while the other two in tension, so as to make the measuring circuit insensitive to temperature variations. The bridge output voltage was acquired by means of

a INA122 instrumentation amplifier [111], the gain resistor R_G was set to 500Ω (see Figure 46), providing a gain of 405 V/V.

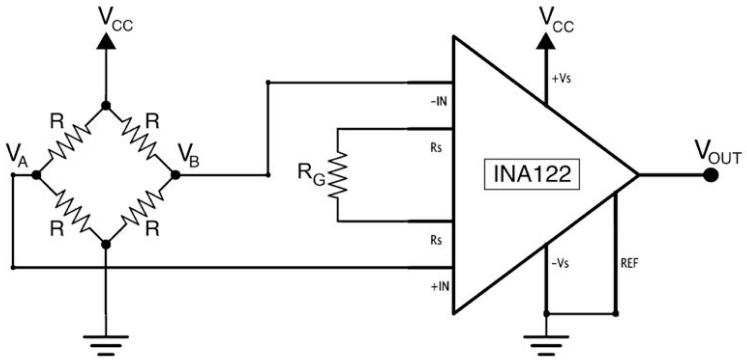

Figure 46. Load cell conditioning circuit based on instrumentation amplifier (INA122).

The equation describing the output voltage from the load cell conditioning circuit is presented below (R=1kΩ, R_G = 500Ω, Vcc = 5V, G=405):

$$\boldsymbol{V_{OUT} = G(V_A - V_B) = G\,\frac{\Delta R}{R}\,V_{CC}} \qquad (6)$$

A static calibration of the sole load cell was carried out by fixing one end of it to a table, and applying 12 calibrated weights in suspension to the other end. The output voltages corresponding to the different weights were used to perform a static calibration of the load cell.

Due to the geometry of the hand prosthesis and the diameter of the handlebar (see Figure 47,A), only the distal phalanx of the thumb and the distal and medium phalanges for the index, middle, ring and little finger, take actually contact with the handlebar. The combination of these 9 forces along the sensing direction of the load cell, provides the definitive power grip force. Tiny piezoresistive force sensors [62,88] were applied on the phalanges involved in the grasp (see Figure 47,B), in order to measure the forces exerted by each phalanx during the grasping task. Force Sensitive Resistors (FSR) by Interlink Electronics (FSR 400 model) were used; on their sensing areas, rigid domes were attached to facilitate mechanical coupling with the grasped object. As in previous studies [88,94], the FSRs were conditioned by means of current mirror circuits (see Figure 47,C). Basically, each circuit (designed to sense forces in the range 0-10 N) replicates the FSR current in the gain resistor R_G, thus providing an output voltage V_{OUT} proportional to the measured force. Static calibrations were performed to obtain the FSRs sensitivities: different calibrated weights were applied on the active area of the sensors (perpendicular to the dome) and the corresponding output voltages from the conditioning circuits were recorded, after, linear regressions provided the force - voltage relationships.

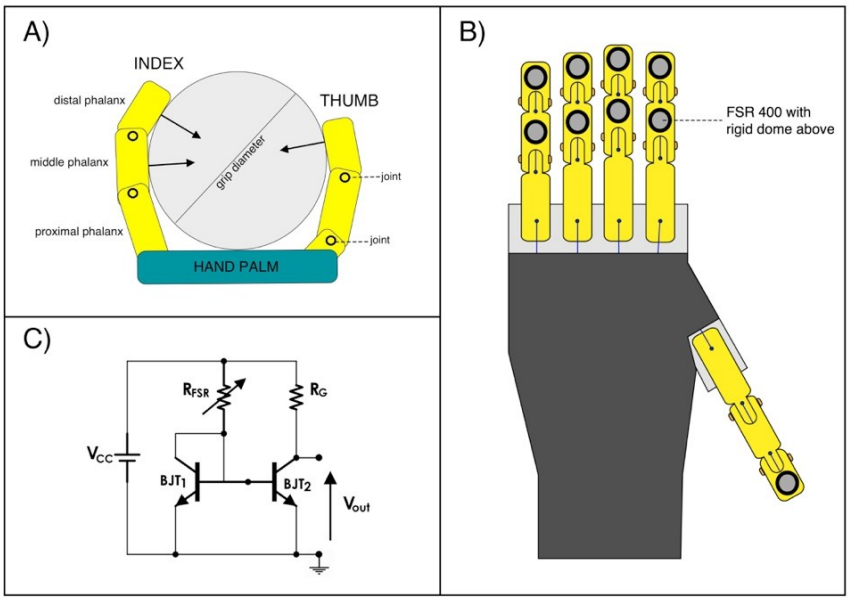

Figure 47. Force measure system for mapping the grip forces distribution between the phalanges: A) Illustration from a lateral view of the "Federica" hand while grasping the cylindrical handlebar; B) Illustration of the FSR-based sensors placements on the selected phalanges; C) Conditioning circuit (current mirror) for one of the FSR-based sensors.

Energy performance of the prosthetic mechanical system

Figure 48 shows the "Federica" hand while grasping the custom handlebar.

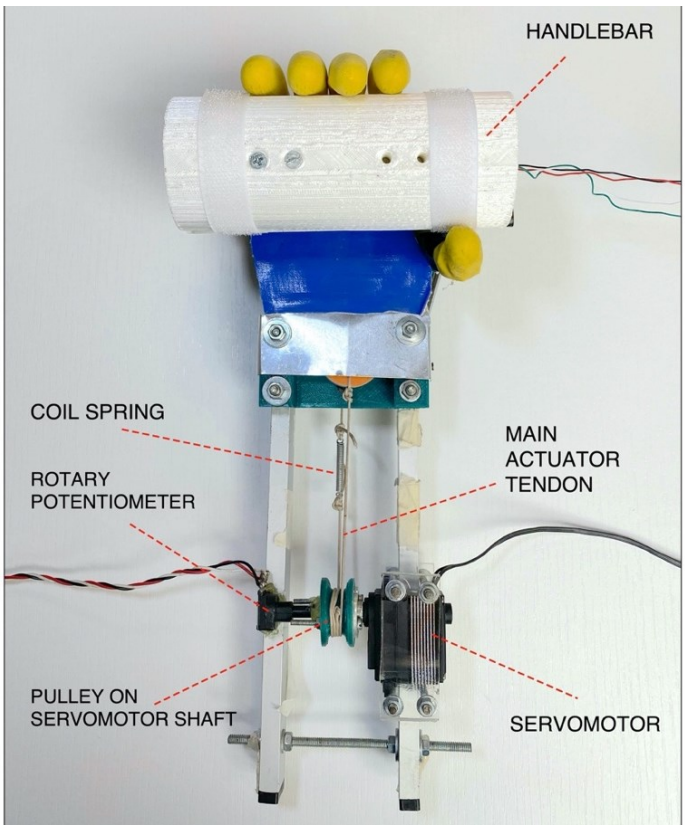

Figure 48. “Federica” hand while grasping the cylindrical handlebar during the performed grip tests.

Figure 49 shows the flow of forces generated by the servomotor on the main actuator tendon ($\vec{F}_{MAIN\ ACTUATOR\ TENDON}$) through the mechanical system. This tensile force is distributed to the phalanges ($\vec{F}_{GRIP}$) via the differential system of pulleys, partly lost by mechanical friction ($\vec{F}_{HAND\ FRICTION}$), and partly absorbed as elastic force ($\vec{F}_{ELASTIC}$) by the sole spring in the back main tendon. The grip force is the sum of the forces ($\vec{F}_{GRIP1}$) exerted on phalanges in direct contact with the grasped object. Instead, the forces ($\vec{F}_{GRIP2}$) applied on the free phalanges are not used in the prehension. The effective force ($\vec{F}_{LOAD\ CELL}$) that reaches the load cell in the handlebar, is represented by the $\vec{F}_{GRIP1}$ minus the little friction force generated inside the handlebar ($\vec{F}_{HANDLEBAR\ FRICTION}$).

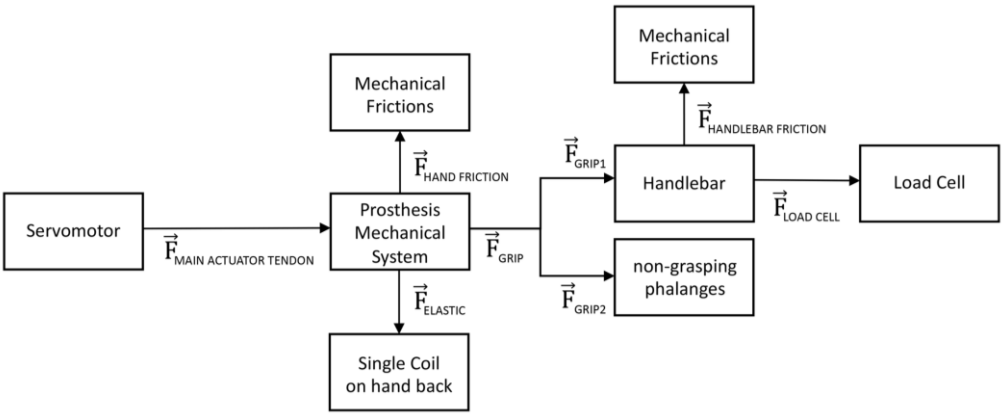

Figure 49**.** Diagram illustrating the flow of the force generated by the servomotor of the “Federica” hand.

In order to compute the energy performance of the prosthetic mechanical system, the total grip force is divided by the force applied on the main tendon.

Estimation of main tendon force from servomotor current absorption

A current measurement circuit based on the INA169 [112] was used to continuously monitor the current absorbed by the servomotor by the battery. Figure 50 shows that the motor load current I_S is drawn from the voltage generator V_{IN} through the 0.1Ω shunt resistor R_{SHUNT}. The INA169 converts the differential input voltage across R_{SHUNT} to a current output. This current is converted back to a voltage V_{OUT} with an external load resistor R_L that provides a predefined gain. The transfer function for the current measurement amplifier is:

$$\boldsymbol{V_{OUT} = I_O R_L = g_m I_S R_{SHUNT} R_L} \qquad (7)$$

Where, gm is 1000μA/V, R_{SHUNT} is 0.1Ω and R_L is 9.35kΩ, for V_{IN}=7.4V (R_L is variable and related to the input voltage V_{IN}). Therefore, measuring the circuit output voltage V_{OUT} is possible to obtain the current flowing in the load (i.e. the servomotor).

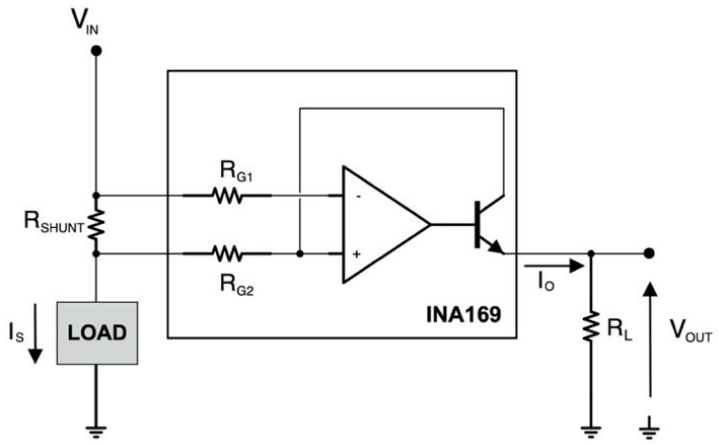

Figure 50. Current measurement circuit, based on INA169. V_{IN} = 7.4V; R_{SHUNT} = 0.1Ω; R_L = 9.35KΩ ; R_{G1} = R_{G2} = 1KΩ.

The relationship between the absorbed current and the torque generated by the servomotor [47] was estimated experimentally. The servomotor was fixed on a large table (see Figure 51,A), different calibrated weights were applied in suspension on its arm and the related absorbed current were recorded. The torque [Ncm] was computed by multiplying the weight (expressed in N) by the length of the servomotor arm (2.5cm). The linear regression of the experimental data provides the current - torque relationship. "Federica" hand operates with a 2 cm diameter pulley connected to the servomotor shaft (see Figure 51,B).

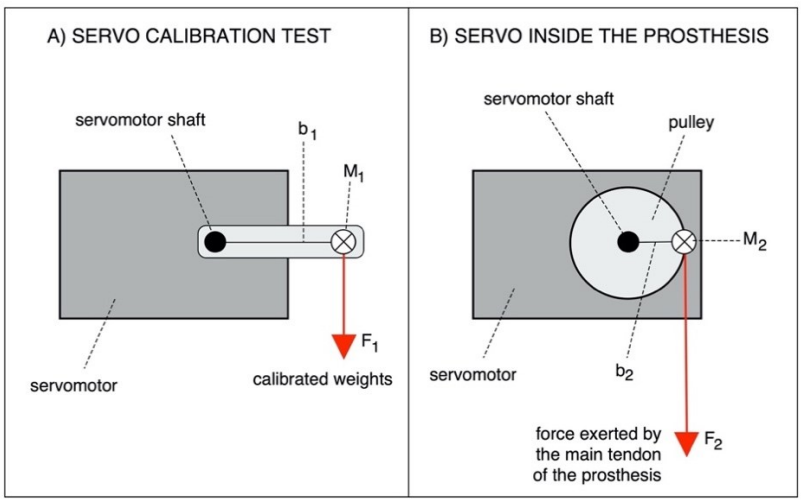

Figure 51. Servomotor configurations: A) Calibration test; B) Implementation in the prothesis.

Figure 51 shows that for the same torque, the force (F_2) exerted by the main tendon of the prosthesis is given by the following relationship:

$$M_1 = M_2 \rightarrow F_1 b_1 = F_2 b_2 \rightarrow F_2 = \frac{F_1 b_1}{b_2} \qquad (8)$$

By considering that b_1= 2.5cm and b_2= 1cm, F_2 = M_1. Thus, by correlating the current absorption to the mechanical torque generated by the servomotor, it is possible to estimate the force exerted on the main tendon of the prosthesis.

Estimation of main tendon displacement

A rotary potentiometer was fixed on the servomotor shaft (see Figure 48) to measure the angular rotation of the servomotor and, in turn, the main tendon displacement. The potentiometer was connected as a voltage divider of the 5V supply voltage. The relationship between the shaft rotation angle and the potentiometer output voltage was experimentally obtained by considering various known angular positions (18 degrees step) and measuring the corresponding displacements of the main tendon.

Estimation of work

The work needed to operate the "Federica" hand (e.g. to close and open the hand) can be computed by knowing the force exerted by the main tendon and the path length where this force is acting (i.e. tendon displacement) [4,5]. The amount of work corresponds to the area under the force-displacement curve, as explained in the following equation (W: work [Nmm]; x: tendon displacement [mm]; L: maximum tendon displacement [mm]; F: force as function of tendon displacement [N]):

$$W = \int_0^L F(x)dx \qquad (9)$$

Experimental grip tests with the load cell in different positions

Simultaneous acquisitions of the servomotor current and of the force detected by the handlebar, were carried out while the "Federica" hand gripped the handlebar. The signals were acquired at 1 kHz sampling frequency with 14-bit precision by means of an acquisition board (National Instruments NI USB-6009). The servomotor current signal was low-pass filtered with a Butterworth 3-rd order filter, 10 Hz cut-off frequency, to obtain a short-time averaged absorption, less affected by instantaneous current peaks typical of servomotors (see [95] for details). Since the handlebar senses force only along one axis, eight different angular positions (45 degrees increments - see Figure 52) of the handlebar with respect to the prosthesis palm were considered. Averages over the eight redundant measurements provide a better estimate of the gripping force components.

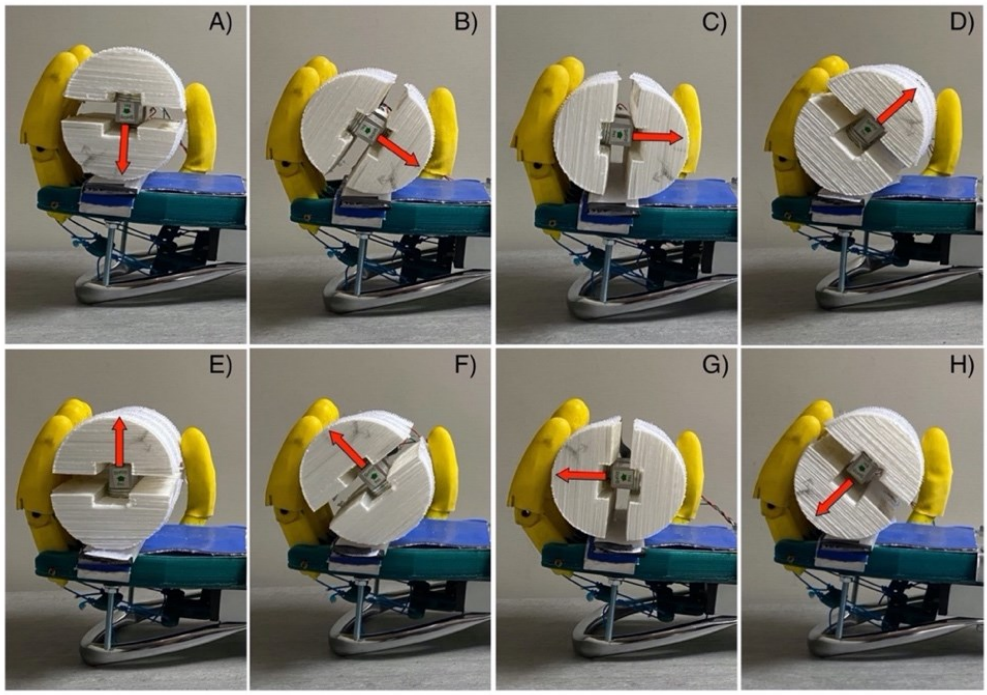

Figure 52. Experimental test of power grip force measurement, with the handlebar in eight different position with respect to the prosthesis palm: A) 0 degrees; B) 45 degrees; C) 90 degrees; D) 135 degrees; E) 180 degrees; F) 225 degrees; G) 270 degrees; H) 315 degrees. The red arrow represents the load cell sensing axis.

Load Cell static calibration

The results of the static calibration of the load cell are presented in Figure 53. The experimental measurements are represented as circles while the linear regression is represented as a continuous red line. The angular coefficient of the regression line was 0.13 [V/N], whereas the coefficient of determination R^2 of the linear regression was 0.99, proving a linear behaviour of the load cell.

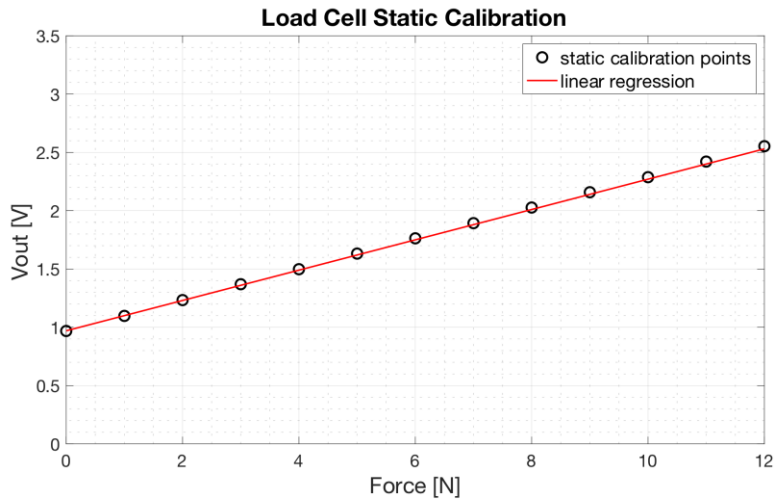

Figure 53. Load cell static calibration: scatter plot of the experimental data (o) and linear regression (continuous red line).

The equation which allows to estimate the weight applied to the load cell as a function of its voltage output (see Figure 53) is:

$$\boldsymbol{Weight\ [N] = \frac{V_{OUT} - 0.97}{0.13}} \qquad \textbf{(10)}$$

FSRs static calibrations

Results of the static calibration related to an FSR-based sensor applied on a prosthesis phalanx, are showed in Figure 54. Experimental measurements are represented as circles, while linear regression is represented as red continuous line. The regression line is expressed as:

$$\boldsymbol{y = 0.297 \times x + 4.80} \qquad \textbf{(11)}$$

with a coefficient of determination R^2 equal to 0.99. Similar results were obtained from the FSR-based sensors applied on the other phalanges.

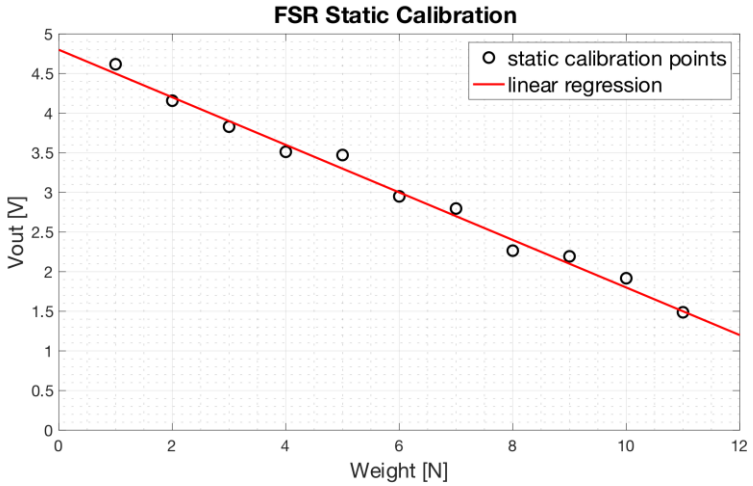

Figure 54. Static calibration of an FSR-based sensor used to measure phalanx contact force: scatter plot of the experimental data (black circles) and the regression line (red line).

Servomotor characterization

Figure 55 shows the experimental data of the current absorbed as a function of the mechanical torque provided by the servomotor. Experimental measurements are represented as black circles, while the polynomial regression is represented as a red continuous line. The relationship is clearly non-linear. However, a simple 2nd order polynomial function well fits the current-torque experimental data with a coefficient of determination R^2 equal to 0.98.

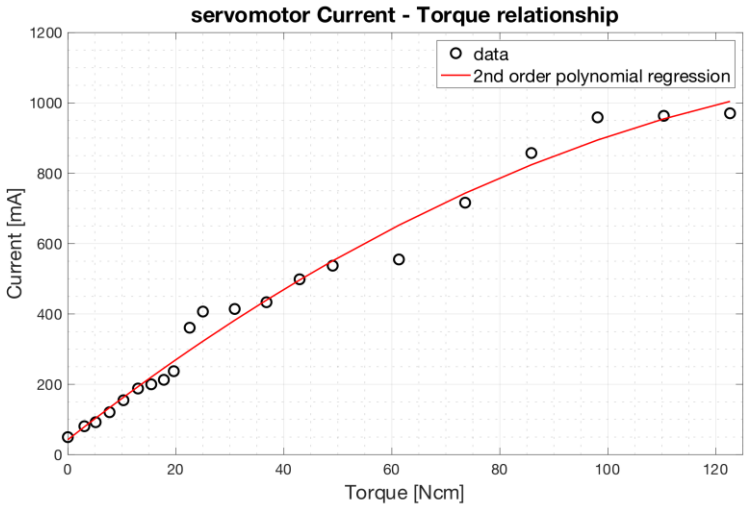

Figure 55. Relationship between the current absorbed by the servomotor (scaled in mA) and the torque generated (scaled in Ncm). The 2nd order polynomial regression function is depicted as red continuous line.

The equation of the 2nd order polynomial regression function resulted:

$$y[mA] = 42.49 + 12.05 \times x - 0.03 \times x^2 \qquad (12)$$

From this relationship, it is possible to estimate the torque exerted by the servomotor from the instantaneous measurement of the absorbed current. In turn, by considering the arm of the motor pulley of the prosthesis, the force exerted on the main tendon can be continuously estimated by the servomotor current.

Rotary potentiometer characterization

Figure 56 shows the trend of the output voltages from the rotary potentiometer fixed to the servomotor shaft as a function of the main actuator tendon displacement. The linear regression function well fits the experimental data with a coefficient of determination R^2 equal to 0.99.

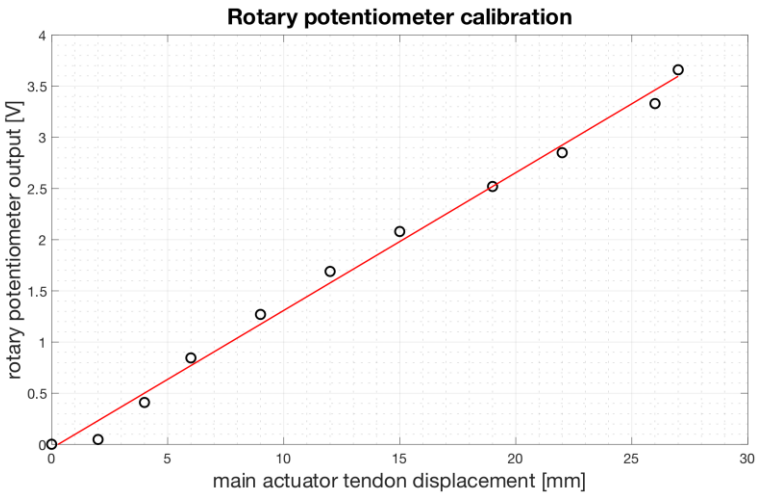

Figure 56. Relationship between the output voltages [V] from the rotary potentiometer fixed to the servomotor shaft as a function of the main actuator tendon displacement [mm]. Experimental data are plotted as black circles while the linear regression function is plotted as a red continuous line.

The linear regression function resulted:

$$\boldsymbol{y\,[V] = 0.135 \times x - 0.037} \qquad \textbf{(13)}$$

From this relationship, it is possible to estimate the main actuator tendon displacement in function of the output voltage from the potentiometer.

Results of the experimental grip tests

As an example of the grip test experimental data, Figure 57 shows simultaneous recordings of the motor current absorption (mA) and the grip force (N) exerted on the handlebar (the load cell is tilted 45 degrees as in Figure 52,B). The current (Figure 57,A) shows a first peak at the motor starting and a second peak when the prosthetic fingers make contact with the handlebar; then, its value stabilizes at about 700 mA for the entire holding time (about 11 seconds). As soon as the handlebar is reached, the grip force (Figure 57,B) shows a rapid ascent and a little overshoot, and then remains at a constant value for the entire holding time. These types of waveforms were recorded for all the eight inclinations of the load cell.

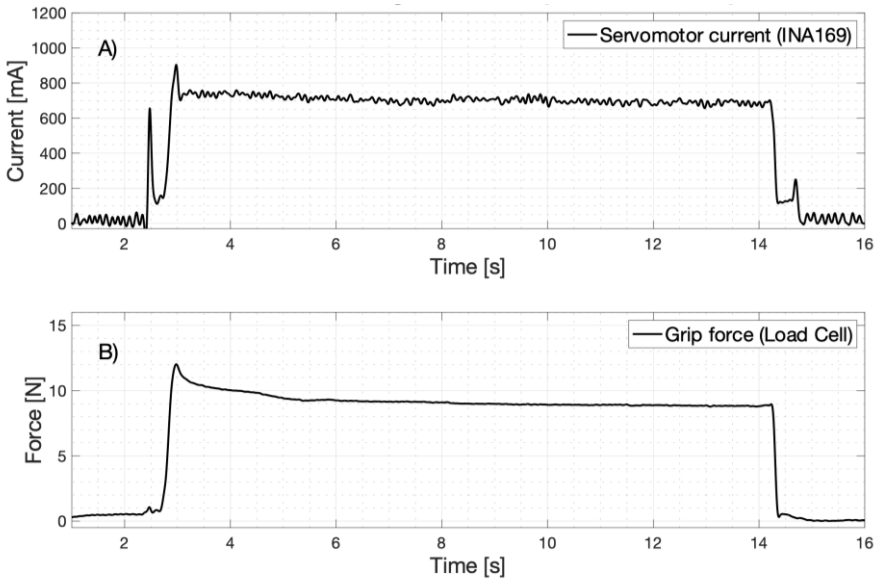

Figure 57**.** Example of experimental data recorded during the power grip test (here handlebar tilted 45 degrees): (a) Absorbed current by the servomotor; (b) Grip force on the handlebar (load cell output).

Table 6 shows the mean value of force exerted on the handlebar, the corresponding mean value of current absorbed by the servomotor and the estimated tensile force on the main tendon for all load cell tilts. The mean values were computed by considering ten repetitions of grasp tests and excluding the transients. The measured grip forces vary considerably as the load cell inclination changes: the highest values are reached at 45 degrees and 225 degrees; the lowest at 135 degrees and 315 degrees. Obviously, higher force is measured when the resultant of the phalanges forces is principally directed along the sensitivity direction of the load cell.

Table 6. Experimental data of the grip tests. For each angular position of the handlebar: the mean value of force exerted on the handlebar, the mean value of current absorbed by the servomotor and the estimated force exerted on the main tendon of prosthesis.

Load cell tilt [degrees]	**Mean force exerted on the load cell [N]**	**Mean current absorbed by the servomotor [mA]**	**Estimated tensile force exerted on the main tendon of the prosthesis [N]**
0	6.47	758	75.64
45	9.09	702	67.81
90	7.19	685	65.50
135	2.28	628	58.22
180	6.04	712	69.25
225	8.54	771	77.67
270	6.12	718	70.09
315	1.96	671	63.72

Considering the Table 6 data, the mean current absorption was about 705 mA (SD: 46 mA) and the mean estimated force exerted on main tendon was 68.49 N (SD: 6.28N).

Figure 58 graphically represents the direction and amplitude of the forces measured by the load cell for each handlebar angle.

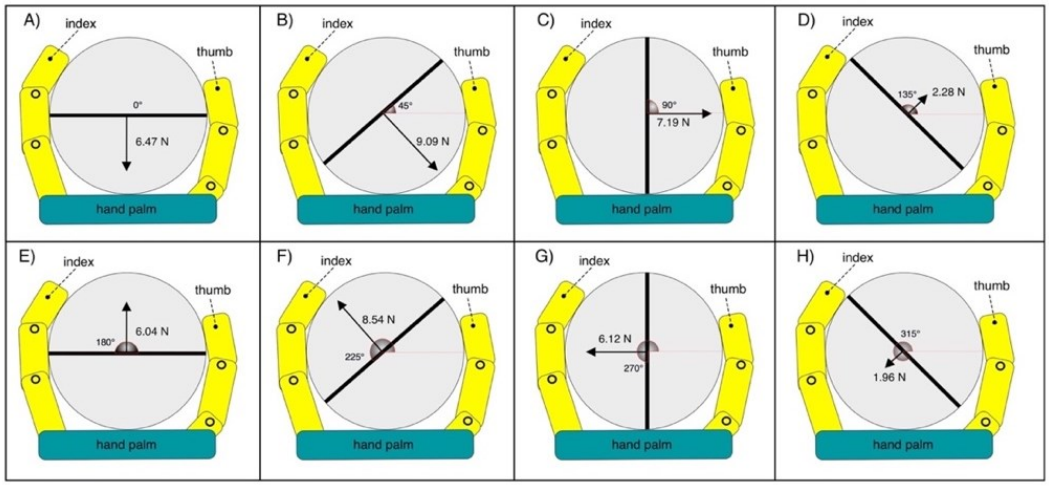

Figure 58. Measured force represented as vectors, for each tilt of the handlebar: A) 0 degrees; B) 45 degrees; C) 90 degrees; D) 135 degrees; E) 180 degrees; F) 225 degrees; G) 270 degrees; H) 315 degrees.

Figure 59 shows the polar diagram of the force measured by the load cell for the eight angles considered. The direction of maximum force is evident.

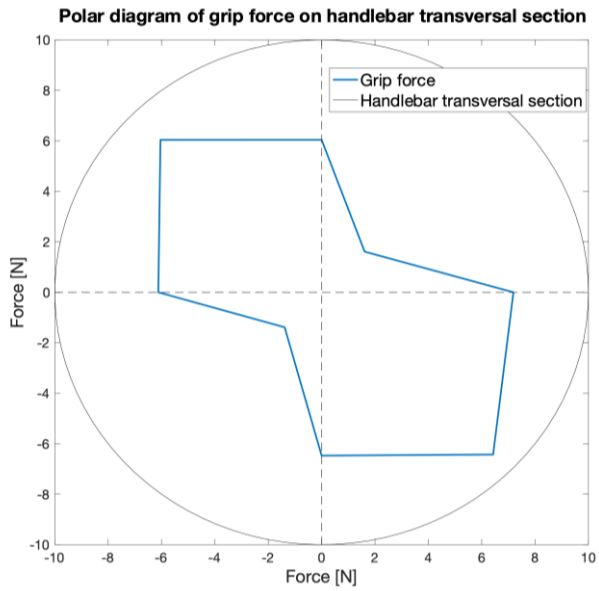

Figure 59**.** Polar diagram of the force measured by the load cell for the eight angles considered.

Table 7 shows the L2 norm values computed by considering the forces exerted on the load cell in two different positions rotated by 90 degrees. The average value for the load cell position pairs is 8.80 N (SD: 0.74 N) which corresponds to the mean power grip force.

Table 7. L2 norm values for pairs of load cell positions rotated by 90°.

Load cell positions [degrees]	L2 norm of exerted forces on handlebar [N]
0 and 90	9.67
45 and 135	9.37
90 and 180	7.54
135 and 225	8.84
180 and 270	8.60
225 and 315	8.76

Table 8 outlines the mean force values measured by means of the FSR-based sensors, on each different phalanx that take contact with the handle. On average, the middle phalanges exert the greatest forces.

Table 8. Mean forces [N] measured on selected phalanxes of the prosthetic fingers, by means of FSR-based sensors.

Finger	Phalanx	Mean force on FSR-based sensor [N]
Thumb	Distal	1.89
Index	Distal	1.95
	Medial	2.38
Middle	Distal	2.45
	Medial	4.61
Ring	Distal	0.91
	Medial	2.39
Little	Distal	1.09
	Medial	1.21

Finally, the energy performance of the whole mechanical system (see Figure 49), computed as the mean power grip force (8.80 N) divided by the mean force on the main tendon of the prosthesis (68.49 N) was about 12.85 %. It was experimentally measured that the loading of the spring present in the mechanical system, for a maximum elongation of about 3mm, absorbs 7.5N. The remaining energy is dissipated in friction by the mechanical components of the prosthesis.

Work for closing-opening the hand and hysteresis cycle

As an example, Figure 60 shows the main tendon displacement and force during a hand grip of the handlebar. Simultaneous recordings (acquired by means of NI USB-6009, with 5KHz sampling frequency and 14bit precision) of the main tendon displacement (estimated from the rotary potentiometer), and the force exerted by the same tendon (estimated from the servomotor current, low-pass filtered by a Butterworth 3-rd order filter with 10 Hz cut-off frequency) are respectively presented in panels a) and b).

The hand closing-opening cycle consists of a rest phase, a hand closing phase (that ends when the hand grasps the object), a hold-up phase and a release phase. In particular, during the hand closing phase, the tendon excursion increases until reaching the object (at about 25mm – see panel a)); likewise, when the hand starts opening, the main tendon gradually returns to its initial position. During rest, there is a pretension of about 9N on the main tendon (see panel b); when the servomotor is triggered, the recorded force presents a pulse of about 30N, associated to the force necessary to overcome the static frictions of the servomotor and other mechanical parts (note that the tendon is not moving yet). After that, the force quickly returns to the pretension values and then increases reaching its peak value (about 70N, when the handlebar is firmly grabbed). Finally, when the hand starts opening, the main tendon force rapidly returns to the pretension values.

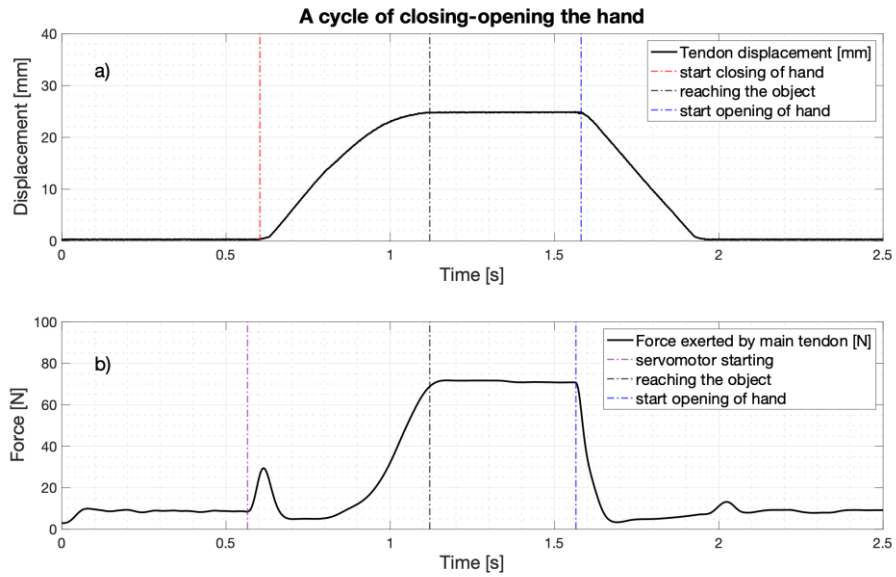

Figure 60. A cycle of closing-opening the hand: a) main tendon displacement (estimated from the rotary potentiometer) [mm]; b) force exerted by the main tendon (estimated from the current absorption of the servomotor) [N].

The relationship between the main tendon force and its displacement is presented in Figure 61. In particular, the panel a) shows a whole cycle of hand closing (blue line) and opening (red line). The blue area under the curve in panel b) represents the work required for closing the hand (work in); the red area under the curve in panel c), represents the work returned by the hand during reopening (work out); the magenta area in panel d) represents the amount of the dissipated energy (hysteresis) for an entire cycle, which is computed as the difference of the two previous works according to the following formula:

$$\boldsymbol{Hysteresis}\ [\boldsymbol{Nmm}] = \boldsymbol{Work}_{\boldsymbol{closing}}[\boldsymbol{Nmm}] - \boldsymbol{Work}_{\boldsymbol{opening}}[\boldsymbol{Nmm}] \quad (14)$$

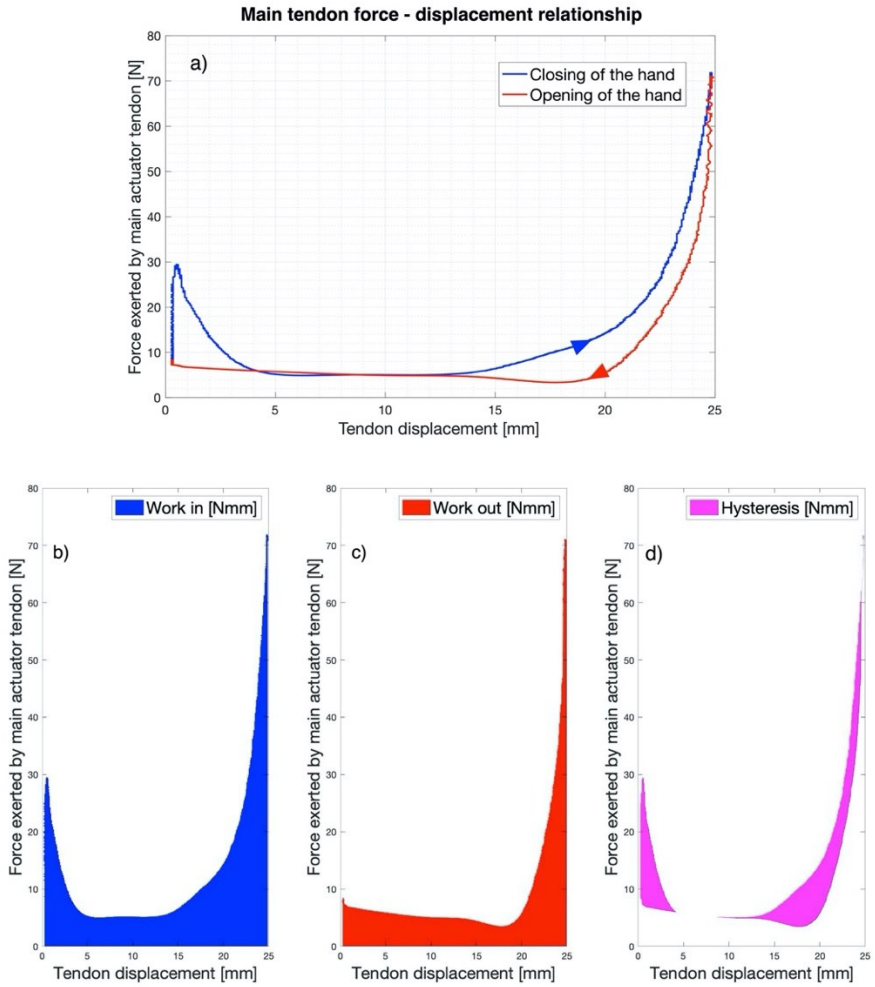

Figure 61. Main tendon force-displacement relationship a) A whole cycle of hand closing (blue line) and opening (red line), the arrows indicate the direction of travel; b) The blue area is the work required for closing the hand (work in); c) The red area is the work returned by the hand during reopening (work out); d) The magenta area is the dissipated energy per cycle.

During consecutive cycles of closing-opening of the hand, the mean values of the works were: work in = 302.17Nmm (SD: 4.42Nmm), work out = 196.84Nmm (SD: 5.91Nmm), and hysteresis = 106.80Nmm (SD: 3.31Nmm).

The energy performances of the "Federica" hand were compared with those of other prostheses available in the literature [4,5] (see Table 9). These other prostheses are body powered and uses anthropomorphic or hook mechanisms. It is evident that prostheses with hook mechanisms have, on average, greater energy efficiency (low hysteresis), with respect to the anthropomorphic prostheses. Nevertheless, "Federica" hand showed the lowest hysteresis among the anthropomorphic prostheses and most of the hook devices considered.

Table 9. Works for hand opening, closing and hysteresis [Nmm] of different hand prostheses. The acronym VO stands for voluntarily open, while VC stands for voluntarily closed.

Prosthesis	Work for hand closing [Nmm] (mean ± SD)	Work for hand opening [Nmm] (mean ± SD)	Hysteresis [Nmm] (mean ± SD)
Federica Hand	302.17 ± 4.42	196.84 ± 5.91	106.80 ± 3.31
Hosmer APRL VC Hand 52541	1058 ± 4	-	298 ± 8
Hosmer APRL VC Hook 52601	720 ± 6	-	138 ± 3
Hosmer Soft VC hand 61794	2292 ± 12	-	1409±37
TSR VC Hook -Grip 2SS	284 ± 3	-	52 ± 1
Otto Bock VC 8K24, frame	1624 ± 8	-	389 ± 19
Hosmer Sierra VO Hand (ungloved)	-	1152 ± 8	637±6
RSL Steeper VO Hand (ungloved)	-	1758 ± 27	855±6
Otto Bock VO Hand (ungloved)	-	2545 ± 11	917±5
Hosmer Becker VO (ungloved)	-	2748 ± 17	1710 ± 9
Hosmer Model VO 5XA Hook (1 band)	-	1128 ± 14	290±3
Otto Bock VO 10A60 Hook	-	1002 ± 3	482±5
Hosmer Sierra 2 Load VO Hook	-	1243 ± 11	379±1
RSL Steeper Carbon VO	-	1619 ± 2	487±4

Discussion and conclusions

This study presents the experimental tests carried out on the “Federica” hand, for evaluating its power grip force and energy efficiency. A custom split cylindrical handlebar embedding a single axis load cell was used; it was positioned in various angles during grasp. The mean grip force was 8.80 N (SD: 0.74 N) (average and SD of the L2 norms, according to the NIST guidelines [110]). However, by using more complex measurement systems, such as multi-axis load cells, that simultaneously sense force contributions from multiple directions, higher values could be obtained.

The current absorption of the single servomotor that actuates all the five prosthetic fingers, was chosen to estimate the force exerted by the main tendon of the prosthesis, during the grasping tasks. This measure of force combined with that of tendon displacement, made it possible to estimate the energy performance of the “Federica” hand, which turned out to be remarkable. It is well known that an efficient mechanism has a low hysteresis [4], that is low dissipated energy. The “Federica” hand showed a mean hysteresis of 106.80 Nmm, which resulted much lower than most of the considered prostheses [4,5]. Moreover, the energy peak at the servomotor starting (see Fig.16,B), when the tendon is still not pulled, involves an overestimation of the hysteresis. The limited energy efficiency of the “Federica” hand of about 12.85%, is most likely due to the frictions generated by its mechanical components. This apparently low value is due to

the anthropomorphic structure of the prosthesis; higher values can be obtained with hooked prostheses [4,5]. However, thanks to the adaptive grip of the prosthesis that is able to wrap around any shaped object [47,77,94,95], a power grip force below 10N, together with a hand closing time of about half a second [95], are enough to support the user in many actions of daily life [104].

The obtained results confirmed that the “Federica” hand with a single servomotor and the differential force distribution mechanism between the fingers, is able to offer high performances that guarantee a secure grip, independent of the shape of the object, and a remarkable grasping speed. Limitations of this study include: the use of a single diameter handlebar equipped with a single axis load cell and the indirect measurement of the tensile force on the main tendon.

4.3 Tests on Healthy and Amputee Subjects

Test on healthy subjects by using the circumference muscle force sensor

Various tests were carried out on voluntary healthy subjects, to verify the capability of the circumference muscle force sensor (presented in section 2.2), as alternative to the EMG, to control the "Federica" hand. The sensor was placed around the proximal forearm (at about three quarters of the distance between the wrist and the elbow). The control was based on proportional logic: the degree of hand closure is related to the intensity of the muscle contraction (i.e. the stretching of the conductive rubber cord sensor).

The subjects were asked to perform slow actions as to grab objects (both rigid and deformable) of different shapes, to take a bottle, to take a glass to drink and even some fast actions as to catch a flying ball, thrown by another person (see Figure 62). The subjects became familiar with the prosthesis very soon and were able to successfully perform the required actions.

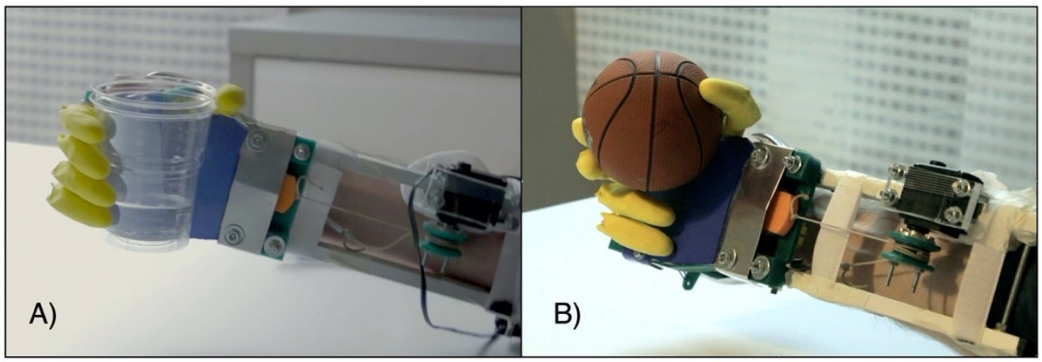

Figure 62. The picture shows some tests carried out with the "Federica" prosthetic hand, while: A) Holding a glass of water; B) Catching a ball on the fly.

Test on healthy subjects by using the single-point force sensor

Various tests were principally carried out on healthy volunteer subjects, to assess the ability of the FSR-based sensor (presented in section 2.1) to implement the control of the "Federica" hand. The control was proportional—the more intense the muscular contraction, the more the hand clenches (performing a synergic grasp movement). The test consisted of replacing the EMG-LE control signal with the raw signal generated by the FSR-based sensor, applied on the flexor carpi ulnaris of each subject, by means of an armband. The subjects wore the prosthetic hand and performed some predefined tasks: grabbing both non-deformable objects (such as fruits, glasses, etc.) and deformable objects (such as sponges, rubber balls, etc.), pouring some water from a plastic bottle into

a glass to drink, etc. These tests confirmed the high speed of interaction between the user and the prosthesis and the self-adapting capacity of the device to grab many complex shaped objects, ensuring a secure grip on them.

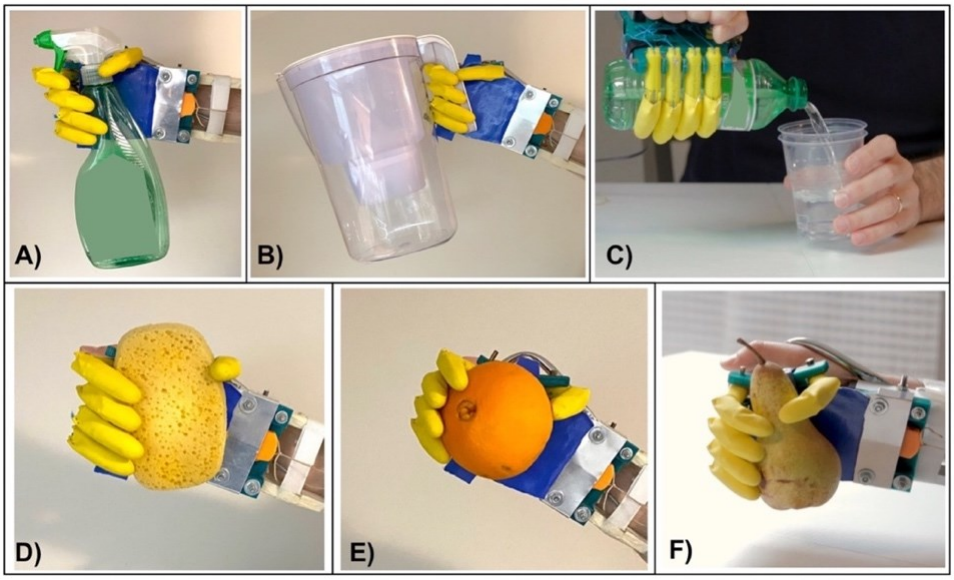

Figure 63. “Federica” hand tested on healthy subjects, while holding: A) a spray cleaner; B) a water tank; C) a bottle; D) a sponge; E) an orange; F) a pear.

Preliminary test on an amputee patient by using the single-point force sensor

A very preliminary test of the “Federica” hand was carried out by a patient with transcarpal amputation, executed in 2007 following a traumatic event (the wrist disarticulation is still present). The patient was unable to get used to EMG-controlled prostheses due to difficulties encountered in training and has folded back into use of a simple aesthetic hand prosthesis, as showed in Figure 64. The connection of the prosthesis to the residual limb has not yet been carried out: the socket and the prosthesis need ad-hoc modifications. However, the FSR-based sensor was applied on the patient’s flexor carpi ulnaris by means of an armband (see Figure 64,A) to test patient’s ability to control prosthesis movements. Despite the partial atrophy of the forearm muscles, after calibration, the patient immediately showed familiarity with it, managing to proportionally control the opening (see Figure 64,B) and closing (see Figure 64,C) of the “Federica” hand.

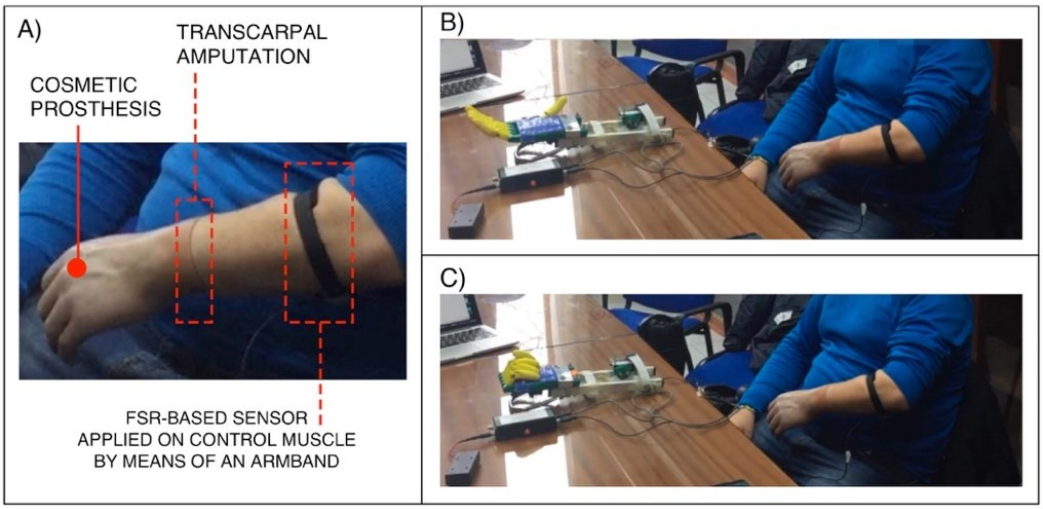

Figure 64. “Federica” hand tested on a patient with transcarpal amputation: a) image showing the positioning of the FSR-based sensor by means of an armband on the target muscle; b) example of rest condition corresponding to the opening of the prosthetic hand; c) example of muscle contraction corresponding to the proportional closing of the prosthetic hand.

Chapter 5

Discussion and Conclusions

Discussion

The current doctoral dissertation presented the 3D printed, low-cost, myo-controlled "Federica" hand, especially intended for research studies and developing countries, and provides the readers with all the knowledge necessary for the reproduction of the device; therefore, the CAD modelling files of the 3D printable components and the software developed for the Arduino platform are proposed to be public and free. The actual dimensions of the device are suitable for an adult man, on the other hand, the dimensions can be easily rescaled to adapt them to an adult woman or a child. However, the motor housing would need to be redesigned in order to fit the prosthesis with a socket for the patient's arm stump. A possible solution to address this issue in case of transradial amputation, was tested in a simulation environment and consists of a different version of the "Federica" hand, which includes the servomotor inside the palm (see Figure 65). The layout of both the palm and the mechanical components was changed; in particular, the palm was extended and raised, in order to house the servomotor.

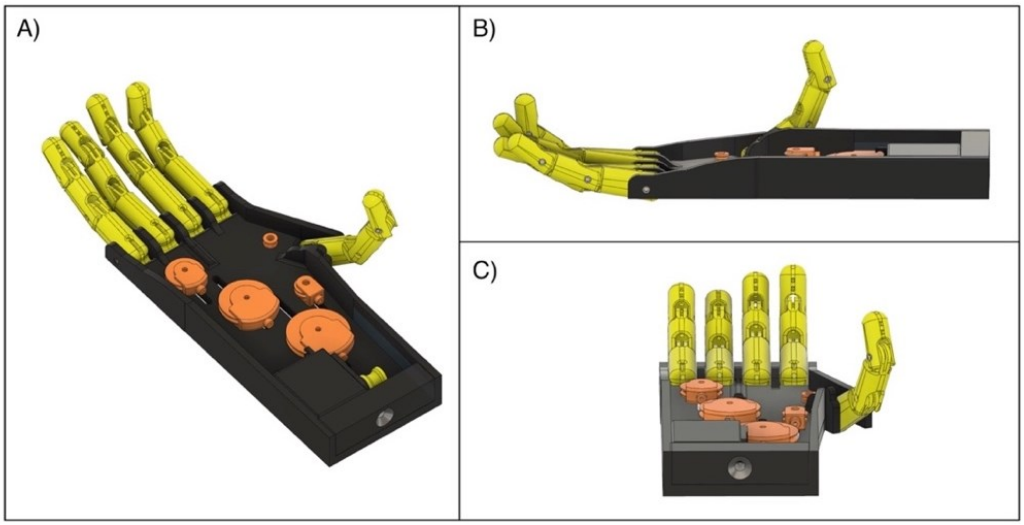

Figure 65. 3D renderings of the “Federica” hand with built-in servomotor: a) Top view; b) Side view; c) Bottom view.

Figure 66 illustrates a possible arrangement of the prosthetic device combined with a 3D printed socket for the arm stump. In the proposed design, the socket embeds the FSR-based sensor housing, in correspondence with the muscle assigned to the control. An aluminium tube, fastened in the distal part of the socket, ends with a screwed joint which is fixed in an ad-hoc slot of the hand prosthesis. The vibration motor for providing the sensory feedback of the grip force [47,74], is attached to the external surface of the socket. The battery pack (removable) and the control system box, are hooked around the aluminium tube. Finally, the switch to turn on the device, is located on the control system box.

Each prosthesis socket should be custom-made for the specific patient, according to his level of amputation. Indeed, in case of a long transradial amputation, it would be necessary to design alternative solutions for the positioning of the battery pack and the control system. On the other hand, in case of transcarpal amputation (see Figure 64), where wrist disarticulation is still present, the version of the prosthesis with built-in servomotor could not be suitable, as it would create a too long limb compared to the natural one.

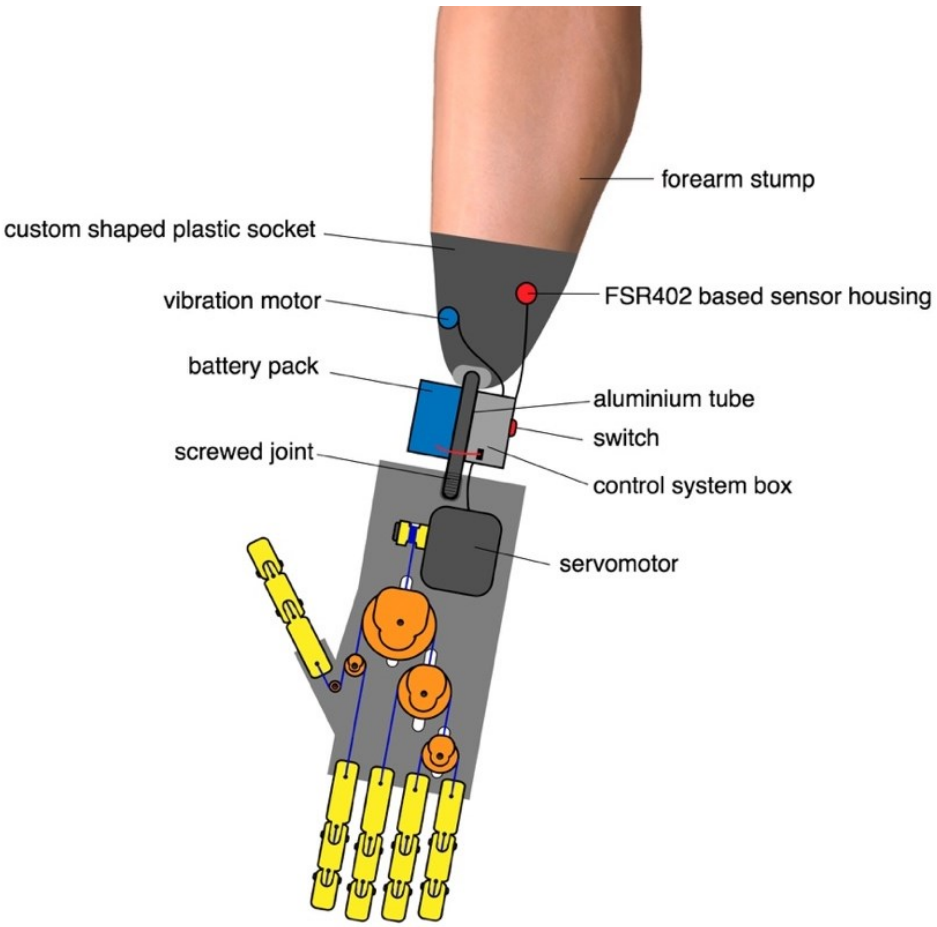

Figure 66. Illustration of a possible configuration of the prosthetic device on an amputee patient (transradial amputation). The arrangement consists of a 3D printed socket and a realization of "Federica" hand with built-in servomotor. The figure also shows the approximate positions of the various components (FSR-based sensor, vibration motor, control system, battery pack).

Conclusions

The "Federica" hand is a low-cost prosthetic device, which allows to perform many actions in daily life. The prosthesis design presents various innovative aspects and advantageous solutions, that can potentially be adopted by other projects.

The mechanical differential system provides a balanced force distribution to the fingers and allows a secure grip on a great variety of objects, regardless of their shape and deformability. The absence of return springs (used in many prosthetic devices for passive hand opening [1,2]) and the closed loop chain of tendons, contribute to the energy transmission efficiency of the prosthesis. The apparently low value of energy efficiency of about 12.85%, is most likely due is due to the anthropomorphic structure of the prosthesis and to the frictions generated by its mechanical components; higher values can be obtained with hooked prostheses [4,5]. However, thanks to the adaptive grip of the

prosthesis that is able to wrap around any shaped object [47,77,94,95], a mean power grip force of 8.80N (SD: 0.74 N) [95] is enough to support the user in many actions of daily life [104]. Moreover, the “Federica” hand showed a mean hysteresis (dissipated energy) of 106.80 Nmm, which resulted much lower than most of the considered prostheses [4,5]. About the energy required from the prosthesis functioning, it was tested that by using a battery pack of 7.4 V (2x 3.7V - 3000 mAh) an autonomy for at least an entire day is predicted.

The control signal based on force-myography, offers a valid alternative to the EMG to effectively control the prosthesis. The FSR-based sensor, is extremely cheap, thin and can be easily placed on target muscles. FSR can operate in wet environments and does not suffer from electromagnetic interferences. The FSR provides a ready-to-use signal that does not require any processing, unlike the EMG. By using FSR sensors, the training phase seems to be much simpler and faster for users. Furthermore, in spite of the electromechanical delay, the FMG muscle onset timing does not differ very much to that provided by the EMG envelope [96]. This contributes to the remarkable activation speed of the "Federica" hand.

The significant activation speed of the "Federica" hand is due to both its mechanical design and the FMG control system. Even considering the performances of recent and sophisticated prostheses available on market (0.35s for Michelangelo by Ottobock, 0.80s for iLimb Quantum by Touch Bionics, 1s for BesBionicV3 by Steeper) [1,2,98,99], the "Federica" hand takes less than 0.5 seconds from the muscle sensor trigger, until to the complete closure of the hand [95]. As further evidence, experimental tests carried out on healthy subjects showed the capability to grab objects on the fly [47] after a very short training.

"Federica" hand can also provide the user with a tactile sensory feedback of the grip force, by means of a small vibrating motor, which can be also inserted in the prosthesis socket. Not all the prostheses provide feedback and the user is enforced to use only the visual feedback to make sure that the hold has taken place. Restoring tactile sensation in hand prostheses is helpful to improve user experience and manipulation performances [74].

Finally, the cost for the realization of the "Federica" hand is considerably lower compared to commercial devices and also to many other prototypes [1,2]. Obviously, the manual labour for assembling parts was not estimated. However, the low cost and the relative simplicity of assembly, make the "Federica" hand ideal for use in poor and developing countries.

Certainly, many improvements could still be carried out. First, an aesthetic silicone glove would be useful for better device acceptance. At present the device allows only one

grip modality: the grasping with the simultaneous activation of all five fingers. The prosthesis could be modified to perform other gestures, such as pinch or precision grip. The "Federica" hand, as an open project, can offer some help to those in need and can stimulate other researchers or technicians to bring new ideas and solutions.

Chapter 6

Future Trends and Applications

Array armband of force sensors for gesture recognition purpose and prosthetic control

Introduction

Human Machine Interfaces (HMI) are becoming increasingly widespread with applications spanning from assistive devices for disability, muscle rehabilitation, prosthesis control, remote manipulation, and gaming controllers [113,114]. Being the hand extremely important in one's life, an entire field of HMI is dedicated to hand gesture recognition applications. Generally, visual, electromyographic, or inertial sensors are the most used technologies for detecting hand gestures [130,131]. Visual-based hand gesture recognition systems do not need any device to wear, allowing for extreme freedom of use. Such remote sensing is very attractive, but its performances are heavily influenced by many factors such as camera field of view, challenging image processing, illumination conditions, objects overlapping, etc. [115,116]. Devices based on surface electromyography (sEMG or simply EMG) recordings [117,118] need electrodes in steady contact with the skin, and they are prone to motion artifacts, electromagnetic noise and crosstalk with other biopotentials. They also require real-time processing of the raw sEMG signals to extrapolate useful features (e.g. sEMG envelope/RMS) [28]. As example, Myo Armband by Thalmic Labs, a commercial device based on eight sEMG sensors and an inertial platform, allows the user to interface via Bluetooth with PCs or mobile devices to control supported applications [119–121] including robot motion [122].

As an alternative to sEMG, other sensors can monitor the mechanical muscular activity, and some are briefly presented below. A pressure sensors array coupled to air-bladders mounted on an armband was proposed to detect hand motion (accuracy of 90%) by monitoring the swelling of muscles [31]. The air bladders are cumbersome, uncomfortable, and not widely adaptable. A wristband composed of an array of barometric pressure sensors was proposed to estimate tendons and muscle motions during gestures [123], reaching a classification accuracy of wrist gestures of 98%. A combination of sEMG electrodes and microphones [124] was used to detect both electrical muscle activity and the mechanomyogram (MMG – i.e. mechanical vibrations produced during muscle contraction). The microphones presented high sensitivity to noise and motion artifacts, in addition to the aforementioned EMG problems. A conventional ultrasound probe fixed to the forearm was proposed for finger motion recognition, proving accuracy of 96% [125]. This approach resulted very cumbersome, uncomfortable and required a complex image processing for gestures features extraction. Furthermore, piezoelectric sensors were used to estimate finger gestures (accuracy of 97%) by recording the vibrations and shape changes that occur at the wrist due to muscles and tendons motions [126]. These kinds of sensors could also be employed to harvest energy from body movements, including upper limb motion [127].

Other recent studies [128] presented devices for gesture recognition based on an array of Force-Sensitive Resistors (FSRs) [78]. A combination of two sEMG and four FSR sensors, mounted on a wrist strap, can be used to classify finger movements scoring accuracy of 96% [129]. An armband equipped with sixteen FSR sensors positioned on both wrists and forearms [130] allowed the classification of several hand gestures with an accuracy of about 97%. A similar device equipped with eight FSR sensors, tested on amputees [131] while trying to mirror different hand grips in their residual forearm muscles, yielded an accuracy of 70%. Moreover, a high-density grid of 126 FSR sensors [23] embedded in a forearm prosthetic socket and tested on healthy subjects to recognize arm positions, yielded an accuracy of 99.7%.

However, the approaches proposing pressure sensors wrapped around the wrist, do not directly monitor muscle contraction, but rather tension of tendons. Moreover, even in the cases of FSR arrays applied on the forearm, to the best of our knowledge, the detected signals were not proven to be equivalent to EMG.

The aim of this study was to investigate the possibility to recognize hand gestures by monitoring the contractions of a reduced number of specific forearm muscles, via the bespoke FSR-based sensors, which demonstrated to provide signals quite similar to the EMG linear envelope (EMG-LE) [62]. To reach this goal, a new gesture recognition

armband is presented; it is equipped with only three FSR based sensors, applied on specific forearm muscles to recognize eight hand gestures. The armband is designed to be easily wearable and adjustable for any user. Thanks to the similarity with the EMG-LE [62], the device could be reconfigured to resemble previous, well-established EMG based HMIs (e.g., exergaming applications for patients during neuromotor rehabilitation) [132].

Piezoresistive array armband design

The armband consists of three FSR-based sensors (presented in section 2.1), as depicted in Figure 67. The support was designed with a housing site for the FSR, and an opening to allow sensor sliding along the band and precise positioning on a target muscle. The armband can be wrapped around user's forearm and fastened with a Velcro strip in order to measure muscle contractions and recognize hand gestures. Indeed, each gesture generates a characteristic force distribution on the sensors, and this allows discriminating the intentional movements.

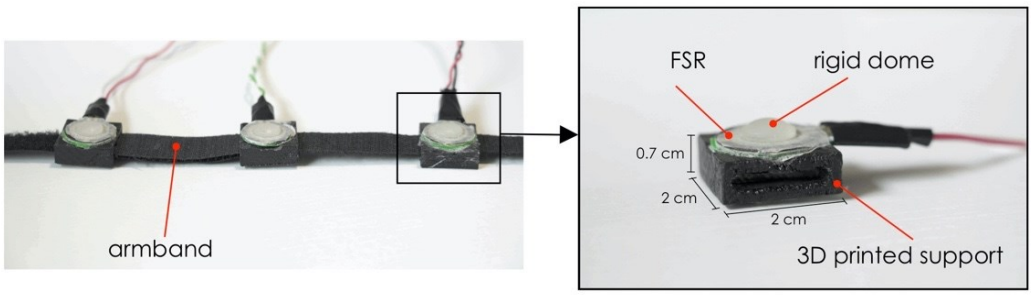

Figure 67. Piezoresistive array armband: on the left the armband with three FSRs; on the right an enlargement of the FSR-based sensor mounted on its 3D printed support with actual dimensions.

Given the similarity between the FSR-based sensor output and the EMG-LE [62], the muscle sensors should be positioned above the muscle belly as for EMG detection. The chosen muscles should be superficial to allow advantageous signal to noise ratio. Moreover, since the FSR-based sensors are embedded in an armband, the pick-up points should belong to a circumference that wraps around the forearm. Three forearm muscles were preferred to better discriminate the different hand gestures. In detail, FSR1 was applied on flexor carpi ulnaris, FSR2 on flexor carpi radialis and FSR3 on extensor digitorum. The armband was positioned proximally at 25% of the distance between the olecranon and the process styloideus ulnae of the right forearm (see Figure 68). Indeed, a functional-anatomical analysis of the forearm muscles [93] revealed that flexor carpi ulnaris is mainly involved in wrist flexion and wrist adduction; flexor carpi radialis in wrist flexion and wrist abduction; extensor digitorum in fingers extension, fingers abduction and wrist extension.

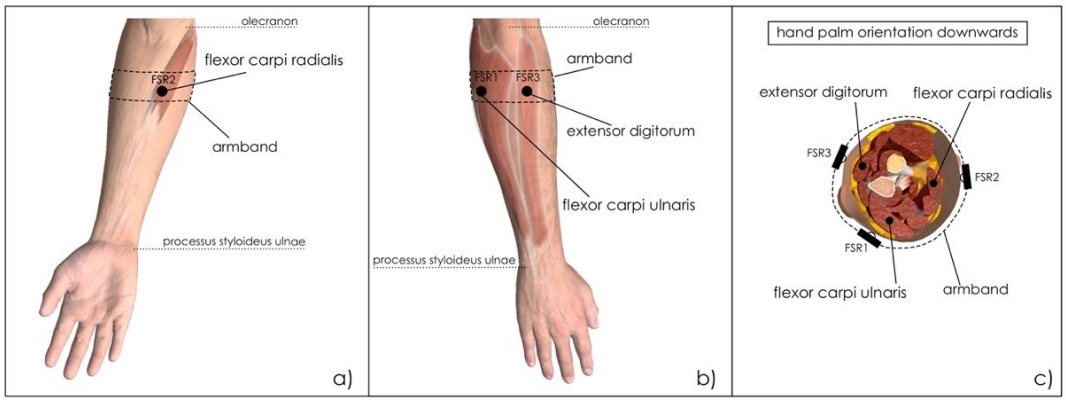

Figure 68. Placements of FSRs on forearm muscles: a) Ventral view of right forearm: FSR2 sensor on flexor carpi radialis; b) Dorsal view of the right forearm: FSR1 on flexor carpi ulnaris and FSR3 on extensor digitorum; c) Right forearm cross-section: FSRs placement onto the aforementioned muscles.

A current mirror (see Figure 69) was used as a conditioning circuit for each FSR-based sensor [94,95]. It was made of a pair of common npn BJT (2N2222), positioned very close to each other. Basically, the current mirror replicates the FSR-based sensor (R_{FSR}) current in the gain resistor (R_G), thus providing a linear load-to-voltage response and allowing the output voltage to swing through the full voltage supply range. The sensibility of each muscle sensor can be varied by changing the R_G value. Thanks to its low energy consumption, this conditioning circuit can be directly supplied by microcontrollers or ADC boards (e.g. 3.3V or 5V). V_{CC} was set to 5V, and the gain resistors R_{G1}, R_{G2}, and R_{G3} were set to 850 Ω, 790 Ω and 960 Ω respectively to equalize the gains of the three channels.

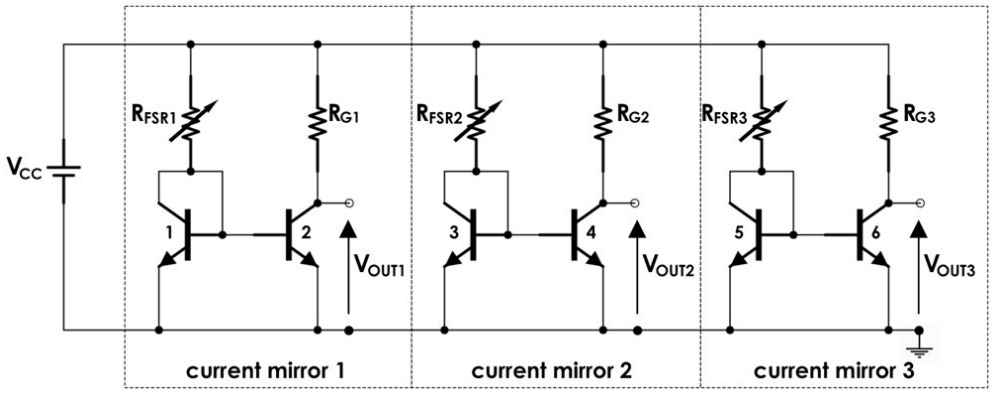

Figure 69. FSR-based sensors conditioning circuit based on mirror current circuits.

Static calibrations were performed for each FSR-based sensor, to evaluate the relationship between the muscular force exerted on the FSR, reported in Kg, and the voltage output V_{OUT} (see Fig 3) [62]. Each sensor was placed on a precision electronic

scale, then different weights were applied on active sensor area perpendicularly to the dome, and the corresponding output voltages were recorded. The output signals were acquired at 1kHz sampling frequency with 12-bit precision by means of National Instruments NI USB-6008 acquisition board.

Machine learning algorithms applied to hand gesture classification

The experimental tests involved 10 subjects (8 men and 2 women aged from 25 to 64 years), who provided their informed and written consent. Each participant comfortably sat on an adjustable height chair, leaning against its fixed seatback, in front of a desk with a computer screen. He was asked to place his elbow on the desk, forming an angle of about 45° between the forearm and the desktop. The armband was appropriately positioned on the forearm, and the pressure at rest was recorded by the sensors and resulted 100 g/cm^2 on average. The subjects were asked to perform 10 repetitions of each hand gesture class (see Figure 70) in the following order: rest; wrist flexion; wrist extension; wrist adduction; wrist abduction; wrist rotation (supination); finger abduction; clenched fist; holding the final hand posture for a couple of seconds and resting for a few seconds before the next movement. After the 10 repetitions of each hand gesture class, the participant was allowed to rest for about a minute. Simultaneous recordings from the three FSR-based sensors ($V_{OUT\ 1\text{-}2\text{-}3}$) were collected via the NI USB-6008 board at 1 kHz sampling frequency with 12-bit precision.

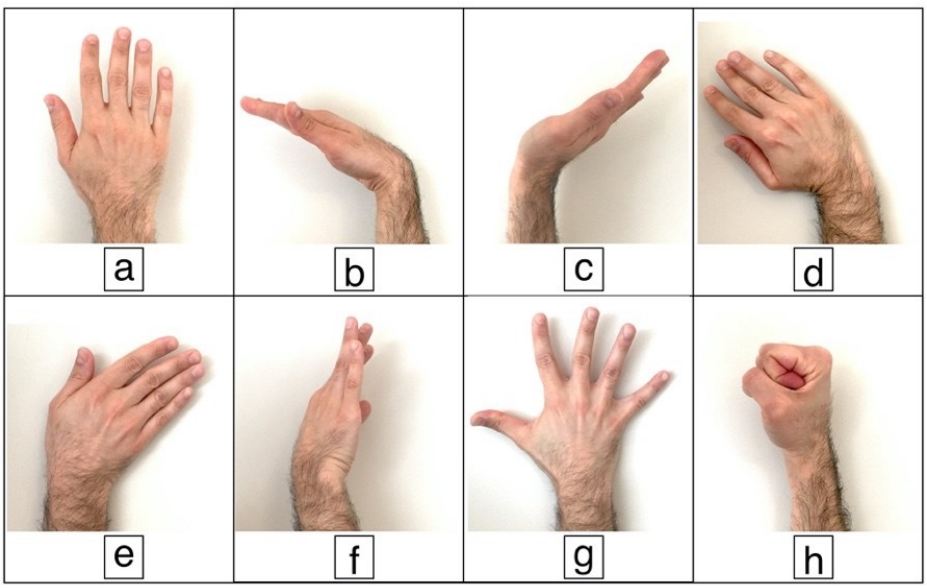

Figure 70. Performed hand gestures: a) rest; b) wrist flexion, c) wrist extension, d) wrist adduction, e) wrist abduction, f) wrist rotation (supination); g) fingers abduction; h) clenched fist.

The raw signals were firstly pre-processed, by subtracting the minimum signal values recorded at rest (FSR offsets due to the armband fastening pressure) and normalizing to

the absolute maximum value. In order to avoid manual selection of each hand gesture, pre-processed data were automatically segmented to extract the time intervals corresponding to the final hand postures. Segmentation was achieved by selecting the FSR signal with maximum variation (peak-to-peak amplitude) and applying an heuristically chosen threshold set at 40% of this value, which guaranteed appropriate segmentation of all gestures. Means and standard deviations (SDs) of the three FSR signals were computed for each segment. Then, for each gesture instance, the three means and the three SDs computed in the corresponding segment were considered as features. In detail, the features extracted from all the gestures instances in a single trial of a subject, were assembled in a database consisting of an 80x7 matrix (10 repetitions for each of the 8 hand gestures); each row corresponded to a single gesture instance and was composed by the following seven elements: [FSR1_mean, FSR2_mean, FSR3_mean, FSR1_SD, FSR2_SD, FSR3_SD, GESTURE_LABEL].

Then, different machine learning algorithms (Linear/Polynomial/Radial Basis Function - Support Vector Machines; Linear Discriminant Analysis; Quadratic Discriminant Analysis; Random Forest; K-Nearest Neighbors, Neural Networks) were used for model training and data classification, by means of "Weka" software [133]. The conceptual scheme of the entire process of hand gestures classification is depicted in Figure 71.

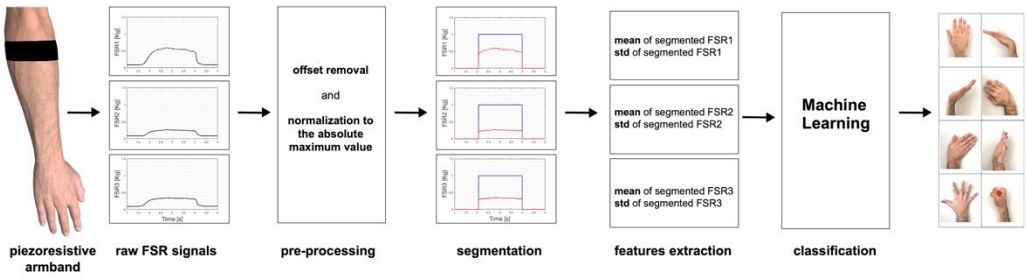

Figure 71. Schematic illustration of the hand gesture recognition system.

Classification performances were assessed by applying the 10-fold and leave-one-out cross validations on each of the ten subjects' databases. In 10-fold cross-validation, the dataset is randomly divided into 10 subsets of equal size, and then each subset is tested using the classifier trained on the remaining 9 subsets. Then, the obtained 10 classification accuracies were averaged to provide an overall classification accuracy. Instead, leave-one-out cross-validation is simply n-fold cross-validation, where n is the number of instances in the dataset. Each instance, in turn, is left out, and the learning

method is trained on all the remaining instances. Finally, all the n classification accuracies were averaged to yield an overall classification accuracy [133].

Furthermore, the classification performances of the different machine learning algorithms were also tested on a combined database, obtained by joining all subjects' databases.

Finally, the possibility to classify gestures with less than three sensors was tested by considering features from different sensors pairs (FSR1-FSR2, FSR1- FSR3, FSR2-FSR3) and even from a single sensor (FSR1, FSR2, FSR3). In the case of sensors pairs, each instance is characterized by four features (2 means and 2 SDs), while for a single sensor, the features reduced to two.

Real-time implementation of hand gesture recognition

A linear SVM classifier was implemented on an Arduino UNO board [134,135], equipped with an ATmega328 (Atmel) microcontroller, to provide real-time gesture recognition. The three outputs of the FSR sensors conditioning circuit were directly connected to the analog inputs of the board. In addition, custom graphical user interfaces (GUI) were designed by means of "Processing" software [136] to facilitate interactive armband calibration and to allow real-time user interaction with a computer. The real-time application involved the steps described below. For device calibration, the subject was asked to wear the armband and to perform the same sequence of gestures described in section "*Machine learning algorithms applied to hand gesture classification"*. Data were sent to the PC and used to train a Linear SVM classifier by means of Weka software; the trained classifier parameters were sent to the Arduino board, and the calibration phase was completed (see Figure 72,a). The videogame started on the PC screen and the Arduino board performed real-time classification of the current gesture: extracting gesture features (mean and SD) every 100 ms, making a classification and sending this information (coded in 1 byte) to the PC at a 10 Hz rate, via USB communication (see Figure 72,b). The subject started to play, and the Arduino board output was used to replace the keyboard and mouse controls. The subject never removed the armband between these steps. For each gaming session, the gestures correctly recognised in real-time were annotated and then their percentages were computed. Each user was also asked to evaluate the comfort and effectiveness of the device on a 0-to-10 scale. The implementation of a real-time LDA classifier was further tested, repeating the same procedure described for the Linear SVM.

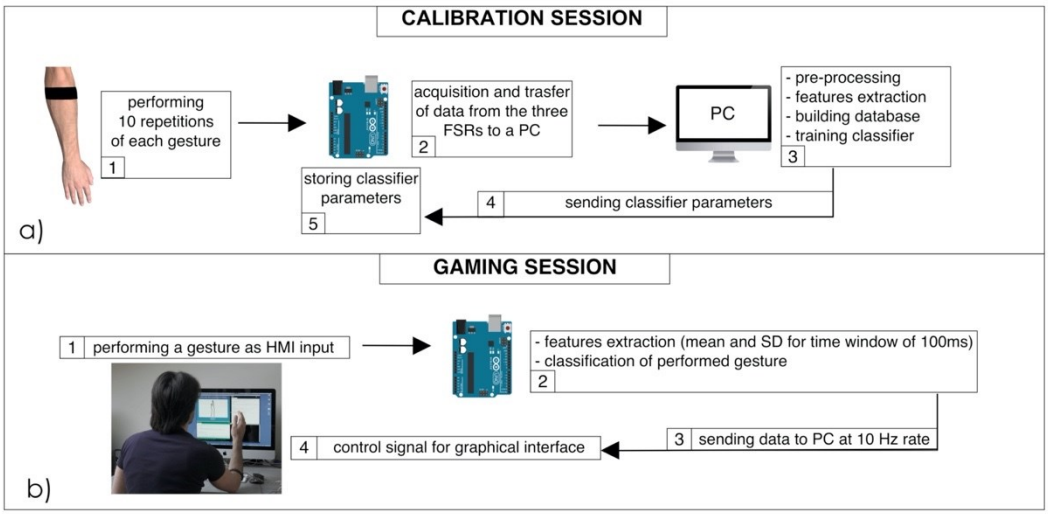

Figure 72. Real-time HMI: a) block diagram of the calibration phase; b) block diagram of the gaming session.

Results

Figure 73 shows an example of the FSRs raw signals for each performed hand gesture (subject #3). Different intensity force scales were used to better appreciate the signals shapes.

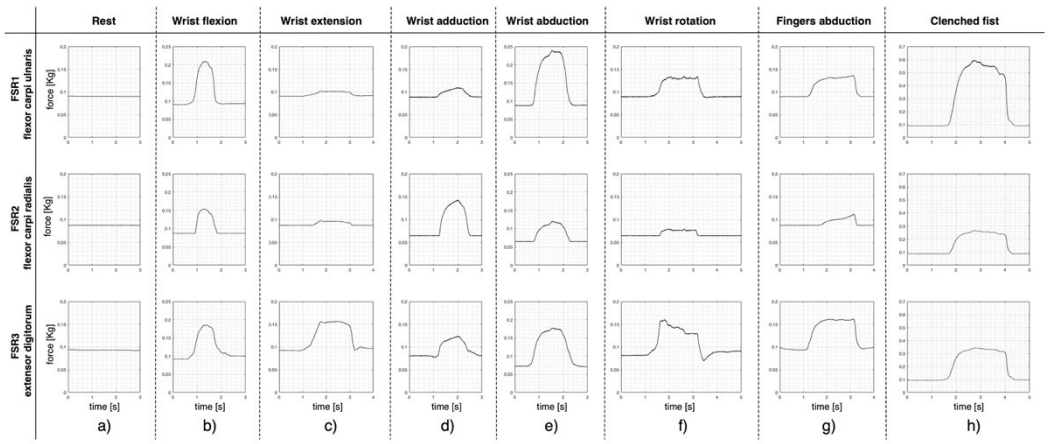

Figure 73. Examples of raw signals (subject #3) recorded by the three FSRs for each performed gesture. Signal amplitudes are expressed in kilograms (different force scales were used).

An example of raw signal segmentation is showed in Figure 74. The segmentation function was achieved by applying a threshold set at 40% of the FSR3 maximum signal variation. The segmentation allowed us to extract only the samples associated with the fully reached gesture while discarding the initial and final transients.

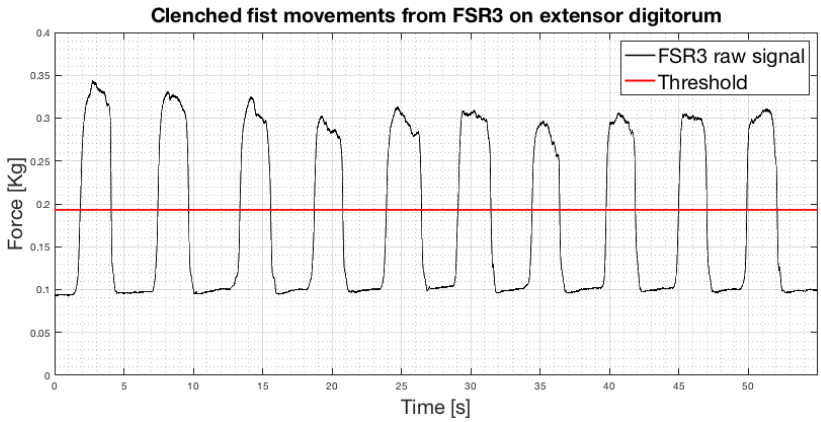

Figure 74. Recording of 10 consecutive clenched fist movements from FSR3 (subject #3): FSR3 raw signal with the superimposed threshold (red line).

Moreover, analyzing the values of the segmented signals for each clenched fist movement in Figure 74, it was found that the distributions of the occurrences do not seem Gaussian. These probability distributions showed up also from the segmented signals related to the other gestures. The median, as an alternative to the mean, would be another possible feature. As an example, Figure 75 shows the means, the standard deviations, and the medians referred to the segmented signals depicted in Figure 74. In this case, the percentage variation between the mean and the median was less than 2% for each repetition. Comparable percentages were also found in the segmented signals related to the other gestures. Hence, there is not practical convenience in using medians instead of means because it would increase the computational burden (critical for real-time applications).

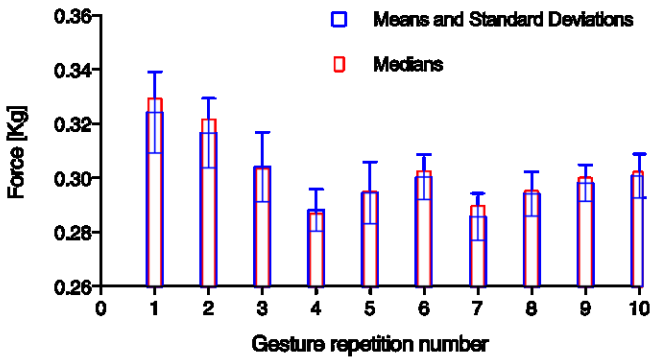

Figure 75. Means, standard deviations, and medians related to the segmented FSR3 signals of 10 clenched fist movements showed in Figure 74.

As an example, Figure 76 shows the means corresponding to the 10 repetitions of each gesture (subject #3) with different colors (see legend of Fig 10) in a three-dimensional space (x, y, z axes correspond to FSR1, FSR2, and FSR3 respectively). In addition, data were enriched by reporting centroids and standard deviations (computed in

the three directions). Gestures appeared to be confined in specific regions, which did not overlap with each other. It is interesting to note that the rest condition was located around a point that represented the grip force of the armband (here about 0.1 Kg).

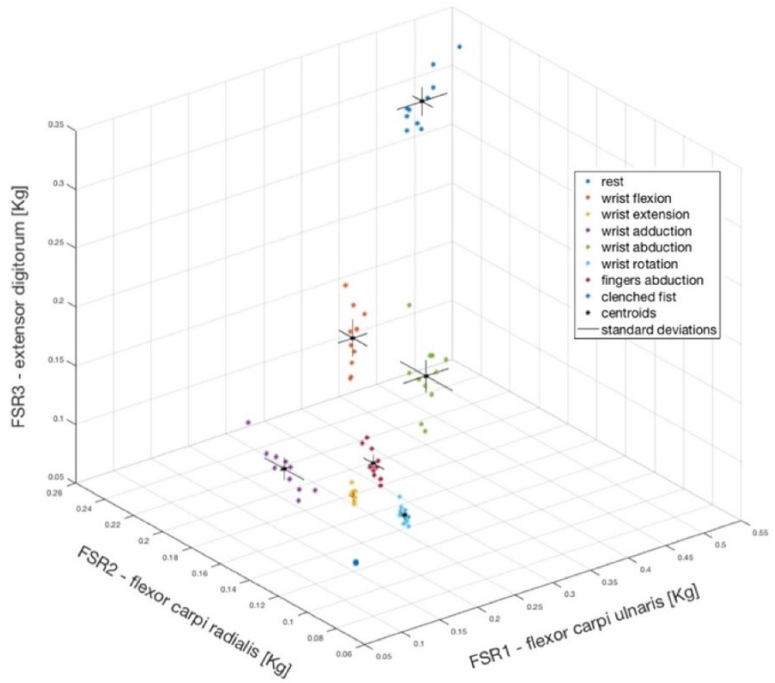

Figure 76. Mean values computed for each of the 10 repetitions of each gesture (coded with different colors). FSR1, FSR2, FSR3 correspond to x, y, z axes, respectively. For each gesture, the centroid is depicted as a black asterisk and the standard deviations in the three directions as continuous black lines.

Considering all three FSRs, the classification accuracy achieved for each subject, by means of the different algorithms and cross-validation methods are shown in Table 10.

Table 10. Classification accuracies (in percentage) on 10 different subjects, using different machine learning algorithms (Linear SVM (L-SVM); Polynomial SVM (P-SVM), Radial Basis Function SVM (RBF-SVM); Linear Discriminant Analysis (LDA); Quadratic Discriminant Analysis (QDA); Random Forest (RF); K-Nearest Neighbors (K-NN), Neural Networks (NN)) and different cross-validation methods (10-fold (CV1), leave-one-out (CV2)).

	L-SVM		P-SVM		RBF-SVM		LDA		QDA		RF		KNN		NN	
	CV1	CV2	CV1	CV2	CV1	CV2	CV1	CV2	CV1	CV2	CV1	CV2	CV1	CV2	CV1	CV2
S1	95	95	87.5	81.25	93.25	91.25	97.5	97.5	97.5	97.5	96.25	96.25	91.25	91.25	90	92.5
S2	92.5	87.5	73.75	76.25	90	88.75	95	96.25	96.25	96.25	89	88.75	88.50	88.75	83.75	86.25
S3	98.75	98.75	82.5	78.75	97.5	96.25	97.5	96.25	100	100	97.5	97.5	95	93.75	97	96.25
S4	96.25	96.25	80	83.75	96.25	96.25	96.25	96.25	98.75	98.75	97.5	97.5	100	100	100	100
S5	90	88.75	75	73.75	90	97.5	93.75	92.5	97.5	97.5	93.5	93.75	91	90	91.5	90
S6	100	100	85	86.25	100	100	100	100	98.75	98.75	97.5	97.5	98.75	98.75	98.75	98.75
S7	97.5	97.5	97.5	93.75	97.5	97.5	100	100	98.75	98.75	97.5	95	100	100	98.75	97.5
S8	97.5	96.25	92.5	92.5	97.5	96.25	98.75	98.75	98.75	98.75	100	100	97.5	97.5	98.75	98.75
S9	96.25	96.25	83.75	86.25	97.5	96.25	96.25	96.25	98.75	98.75	98.75	98.75	98.75	98.75	100	100

S10	96.25	95	75	86.25	96.25	96.25	97.5	96.25	93.75	93.75	93.75	93.75	98.75	98.75	97.5	97.5

Figure 77 shows the means and the standard deviations of the accuracies achieved across all participants, using the aforementioned machine learning algorithms and the two cross-validation methods.

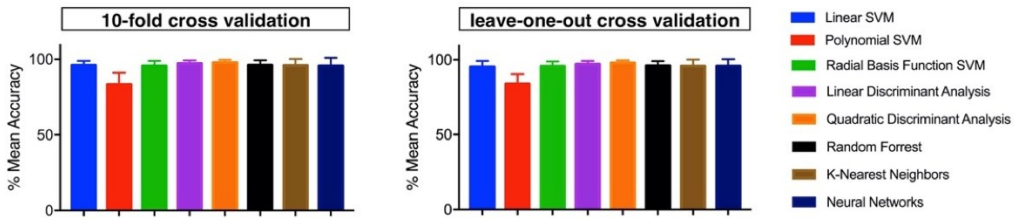

Figure 77. Means and standard deviations of the accuracies achieved across the 10 participants, by means of the different machine learning algorithms and for each tested cross-validation method (10-fold and leave-one-out).

Table 10 shows that Linear SVM and LDA algorithms allow to obtain higher classification accuracies with lower computational complexities, compared to all the other evaluated machine learning algorithms. Therefore, more extended analysis was focused on these classifiers, considering the 10-fold cross validation.

Table 11 summarizes the classification performances achieved by considering all sensors combinations, reporting means and standard deviations of the related accuracies (across all participants). Using a single sensor, the mean classification accuracy was about 77% for Linear SVM, while about 82% for LDA. Moreover, using two sensors the accuracy increased to about 91% for Linear SVM, while about 92% for LDA.

Table 11. Means and standard deviations of classification accuracies (across all participants) by using Linear SVM and LDA algorithms for all sensors combinations.

Selected sensor/s	**Linear SVM** **mean (SD) accuracy %**	**LDA** **mean (SD) accuracy %**
FSR1	80.25 (9.89)	80.62 (8.00)
FSR2	76 (9.12)	82.37 (10.38)
FSR3	73.88 (13.25)	82.05 (8.58)
FSR1 and FSR2	91.75 (8.70)	92.27 (6.96)
FSR1 and FSR3	92.25 (5.26)	91.62 (6.18)
FSR2 and FSR3	90.38 (5.68)	92.87 (4.41)
FSR1 and FSR2 and FSR3	96 (2.93)	97.25 (2.02)

Table 12 outlines the classification performances obtained for the combined database (all subjects) by using Linear SVM and LDA for all sensors combinations.

Table 12. Classification accuracies reached on the combined database by using Linear SVM and LDA for all sensor combinations.

Selected sensor/s	Linear SVM Accuracy %	LDA Accuracy %
FSR1	41.5	32.62
FSR2	38	28.5
FSR3	37.1	33.87
FSR1 and FSR2	49.6	44
FSR1 and FSR3	49.6	37.37
FSR2 and FSR3	51.9	41.12
FSR1 and FSR2 and FSR3	58.5	44.50

Table 13 shows the classification accuracies reached with Linear SVM, for each subject and hand gesture class. The average accuracy across all participants resulted 96 % (SD: 2.93 %), and the confusion matrix (right and wrong average recognition percentages across all 10 subjects) is shown in Figure 78.

Table 13. Linear SVM classification accuracies (in percentage) on 10 different subjects in recognizing eight hand gestures (classes).

Gesture (Class)	S1	S2	S3	S4	S5	S6	S7	S8	S9	S10
rest	100	100	100	100	100	100	100	100	100	100
wrist flexion	90	100	100	100	100	100	100	100	100	100
wrist extension	100	90	100	100	90	100	100	100	100	90
wrist adduction	100	90	100	100	100	100	90	90	90	80
wrist abduction	80	70	100	80	60	100	100	90	100	100
wrist rotation	90	100	90	100	80	100	90	100	100	100
fingers abduction	100	90	100	90	90	100	100	100	80	100
clenched fist	100	100	100	100	100	100	100	100	100	100

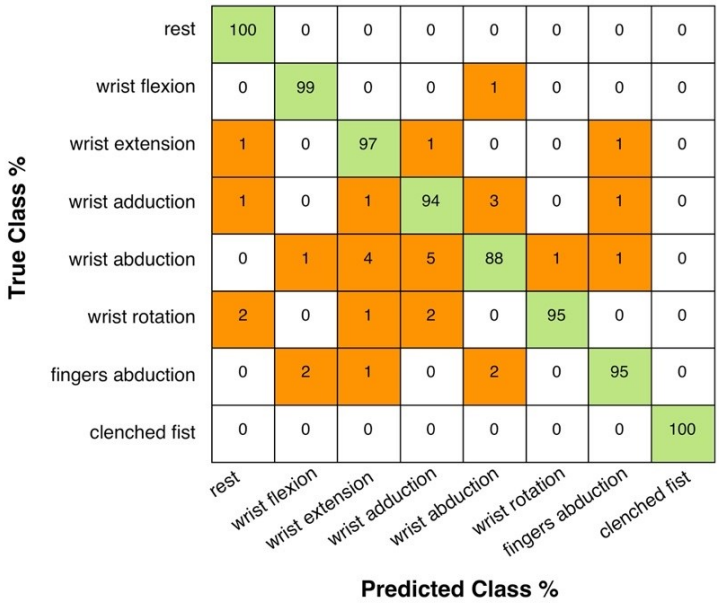

Figure 78. Confusion matrix (across all participants) presenting the Linear SVM classification accuracies (in percentages): rows correspond to true performed hand gestures and columns to predicted hand gestures.

Table 14 shows the classification accuracies reached with LDA, for each subject and hand gesture class. The average accuracy across all participants resulted 97.25 % (SD: 2.02 %), and the confusion matrix (right and wrong average recognition percentages across all 10 subjects) is shown in Figure 79.

Table 14. LDA classification accuracies (in percentage) on 10 different subjects in recognizing eight hand gestures (classes).

Gesture (Class)	**S1**	**S2**	**S3**	**S4**	**S5**	**S6**	**S7**	**S8**	**S9**	**S10**
rest	100	100	100	100	100	100	100	100	100	100
wrist flexion	100	100	100	100	90	100	100	100	100	90
wrist extension	100	90	100	100	90	100	100	100	100	100
wrist adduction	100	100	90	80	90	100	100	90	80	90
wrist abduction	90	70	100	90	90	100	100	100	100	100
wrist rotation	90	100	90	100	90	100	100	100	100	100
fingers abduction	100	100	100	100	100	100	100	100	90	100
clenched fist	100	100	100	100	100	100	100	100	100	100

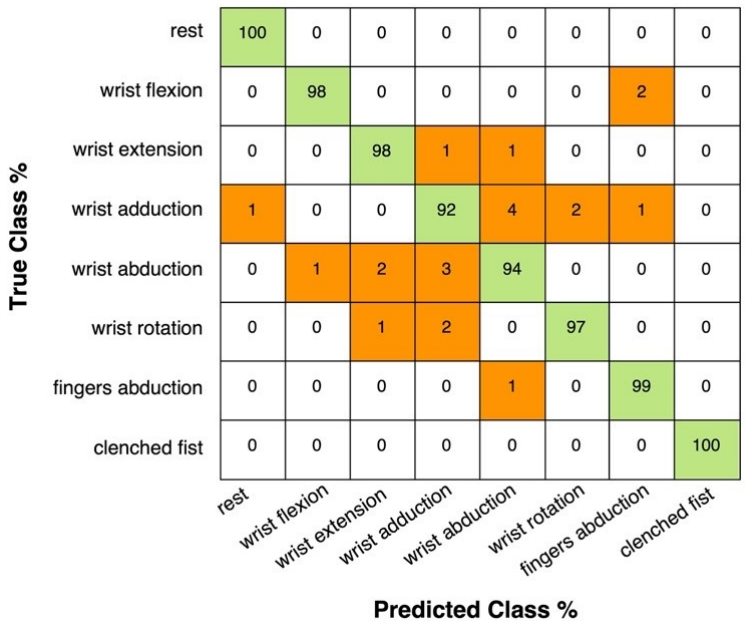

Figure 79. Confusion matrix (across all participants) presenting the LDA classification accuracies (in percentages): rows correspond to true performed hand gestures and columns to predicted hand gestures.

Graphical interfaces for practical HMI applications

The custom graphical interface that displays icons corresponding to the recognized hand gestures, was used both for calibration purposes and for quick assessment of real-time classifier performances (see Figure 72). The real-time gesture recognition system was used to play various games (e.g. "Pong" videogame) by replacing the mouse and keyboards commands with those provided by the Arduino board [137]. The average percentage (across all users) of correctly recognized gestures resulted 93% with Linear SVM, while 90% with LDA. Subjects reported that this HMI was comfortable to wear and intuitive to use, not requiring long training to achieve good results.

Discussion and Conclusions

A novel piezoresistive array armband for hand gesture recognition was presented in this study. It was based on a reduced number of muscle contraction sensors, appropriately positioned on specific forearm muscles. Nevertheless, it allowed discriminating eight classes of hand gestures with remarkable accuracy, regardless of the specific classifier (see Table 10). Classifiers based on Linear SVM and LDA have low computational complexities and can be easily implemented in hardware. Therefore, more extended analysis was focused on these classifiers. The average classification accuracy across all subjects, resulted 96% for Linear SVM and 97.25% for LDA. These performances were achieved by separately considering the databases associated with each user and averaging

the accuracies. Instead, considering the combined database (all subjects) the Linear SVM classification achieved a maximum accuracy of 58.5%, while LDA scored 44.5%. A significant classification accuracy was also achieved by considering combinations of only two sensors: the mean accuracy resulted 91.46% for Linear SVM and 92.25% for LDA. As expected, the use of a single sensor led to a significant reduction in mean classification accuracy (about 77% for Linear SVM and 82% for LDA). With regard to the reproducibility test (described in section 2.3), the mean classification accuracy (across all subjects) was 78.8% for Linear SVM and 60.25% for LDA. This reduction in accuracy suggests that each time the device is used, a new calibration (i.e. classifier training) is advisable for optimal performances. It could be interesting to extend this study to a much larger cohort of subjects, in order to obtain more reliable classification results, and also to investigate the possibility to discover common muscle activation strategies, to identify pathological behaviours, etc.

The proposed armband is extremely lightweight, simple to wear, and easily adjustable for any user. It is comfortable and unobtrusive, as proved by the low grip force values recorded at rest, and it allows to simultaneously monitor the contractions of multiple specific forearm muscles. It is also scalable in the number of sensors, thus giving the opportunity to avoid their precise positioning onto specific muscles (e.g. full sensors covered armband could be used). The extreme simplicity of FSR sensors and their conditioning circuits, along with the straightforward usability of the output signals (no additional processing required), allow to easily implement this system on low-performing, commercial platforms, also with wireless capabilities [11,12].

The proposed HMI could be applied in “exergaming” applications: graphical interfaces can provide patients with real-time feedback on the quality of the performed gestures, inducing self-corrections of their movements. Moreover, the possibility to monitor the contractions of specific muscles would provide additional clinical information about patients’ progress. Thus, the exergaming could be used in clinical practice to make neuromotor rehabilitation processes more stimulating and enjoyable.

The encouraging results obtained with few sensors, suggest the possibility to adopt this HMI also in hand prosthesis control [47,138,139], to the similarity of the FSR-based sensors outputs and the EMG-LE. Indeed, the small size and flatness of the sensors make it possible to embed them inside the prosthesis socket. More generally, the muscle contraction sensors could be potentially adapted to monitor other muscles (e.g. muscles of arms, legs, shoulders, etc.), allowing them to develop a wide range of EMG-based HMI applications.

References

1. Vujaklija, I.; Farina, D.; Aszmann, O.C. New Developments in Prosthetic Arm Systems. *Orthop Res Rev* **2016**, *8*, 31–39, doi:10.2147/ORR.S71468.
2. Belter, J.T.; Segil, J.L.; Dollar, A.M.; Weir, R.F. Mechanical Design and Performance Specifications of Anthropomorphic Prosthetic Hands: A Review. *J Rehabil Res Dev* **2013**, *50*, 599–618, doi:10.1682/jrrd.2011.10.0188.
3. Carey, S.L.; Lura, D.J.; Highsmith, M.J.; CP; FAAOP Differences in Myoelectric and Body-Powered Upper-Limb Prostheses: Systematic Literature Review. *J Rehabil Res Dev* **2015**, *52*, 247–262, doi:10.1682/JRRD.2014.08.0192.
4. Smit, G.; Bongers, R.M.; Van der Sluis, C.K.; Plettenburg, D.H. Efficiency of Voluntary Opening Hand and Hook Prosthetic Devices: 24 Years of Development? *J Rehabil Res Dev* **2012**, *49*, 523–534, doi:10.1682/jrrd.2011.07.0125.
5. Smit, G.; Plettenburg, D.H. Efficiency of Voluntary Closing Hand and Hook Prostheses. *Prosthet Orthot Int* **2010**, *34*, 411–427, doi:10.3109/03093646.2010.486390.
6. Basmajian, J.V.; Luca, C.J. de *Muscles Alive: Their Functions Revealed by Electromyography*; Williams & Wilkins: Baltimore, 1985; ISBN 978-0-683-00414-4.
7. Gargiulo, G.D.; Bifulco, P.; Cesarelli, M.; Fratini, A.; Romano, M. Problems in Assessment of Novel Biopotential Front-End with Dry Electrode: A Brief Review. *Machines* **2014**, *2*, 87–98, doi:10.3390/machines2010087.
8. Cesarelli, M.; Bifulco, P.; Bracale, M. Quadriceps Muscles Activation in Anterior Knee Pain during Isokinetic Exercise. *Med Eng Phys* **1999**, *21*, 469–478, doi:10.1016/s1350-4533(99)00068-5.
9. Medved, V. Standards for Reporting EMG Data.; 2000.
10. Stegeman, D.; Hermens, H. Standards for Suface Electromyography: The European Project Surface EMG for Non-Invasive Assessment of Muscles (SENIAM). **2007**, *1*.
11. Gargiulo, G.; Bifulco, P.; McEwan, A.; Nasehi Tehrani, J.; Calvo, R.A.; Romano, M.; Ruffo, M.; Shephard, R.; Cesarelli, M.; Jin, C.; et al. Dry Electrode Bio-Potential Recordings. *Annu Int Conf IEEE Eng Med Biol Soc* **2010**, *2010*, 6493–6496, doi:10.1109/IEMBS.2010.5627359.
12. Bifulco, P.; Cesarelli, M.; Fratini, A.; Ruffo, M.; Pasquariello, G.; Gargiulo, G. A Wearable Device for Recording of Biopotentials and Body Movements. In Proceedings of the 2011 IEEE International Symposium on Medical Measurements and Applications; May 2011; pp. 469–472.
13. Analysis and Modelling of Muscles Motion during Whole Body Vibration | SpringerLink Available online: https://link.springer.com/article/10.1155/2010/972353 (accessed on 16 November 2020).
14. Dosen, S.; Markovic, M.; Somer, K.; Graimann, B.; Farina, D. EMG Biofeedback for Online Predictive Control of Grasping Force in a Myoelectric Prosthesis. *J Neuroeng Rehabil* **2015**, *12*, 55, doi:10.1186/s12984-015-0047-z.
15. Oskoei, M.A.; Hu, H. Myoelectric Control Systems - A Survey. *Biomed. Signal Process. Control.* **2007**, doi:10.1016/j.bspc.2007.07.009.
16. Parker, P.; Englehart, K.; Hudgins, B. Myoelectric Signal Processing for Control of Powered Limb Prostheses. *Journal of Electromyography and Kinesiology* **2006**, *16*, 541–548, doi:10.1016/j.jelekin.2006.08.006.

17. Geethanjali, P. Myoelectric Control of Prosthetic Hands: State-of-the-Art Review. *Med Devices (Auckl)* **2016**, *9*, 247–255, doi:10.2147/MDER.S91102.
18. Li, C.; Ren, J.; Huang, H.; Wang, B.; Zhu, Y.; Hu, H. PCA and Deep Learning Based Myoelectric Grasping Control of a Prosthetic Hand. *Biomedical engineering online* **2018**, doi:10.1186/s12938-018-0539-8.
19. Transradial Amputee Gesture Classification Using an Optimal Number of SEMG Sensors: An Approach Using ICA Clustering - IEEE Journals & Magazine Available online: https://ieeexplore.ieee.org/document/7271103 (accessed on 17 November 2020).
20. Bi, L.; Feleke, A.-->Genetu; Guan, C. A Review on EMG-Based Motor Intention Prediction of Continuous Human Upper Limb Motion for Human-Robot Collaboration. *Biomedical Signal Processing and Control* **2019**, *51*, 113–127, doi:10.1016/j.bspc.2019.02.011.
21. Intelligent EMG Pattern Recognition Control Method for Upper-Limb Multifunctional Prostheses: Advances, Current Challenges, and Future Prospects Available online: https://ieeexplore.ieee.org/document/8612917 (accessed on 17 November 2020).
22. Yang, D.; Yang, W.; Huang, Q.; Liu, H. Classification of Multiple Finger Motions During Dynamic Upper Limb Movements. *IEEE J Biomed Health Inform* **2017**, *21*, 134–141, doi:10.1109/JBHI.2015.2490718.
23. Radmand, A.; Scheme, E.; Englehart, K. High-Density Force Myography: A Possible Alternative for Upper-Limb Prosthetic Control. *J Rehabil Res Dev* **2016**, *53*, 443–456, doi:10.1682/JRRD.2015.03.0041.
24. Hahne, J.M.; Biessmann, F.; Jiang, N.; Rehbaum, H.; Farina, D.; Meinecke, F.C.; Muller, K.-R.; Parra, L.C. Linear and Nonlinear Regression Techniques for Simultaneous and Proportional Myoelectric Control. *IEEE Trans Neural Syst Rehabil Eng* **2014**, *22*, 269–279, doi:10.1109/TNSRE.2014.2305520.
25. Cordella, F.; Ciancio, A.L.; Sacchetti, R.; Davalli, A.; Cutti, A.G.; Guglielmelli, E.; Zollo, L. Literature Review on Needs of Upper Limb Prosthesis Users. *Front Neurosci* **2016**, *10*, doi:10.3389/fnins.2016.00209.
26. Bergman, K.; Oernholmer, L.; Zackrisson, K.; Thyberg, M. Functional Benefit of an Adaptive Myoelectric Prosthetic Hand Compared to a Conventional Myoelectric Hand. *Prosthetics and orthotics international* **1992**, doi:10.3109/03093649209164305.
27. Vidovic, M.M.-C.; Hwang, H.-J.; Amsuss, S.; Hahne, J.M.; Farina, D.; Muller, K.-R. Improving the Robustness of Myoelectric Pattern Recognition for Upper Limb Prostheses by Covariate Shift Adaptation. *IEEE Trans Neural Syst Rehabil Eng* **2016**, *24*, 961–970, doi:10.1109/TNSRE.2015.2492619.
28. Parajuli, N.; Sreenivasan, N.; Bifulco, P.; Cesarelli, M.; Savino, S.; Niola, V.; Esposito, D.; Hamilton, T.J.; Naik, G.R.; Gunawardana, U.; et al. Real-Time EMG Based Pattern Recognition Control for Hand Prostheses: A Review on Existing Methods, Challenges and Future Implementation. *Sensors* **2019**, *19*, 4596, doi:10.3390/s19204596.
29. Tavakoli, M.; Benussi, C.; Lourenco, J.L. Single Channel Surface EMG Control of Advanced Prosthetic Hands: A Simple, Low Cost and Efficient Approach. *Expert Syst. Appl.* **2017**, doi:10.1016/j.eswa.2017.03.012.
30. Raez, M.B.I.; Hussain, M.S.; Mohd-Yasin, F. Techniques of EMG Signal Analysis: Detection, Processing, Classification and Applications. *Biol Proced Online* **2006**, *8*, 11–35, doi:10.1251/bpo115.
31. Jung, P.; Lim, G.; Kim, S.; Kong, K. A Wearable Gesture Recognition Device for Detecting Muscular Activities Based on Air-Pressure Sensors. *IEEE Transactions on Industrial Informatics* **2015**, *11*, 485–494, doi:10.1109/TII.2015.2405413.
32. Ibitoye, M.O.; Hamzaid, N.A.; Zuniga, J.M.; Abdul Wahab, A.K. Mechanomyography and Muscle Function Assessment: A Review of Current State

and Prospects. *Clin Biomech (Bristol, Avon)* **2014**, *29*, 691–704, doi:10.1016/j.clinbiomech.2014.04.003.
33. Beck, T.W.; Housh, T.J.; Cramer, J.T.; Weir, J.P.; Johnson, G.O.; Coburn, J.W.; Malek, M.H.; Mielke, M. Mechanomyographic Amplitude and Frequency Responses during Dynamic Muscle Actions: A Comprehensive Review. *Biomed Eng Online* **2005**, *4*, 67, doi:10.1186/1475-925X-4-67.
34. Deffieux, T.; Gennisson, J.-L.; Tanter, M.; Fink, M.; Nordez, A. Ultrafast Imaging of in Vivo Muscle Contraction Using Ultrasound. *Appl. Phys. Lett.* **2006**, *89*, 184107, doi:10.1063/1.2378616.
35. Barry, D.T.; Leonard, J.A.; Gitter, A.J.; Ball, R.D. Acoustic Myography as a Control Signal for an Externally Powered Prosthesis. *Arch Phys Med Rehabil* **1986**, *67*, 267–269.
36. Posatskiy, A.O.; Chau, T. The Effects of Motion Artifact on Mechanomyography: A Comparative Study of Microphones and Accelerometers. *Journal of Electromyography and Kinesiology* **2012**, *22*, 320–324, doi:10.1016/j.jelekin.2011.09.004.
37. Silva, J.; Heim, W.; Chau, T. A Self-Contained, Mechanomyography-Driven Externally Powered Prosthesis. *Arch Phys Med Rehabil* **2005**, *86*, 2066–2070, doi:10.1016/j.apmr.2005.03.034.
38. Silva, J.; Chau, T. Coupled Microphone-Accelerometer Sensor Pair for Dynamic Noise Reduction in MMG Signal Recording. *Electronics Letters* **2003**, *39*, 1496–1498, doi:10.1049/el:20031003.
39. Antonelli, M.G.; Zobel, P.B.; Giacomin, J. Use of MMG Signals for the Control of Powered Orthotic Devices: Development of a Rectus Femoris Measurement Protocol. *Assist Technol* **2009**, *21*, 1–12, doi:10.1080/10400430902945678.
40. Plewa, K.; Samadani, A.; Chau, T. Comparing Electro- and Mechano-Myographic Muscle Activation Patterns in Self-Paced Pediatric Gait. *J Electromyogr Kinesiol* **2017**, *36*, 73–80, doi:10.1016/j.jelekin.2017.07.002.
41. Dahmane, R.; Valenčič, V.; Knez, N.; Eržen, I. Evaluation of the Ability to Make Non-Invasive Estimation of Muscle Contractile Properties on the Basis of the Muscle Belly Response. *Med. Biol. Eng. Comput.* **2001**, *39*, 51–55, doi:10.1007/BF02345266.
42. Rusu, L.D.; Cosma, G.G.; Cernaianu, S.M.; Marin, M.N.; Rusu, P.F.A.; Ciocănescu, D.P.; Neferu, F.N. Tensiomyography Method Used for Neuromuscular Assessment of Muscle Training. *J Neuroeng Rehabil* **2013**, *10*, 67, doi:10.1186/1743-0003-10-67.
43. Ditroilo, M.; Smith, I.J.; Fairweather, M.M.; Hunter, A.M. Long-Term Stability of Tensiomyography Measured under Different Muscle Conditions. *Journal of Electromyography and Kinesiology* **2013**, *23*, 558–563, doi:10.1016/j.jelekin.2013.01.014.
44. Lobo-Prat, J.; Kooren, P.N.; Stienen, A.H.A.; Herder, J.L.; Koopman, B.F.J.M.; Veltink, P.H. Non-Invasive Control Interfaces for Intention Detection in Active Movement-Assistive Devices. *J Neuroeng Rehabil* **2014**, *11*, 168, doi:10.1186/1743-0003-11-168.
45. Đorđević, S.; Stančin, S.; Meglič, A.; Milutinović, V.; Tomažič, S. MC Sensor--a Novel Method for Measurement of Muscle Tension. *Sensors (Basel)* **2011**, *11*, 9411–9425, doi:10.3390/s111009411.
46. Silva, O.L.; Sousa, T.H.S.; Hoffman, I.O.; Camargo, E.D.L.B. de; Moura, F.S. de; Martins, A.R.C.; Biasi, C.; Fantoni, D.T.; Lima, R.G. A Proposal to Monitor Muscle Contraction through the Change of Electrical Impedance inside a Muscle. In Proceedings of the 5th IEEE RAS/EMBS International Conference on Biomedical Robotics and Biomechatronics; August 2014; pp. 763–767.
47. Bifulco, P.; Esposito, D.; Gargiulo, G.D.; Savino, S.; Niola, V.; Iuppariello, L.; Cesarelli, M. A Stretchable, Conductive Rubber Sensor to Detect Muscle

Contraction for Prosthetic Hand Control. In Proceedings of the 2017 E-Health and Bioengineering Conference (EHB); June 2017; pp. 173–176.
48. Kim, W.S.; Lee, H.D.; Lim, D.H.; Han, J.S.; Shin, K.S.; Han, C.S. Development of a Muscle Circumference Sensor to Estimate Torque of the Human Elbow Joint. *Sensors and Actuators A: Physical* **2014**, *208*, 95–103, doi:10.1016/j.sna.2013.12.036.
49. Han, H.; Kim, J. Active Muscle Stiffness Sensor Based on Piezoelectric Resonance for Muscle Contraction Estimation. *Sensors and Actuators A: Physical* **2013**, *194*, 212–219, doi:10.1016/j.sna.2013.01.054.
50. Guo, J.-Y.; Zheng, Y.-P.; Xie, H.-B.; Chen, X. Continuous Monitoring of Electromyography (EMG), Mechanomyography (MMG), Sonomyography (SMG) and Torque Output during Ramp and Step Isometric Contractions. *Medical Engineering & Physics* **2010**, *32*, 1032–1042, doi:10.1016/j.medengphy.2010.07.004.
51. Kenney, L.P.; Lisitsa, I.; Bowker, P.; Heath, G.H.; Howard, D. Dimensional Change in Muscle as a Control Signal for Powered Upper Limb Prostheses: A Pilot Study. *Med Eng Phys* **1999**, *21*, 589–597, doi:10.1016/s1350-4533(99)00089-2.
52. Bansal, A.K.; Hou, S.; Kulyk, O.; Bowman, E.M.; Samuel, I.D.W. Wearable Organic Optoelectronic Sensors for Medicine. *Adv Mater* **2015**, *27*, 7638–7644, doi:10.1002/adma.201403560.
53. Zhou, B.; Sundholm, M.; Cheng, J.; Cruz, H.; Lukowicz, P. Measuring Muscle Activities during Gym Exercises with Textile Pressure Mapping Sensors. *Pervasive and Mobile Computing* **2017**, *38*, 331–345, doi:10.1016/j.pmcj.2016.08.015.
54. Amft, O.; Junker, H.; Lukowicz, P.; Troster, G.; Schuster, C. Sensing Muscle Activities with Body-Worn Sensors. In Proceedings of the International Workshop on Wearable and Implantable Body Sensor Networks (BSN'06); April 2006; p. 4 pp. – 141.
55. Lukowicz, P.; Hanser, F.; Szubski, C.; Schobersberger, W. Detecting and Interpreting Muscle Activity with Wearable Force Sensors. In Proceedings of the Pervasive Computing; Fishkin, K.P., Schiele, B., Nixon, P., Quigley, A., Eds.; Springer: Berlin, Heidelberg, 2006; pp. 101–116.
56. Cavanagh, P.R.; Komi, P.V. Electromechanical Delay in Human Skeletal Muscle under Concentric and Eccentric Contractions. *Europ. J. Appl. Physiol.* **1979**, *42*, 159–163, doi:10.1007/BF00431022.
57. Viitasalo, J.T.; Komi, P.V. Interrelationships between Electromyographic, Mechanical, Muscle Structure and Reflex Time Measurements in Man. *Acta Physiol Scand* **1981**, *111*, 97–103, doi:10.1111/j.1748-1716.1981.tb06710.x.
58. Ferris-Hood, K.; Threlkeld, A.J.; Horn, T.S.; Shapiro, R. Relaxation Electromechanical Delay of the Quadriceps during Selected Movement Velocities. *Electromyography and clinical neurophysiology* **1996**, *36*, 157–170.
59. Esposito, F.; Limonta, E.; Cè, E. Passive Stretching Effects on Electromechanical Delay and Time Course of Recovery in Human Skeletal Muscle: New Insights from an Electromyographic and Mechanomyographic Combined Approach. *Eur J Appl Physiol* **2011**, *111*, 485–495, doi:10.1007/s00421-010-1659-4.
60. Sasaki, K.; Sasaki, T.; Ishii, N. Acceleration and Force Reveal Different Mechanisms of Electromechanical Delay. *Med Sci Sports Exerc* **2011**, *43*, 1200–1206, doi:10.1249/MSS.0b013e318209312c.
61. Esposito, F.; Cè, E.; Rampichini, S.; Limonta, E.; Venturelli, M.; Monti, E.; Bet, L.; Fossati, B.; Meola, G. Electromechanical Delay Components during Skeletal Muscle Contraction and Relaxation in Patients with Myotonic Dystrophy Type 1. *Neuromuscul Disord* **2016**, *26*, 60–72, doi:10.1016/j.nmd.2015.09.013.
62. Esposito, D.; Andreozzi, E.; Fratini, A.; Gargiulo, G.D.; Savino, S.; Niola, V.; Bifulco, P. A Piezoresistive Sensor to Measure Muscle Contraction and Mechanomyography. *Sensors (Basel)* **2018**, *18*, doi:10.3390/s18082553.

63. Carrozza, M.C.; Suppo, C.; Sebastiani, F.; Massa, B.; Vecchi, F.; Lazzarini, R.; Cutkosky, M.R.; Dario, P. The SPRING Hand: Development of a Self-Adaptive Prosthesis for Restoring Natural Grasping. *Autonomous Robots* **2004**, *16*, 125–141, doi:10.1023/B:AURO.0000016863.48502.98.
64. Jt, B.; Am, D. Novel Differential Mechanism Enabling Two DOF from a Single Actuator: Application to a Prosthetic Hand. *IEEE Int Conf Rehabil Robot* **2013**, *2013*, 6650441–6650441, doi:10.1109/icorr.2013.6650441.
65. Kamikawa, Y.; Maeno, T. Underactuated Five-Finger Prosthetic Hand Inspired by Grasping Force Distribution of Humans. In Proceedings of the 2008 IEEE/RSJ International Conference on Intelligent Robots and Systems, IROS; 2008; pp. 717–722.
66. Fukaya, N.; Toyama, S.; Asfour, T.; Dillmann, R. Design of the TUAT/Karlsruhe Humanoid Hand. *Proceedings. 2000 IEEE/RSJ International Conference on Intelligent Robots and Systems (IROS 2000) (Cat. No.00CH37113)* **2000**, doi:10.1109/IROS.2000.895225.
67. Fukaya, N.; Asfour, T.; Dillmann, R.; Toyama, S. Development of a Five-Finger Dexterous Hand without Feedback Control: The TUAT/Karlsruhe Humanoid Hand. *2013 IEEE/RSJ International Conference on Intelligent Robots and Systems* **2013**, doi:10.1109/IROS.2013.6697008.
68. Weiner, P.; Starke, J.; Hundhausen, F.; Beil, J.; Asfour, T. The KIT Prosthetic Hand: Design and Control. *2018 IEEE/RSJ International Conference on Intelligent Robots and Systems (IROS)* **2018**, doi:10.1109/IROS.2018.8593851.
69. Mnyusiwalla, H.; Vulliez, P.; Gazeau, J.-P.; Zeghloul, S. A New Dexterous Hand Based on Bio-Inspired Finger Design for Inside-Hand Manipulation. *IEEE Transactions on Systems, Man, and Cybernetics: Systems* **2016**, *46*, 809–817, doi:10.1109/TSMC.2015.2468678.
70. Jacobsen, S.C.; Wood, J.E.; Knutti, D.F.; Biggers, K.B. The UTAH/M.I.T. Dextrous Hand: Work in Progress: *The International Journal of Robotics Research* **2016**, doi:10.1177/027836498400300402.
71. Antfolk, C.; D'Alonzo, M.; Rosén, B.; Lundborg, G.; Sebelius, F.; Cipriani, C. Sensory Feedback in Upper Limb Prosthetics. *Expert Rev Med Devices* **2013**, *10*, 45–54, doi:10.1586/erd.12.68.
72. Brown, J.D.; Paek, A.; Syed, M.; O'Malley, M.K.; Shewokis, P.A.; Contreras-Vidal, J.L.; Davis, A.J.; Gillespie, R.B. An Exploration of Grip Force Regulation with a Low-Impedance Myoelectric Prosthesis Featuring Referred Haptic Feedback. *J Neuroeng Rehabil* **2015**, *12*, doi:10.1186/s12984-015-0098-1.
73. Cloutier, A.; Yang, J. Design, Control, and Sensory Feedback of Externally Powered Hand Prostheses: A Literature Review. *Crit Rev Biomed Eng* **2013**, *41*, 161–181, doi:10.1615/critrevbiomedeng.2013007887.
74. Li, K.; Fang, Y.; Zhou, Y.; Liu, H. Non-Invasive Stimulation-Based Tactile Sensation for Upper-Extremity Prosthesis: A Review. *IEEE Sensors Journal* **2017**, *PP*, doi:10.1109/JSEN.2017.2674965.
75. VINCENTevolution 2 Available online: https://vincentsystems.de/en/prosthetics/vincent-evolution-2/ (accessed on 17 August 2020).
76. Fu, Q.; Santello, M. Improving Fine Control of Grasping Force during Hand–Object Interactions for a Soft Synergy-Inspired Myoelectric Prosthetic Hand. *Front. Neurorobot.* **2018**, *11*, doi:10.3389/fnbot.2017.00071.
77. Federica Prosthetic Hand Available online: http://ingegneria-biomedica.dieti.unina.it/index.php/en/projects/federica-prosthetic-hand.html (accessed on 18 August 2020).
78. Interlink Electronics FSR Sensor, Force Sensing Resistor | Interlink Electronics Available online: https://www.interlinkelectronics.com/force-sensing-resistor (accessed on 13 November 2020).

79. Lebosse, C.; Renaud, P.; Bayle, B.; Mathelin, M. de Modeling and Evaluation of Low-Cost Force Sensors. *IEEE Transactions on Robotics* **2011**, *27*, 815–822, doi:10.1109/TRO.2011.2119850.
80. Tiwana, M.I.; Redmond, S.J.; Lovell, N.H. A Review of Tactile Sensing Technologies with Applications in Biomedical Engineering. *Sensors and Actuators A: Physical* **2012**, *179*, 17–31, doi:10.1016/j.sna.2012.02.051.
81. Underlying Physics of Conductive Polymer Composites and Force Sensing Resistors (FSRs). A Study on Creep Response and Dynamic Loading Available online: https://www.ncbi.nlm.nih.gov/pmc/articles/PMC5706281/ (accessed on 16 November 2020).
82. Paredes-Madrid, L.; Palacio, C.A.; Matute, A.; Parra Vargas, C.A. Underlying Physics of Conductive Polymer Composites and Force Sensing Resistors (FSRs) under Static Loading Conditions. *Sensors (Basel)* **2017**, *17*, doi:10.3390/s17092108.
83. Stassi, S.; Cauda, V.; Canavese, G.; Pirri, C.F. Flexible Tactile Sensing Based on Piezoresistive Composites: A Review. *Sensors (Basel)* **2014**, *14*, 5296–5332, doi:10.3390/s140305296.
84. Inc, I.E. Request Datasheets Available online: https://www.interlinkelectronics.com/request-data-sheets (accessed on 13 November 2020).
85. Paredes-Madrid, L.; Matute, A.; Bareño, J.O.; Parra Vargas, C.A.; Gutierrez Velásquez, E.I. Underlying Physics of Conductive Polymer Composites and Force Sensing Resistors (FSRs). A Study on Creep Response and Dynamic Loading. *Materials (Basel)* **2017**, *10*, doi:10.3390/ma10111334.
86. Xie, H.-B.; Zheng, Y.-P.; Guo, J.-Y. Classification of the Mechanomyogram Signal Using a Wavelet Packet Transform and Singular Value Decomposition for Multifunction Prosthesis Control. *Physiol Meas* **2009**, *30*, 441–457, doi:10.1088/0967-3334/30/5/002.
87. Spires, M.C.; Kelly, B.; Davis, A.J. *Prosthetic Restoration and Rehabilitation of the Upper and Lower Extremity*; 2014; ISBN 978-1-306-19704-5.
88. Esposito, D.; Andreozzi, E.; Gargiulo, G.D.; Fratini, A.; D'Addio, G.; Naik, G.R.; Bifulco, P. A Piezoresistive Array Armband With Reduced Number of Sensors for Hand Gesture Recognition. *Front Neurorobot* **2020**, *13*, doi:10.3389/fnbot.2019.00114.
89. Kamen, G.; Gabriel, D.A. Essentials of Electromyography Available online: /paper/Essentials-of-Electromyography-Kamen-Gabriel/17a0c87549f413a0cea07cefb086a03baf51d1bb (accessed on 18 August 2020).
90. Hodges, P.W.; Bui, B.H. A Comparison of Computer-Based Methods for the Determination of Onset of Muscle Contraction Using Electromyography. *Electroencephalogr Clin Neurophysiol* **1996**, *101*, 511–519, doi:10.1016/s0013-4694(96)95190-5.
91. Roberts, T.J.; Gabaldón, A.M. Interpreting Muscle Function from EMG: Lessons Learned from Direct Measurements of Muscle Force. *Integr Comp Biol* **2008**, *48*, 312–320, doi:10.1093/icb/icn056.
92. Hitec HITEC Robot Servo Available online: https://hitecrcd.com/products/servos/discontinued-servos-servo-accessories/hsr-5990tg-hmi-ultra-premium-robot-servo/product (accessed on 20 August 2020).
93. Drake, R.L.; Vogl, W.; Mitchell, A.W.M.; Gray, H. *Gray's Anatomy for Students*; 2015; ISBN 978-0-7020-5131-9.
94. Esposito, D.; Cosenza, C.; Gargiulo, G.D.; Andreozzi, E.; Niola, V.; Fratini, A.; D'Addio, G.; Bifulco, P. Experimental Study to Improve "Federica" Prosthetic Hand and Its Control System. In Proceedings of the XV Mediterranean Conference on Medical and Biological Engineering and Computing – MEDICON 2019; Henriques, J., Neves, N., de Carvalho, P., Eds.; Springer International Publishing: Cham, 2020; pp. 586–593.

95. Esposito, D.; Savino, S.; Cosenza, C.; Gargiulo, G.D.; Fratini, A.; Cesarelli, G.; Bifulco, P. Study on the Activation Speed and the Energy Consumption of "Federica" Prosthetic Hand. In Proceedings of the XV Mediterranean Conference on Medical and Biological Engineering and Computing – MEDICON 2019; Henriques, J., Neves, N., de Carvalho, P., Eds.; Springer International Publishing: Cham, 2020; pp. 594–603.
96. Esposito, D.; Gargiulo, G.D.; Parajuli, N.; Cesarelli, G.; Andreozzi, E.; Bifulco, P. Measurement of Muscle Contraction Timing for Prosthesis Control: A Comparison between Electromyography and Force-Myography. In Proceedings of the 2020 IEEE International Symposium on Medical Measurements and Applications (MeMeA); June 2020; pp. 1–6.
97. ACS712: Hall-Effect-Based Linear Current Sensor IC Available online: https://www.allegromicro.com/en/products/sense/current-sensor-ics/zero-to-fifty-amp-integrated-conductor-sensor-ics/acs712 (accessed on 21 January 2021).
98. Steeper Group - Upper Limb Available online: https://www.steepergroup.com/prosthetics/upper-limb-prosthetics/ (accessed on 21 January 2021).
99. Arm Prosthesis | Ottobock UK Available online: https://www.ottobock.co.uk/prosthetics/upper_limbs_prosthetics/ (accessed on 17 November 2020).
100. Kurillo, G.; Gregorič, M.; Goljar, N.; Bajd, T. Grip Force Tracking System for Assessment and Rehabilitation of Hand Function. *Technology and health care : official journal of the European Society for Engineering and Medicine* **2005**, doi:10.3233/thc-2005-13301.
101. Belter, J.T.; Dollar, A.M. Performance Characteristics of Anthropomorphic Prosthetic Hands. In Proceedings of the 2011 IEEE International Conference on Rehabilitation Robotics; June 2011; pp. 1–7.
102. Belter, J.T.; Leddy, M.T.; Gemmell, K.D.; Dollar, A.M. Comparative Clinical Evaluation of the Yale Multigrasp Hand. In Proceedings of the 2016 6th IEEE International Conference on Biomedical Robotics and Biomechatronics (BioRob); IEEE: Singapore, Singapore, June 2016; pp. 528–535.
103. Irwin, C.B.; Towles, J.D.; Radwin, R.G. Development and Application of a Multi-Axis Dynamometer for Measuring Grip Force. *Ergonomics* **2013**, *56*, doi:10.1080/00140139.2013.847212.
104. Szewczyk, R.; Zieliński, C.; Kaliczyńska, M. *Automation 2019: Progress in Automation, Robotics and Measurement Techniques*; Springer, 2019; ISBN 978-3-030-13273-6.
105. Measure Grip Forces Available online: https://www.tekscan.com/measure-grip-forces (accessed on 18 August 2020).
106. Carbone, G.; Rossi, C.; Savino, S. Performance Comparison Between FEDERICA Hand and LARM Hand. *International Journal of Advanced Robotic Systems* **2015**, *12*, 90, doi:10.5772/60523.
107. Pylatiuk, C.; Kargov, A.; Schulz, S.; Döderlein, L. Distribution of Grip Force in Three Different Functional Prehension Patterns. *Journal of Medical Engineering & Technology* **2006**, *30*, 176–182, doi:10.1080/03091900600565217.
108. Kargov, A.; Pylatiuk, C.; Martin, J.; Schulz, S.; Döderlein, L. A Comparison of the Grip Force Distribution in Natural Hands and in Prosthetic Hands. *Disability and Rehabilitation* **2004**, *26*, 705–711, doi:10.1080/09638280410001704278.
109. Cosenza, C.; Niola, V.; Savino, S. A Mechanical Hand for Prosthetic Applications: Multibody Model and Contact Simulation. *Proc Inst Mech Eng H* **2018**, *232*, 819–825, doi:10.1177/0954411918787548.
110. Falco, J.; Van Wyk, K.; Messina, E. *Performance Metrics and Test Methods for Robotic Hands*; 2018;

111. INA122 Data Sheet, Product Information and Support | TI.Com Available online: https://www.ti.com/product/INA122 (accessed on 20 August 2020).
112. Industries, A. INA169 Analog DC Current Sensor Breakout - 60V 5A Max Available online: https://www.adafruit.com/product/1164 (accessed on 20 August 2020).
113. Guccione, S.; McKirahan, J. *Human Machine Interface: Concepts and Projects*; Industrial Press, 2016; ISBN 978-0-8311-3582-9.
114. Boy, G.A. *The Handbook of Human-Machine Interaction: A Human-Centered Design Approach*; CRC Press, 2017; ISBN 978-1-317-02946-5.
115. Chakraborty, B.K.; Sarma, D.; Bhuyan, M.K.; MacDorman, K.F. Review of Constraints on Vision-Based Gesture Recognition for Human–Computer Interaction. *IET Computer Vision* **2018**, *12*, 3–15, doi:10.1049/iet-cvi.2017.0052.
116. Abraham, L.; Urru, A.; Normani, N.; Wilk, M.P.; Walsh, M.; O'Flynn, B. Hand Tracking and Gesture Recognition Using Lensless Smart Sensors. *Sensors* **2018**, *18*, 2834, doi:10.3390/s18092834.
117. Geng, W.; Du, Y.; Jin, W.; Wei, W.; Hu, Y.; Li, J. Gesture Recognition by Instantaneous Surface EMG Images. *Scientific Reports* **2016**, *6*, 36571, doi:10.1038/srep36571.
118. Du, Y.; Jin, W.; Wei, W.; Hu, Y.; Geng, W. Surface EMG-Based Inter-Session Gesture Recognition Enhanced by Deep Domain Adaptation. *Sensors (Basel)* **2017**, *17*, doi:10.3390/s17030458.
119. Nymoen, K.; Haugen, M.; Jensenius, A. Mumyo - Evaluating and Exploring the Myo Armband for Musical Interaction. In Proceedings of the NIME; 2015.
120. Sathiyanarayanan, M.; Rajan, S. MYO Armband for Physiotherapy Healthcare: A Case Study Using Gesture Recognition Application. *2016 8th International Conference on Communication Systems and Networks (COMSNETS)* **2016**, doi:10.1109/COMSNETS.2016.7439933.
121. Visconti, P.; Gaetani, F.; Zappatore, G.A.; Primiceri, P. Technical Features and Functionalities of Myo Armband: An Overview on Related Literature and Advanced Applications of Myoelectric Armbands Mainly Focused on Arm Prostheses. **2018**, doi:10.21307/IJSSIS-2018-005.
122. Bisi, S.; De Luca, L.; Shrestha, B.; Yang, Z.; Gandhi, V. Development of an EMG-Controlled Mobile Robot. *Robotics* **2018**, *7*, 36, doi:10.3390/robotics7030036.
123. Zhu, Y.; Jiang, S.; Shull, P.B. Wrist-Worn Hand Gesture Recognition Based on Barometric Pressure Sensing. *2018 IEEE 15th International Conference on Wearable and Implantable Body Sensor Networks (BSN)* **2018**, doi:10.1109/BSN.2018.8329688.
124. Caramiaux, B.; Donnarumma, M.; Tanaka, A. Understanding Gesture Expressivity through Muscle Sensing. *TCHI* **2015**, doi:10.1145/2687922.
125. Huang, Y.; Yang, X.; Li, Y.; Zhou, D.; He, K.; Liu, H. Ultrasound-Based Sensing Models for Finger Motion Classification. *IEEE Journal of Biomedical and Health Informatics* **2018**, *22*, 1395–1405, doi:10.1109/JBHI.2017.2766249.
126. Booth, R.; Goldsmith, P. A Wrist-Worn Piezoelectric Sensor Array for Gesture Input. *J. Med. Biol. Eng.* **2018**, *38*, 284–295, doi:10.1007/s40846-017-0303-8.
127. Elahi, H.; Eugeni, M.; Gaudenzi, P. A Review on Mechanisms for Piezoelectric-Based Energy Harvesters. *Energies* **2018**, *11*, 1850, doi:10.3390/en11071850.
128. Giovanelli, D.; Farella, E. Force Sensing Resistor and Evaluation of Technology for Wearable Body Pressure Sensing. *J. Sensors* **2016**, doi:10.1155/2016/9391850.
129. McIntosh, J.; McNeill, C.; Fraser, M.; Kerber, F.; Lochtefeld, M.; Krüger, A. EMPress: Practical Hand Gesture Classification with Wrist-Mounted EMG and Pressure Sensing. In Proceedings of the CHI '16: Proceedings, 34th Annual CHI Conference on Human Factors in Computing Systems; Association for Computing Machinery, May 31 2016; pp. 2332–2342.

130. Jiang, X.; Merhi, L.-K.; Xiao, Z.G.; Menon, C. Exploration of Force Myography and Surface Electromyography in Hand Gesture Classification. *Medical Engineering & Physics* **2017**, *41*, 63–73, doi:10.1016/j.medengphy.2017.01.015.
131. Cho, E.; Chen, R.; Merhi, L.-K.; Xiao, Z.; Pousett, B.; Menon, C. Force Myography to Control Robotic Upper Extremity Prostheses: A Feasibility Study. *Front Bioeng Biotechnol* **2016**, *4*, doi:10.3389/fbioe.2016.00018.
132. Ma, M.; Bechkoum, K. Serious Games for Movement Therapy after Stroke. In Proceedings of the 2008 IEEE International Conference on Systems, Man and Cybernetics; October 2008; pp. 1872–1877.
133. Witten, I.H.; Frank, E.; Hall, M.A.; Pal, C.J. *Data Mining: Practical Machine Learning Tools and Techniques*; Morgan Kaufmann, 2016; ISBN 978-0-12-804357-8.
134. D'Ausilio, A. Arduino: A Low-Cost Multipurpose Lab Equipment. *Behav Res Methods* **2012**, *44*, 305–313, doi:10.3758/s13428-011-0163-z.
135. Arduino Uno Rev3 | Arduino Official Store Available online: https://store.arduino.cc/arduino-uno-rev3 (accessed on 18 November 2020).
136. Processing.Org Available online: https://processing.org/ (accessed on 18 November 2020).
137. Pong Game Available online: https://www.ponggame.org/ (accessed on 21 January 2021).
138. Polisiero, M.; Bifulco, P.; Liccardo, A.; Cesarelli, M.; Romano, M.; Gargiulo, G.D.; McEwan, A.L.; D'Apuzzo, M. Design and Assessment of a Low-Cost, Electromyographically Controlled, Prosthetic Hand. *Med Devices (Auckl)* **2013**, *6*, 97–104, doi:10.2147/MDER.S39604.
139. Ulloa, G.D.F.; Sreenivasan, N.; Bifulco, P.; Cesarelli, M.; Gargiulo, G.; Gunawardana, U. Cost Effective Electro — Resistive Band Based Myo Activated Prosthetic Upper Limb for Amputees in the Developing World. In Proceedings of the 2017 IEEE Life Sciences Conference (LSC); December 2017; pp. 250–253.

Hand prostheses partially restore hand appearance and functionalities. Not everyone can afford expensive prostheses and many low-cost prostheses have been proposed. In particular, 3D printers have provided great opportunities by simplifying the manufacturing process and reducing costs. Generally, active prostheses use multiple motors for fingers movement and are controlled by electromyographic (EMG) signals. The “Federica” hand is a single motor prosthesis, equipped with an adaptive grasp and controlled by a force-myographic signal.

The “Federica” hand is 3D printed and has an anthropomorphic morphology with five fingers, each consisting of three phalanges. The movement generated by a single servomotor is transmitted to the fingers by inextensible tendons that form a closed chain; practically, no springs are used for passive hand opening. A differential mechanical system simultaneously distributes the motor force in predefined portions on each finger, regardless of their actual positions. Proportional control of hand closure is achieved by measuring the contraction of residual limb muscles by means of a force sensor, replacing the EMG. The electrical current of the servomotor is monitored to provide the user with a sensory feedback of the grip force, through a small vibration motor. A simple Arduino board was adopted as processing unit.

The differential mechanism guarantees an efficient transfer of mechanical energy from the motor to the fingers and a secure grasp of any object, regardless of its shape and deformability. The force sensor, being extremely thin, can be easily embedded into the prosthesis socket and positioned on both muscles and tendons; it offers some advantages over the EMG as it does not require any electrical contact or signal processing to extract information about the muscle contraction intensity. The grip speed is high enough to allow the user to grab objects on the fly: from the muscle trigger until to the complete hand closure, “Federica” takes about half a second. The cost of the device is about 100 US$. Preliminary tests carried out on a patient with transcarpal amputation, showed high performances in controlling the prosthesis, after a very rapid training session.

The "Federica" hand turned out to be a lightweight, low-cost and extremely efficient prosthesis. The project is intended to be open-source: all the information needed to produce the prosthesis (e.g. CAD files, circuit schematics, software) can be downloaded from a public repository. Thus, allowing everyone to use the “Federica” hand and customize or improve it.